MEDIUM FREQUENCY POWER DISTRIBUTION ARCHITECTURES FOR NEXT GENERATION PHOTOVOLTAIC FARMS AND DATA CENTERS

A Dissertation

by

BAHAAELDEEN MOHAMED RABEE HAFEZ

Submitted to the Office of Graduate and Professional Studies of
Texas A&M University
in partial fulfillment of the requirements for the degree of

DOCTOR OF PHILOSOPHY

Chair of Committee,	Prasad N. Enjeti
Co-Chair of Committee,	Shehab Ahmed
Committee Members,	Reza Langari
	Hamid A. Toliyat
Head of Department,	Miroslav M. Begovic

August 2015

Major Subject: Electrical Engineering

ABSTRACT

With the recent advancement of power electronics devices, the power electronics converters take more vital roles in the modern power systems given the increased renewable energy penetration such as wind turbines, solar photovoltaic(PV), ocean power …etc. In the same time, the conventional market for power converters that include motor drives and power supplies always increase their requirements bar towards high efficiency, low cost, high density, and high reliability. The key to a high density power supply is to decrease the magnetic elements within the power converters namely the inductors and transformers. The wide band gap based power electronics devices open the door to satisfy the aforementioned power converters' requirements with its ability to fast switching at lower losses and smaller footprint. The focus of this dissertation is to propose and analyze two architectures for utility scale PV farms and data centers employing medium frequency (MF) transformers.

The proposed utility scale PV structure is shown to increase power density and improves system modularity while maintaining high efficiency levels. The PV panels power standard three phase voltage source inverters to generate MF ac voltage. Various voltage source inverter outputs are combined in series via MF transformers to form the proposed MF ac collection grid. A three phase ac-ac cycloconverter interfaces the MF grid with the 60Hz mains. An 80MW PV power plant located in Eggebek/Germany is used for comparison as a design example. Detailed simulation and calculations of the

proposed system demonstrates size/weight reduction and overall efficiency improvement of 2%.

The second proposal is for a medium-voltage (MV) data center power distribution system (DC-PDS) architecture using medium-frequency (MF) link transformer isolation. The proposed approach significantly improves power density while maintaining high efficiency compared to conventional line-frequency based solutions. The approach also contributes to a reduction in PVC and copper used in conventional DC-PDS. First the MV transformed from the utility, is interfaced with a MV switch gear system and a diesel power generator (DPG) system. Then this MV is converted to the low voltages (LVs) required by the loads via MF transformer. The MF transformer primary side windings are connected to stacked AC-AC converters. The LV secondary windings are interfaced with several load systems and battery energy storage system (BESS) using different topologies like boost power factor corrector (PFC), PWM inverter, etc. The presence of MV switch gear and MF transformer in the architecture results in higher efficiency and power density. Extensive finite element (FEA) results are carried out to optimize the transformer design for this proposal. Afterwards, simulation results along with experimental results are presented to validate the proposed concept. Finally, highlights of all the contributions alongside with the recommended future research opportunities are summarized at the end.

DEDICATION

بسم الله الرحمن الرحيم

إلى امي

In The Name of Allah, Most Gracious, Most Merciful

To My Mother

ACKNOWLEDGEMENTS

I would like to thank my advisor Prof. Prasad N. Enjeti for his guidance during my PhD period. I am privileged and lucky to be one of his students. Despite his overwhelming schedule, he was always generous with his time and guided me to overcome all technical challenges that I faced through my work beside this he was a great mentor and gave the best advice for my career.

There are no enough words to thank my co-chair and first mentor and role model Dr. Shehab Ahmed. He opened the door for me to pursue my graduate studies and fully supported me all the way. His morals and dedication to his work will always be an inspiration to me.

I would like also to thank my committee members Prof. Reza Langari and Prof. Hamid A. Toliyat for their time and guidance. Their technical feedback and recommendations improves my work outcome.

I would like also to extend my thanks to Texas A&M ECE department staff, especially Tammy Carda, Jeanie Marshall, Annie Brunker and Melissa Sheldon. They demonstrated the cooperative/friendly spirit within Aggie-Land and facilitated my journey at Texas A&M in every possible way.

I would like also to express my heartfelt thanks to my colleagues and friends Ahmed Morsy, Ahmed Zahran, Harish Sarma, Teayong Kang and all PQ Lab team members and to my summer intern mentor in Halliburton Ayman Kabire.

I owe every achievement in my life to God, my parents and to my great family who gave me their unconditional love and ultimate support and always motivate me during my down time.

Lastly, I thank my wife who her love, support and trust in me motivated me during my PhD journey.

TABLE OF CONTENTS

Page

ABSTRACT ii

DEDICATION iv

ACKNOWLEDGEMENTS v

TABLE OF CONTENTS vii

LIST OF FIGURES ix

LIST OF TABLES xvii

1. INTRODUCTION 1

1.1. High Density Power Supply 4
1.2. Utility Scale PV Farm 6
1.3. Data Center 10
1.4. Research Objective 11
1.5. Outline of Dissertation 13

2. UTILITY SCALE PHOTOVOLTAIC FARMS 15

2.1. Introduction/Existing Architecture 16
2.2. Case Study 21
2.3. Proposed Medium Frequency AC Collection Grid 22
2.3.1. Analysis of the Proposed System 24
2.3.1.1. Three Phase Inverter 24
2.3.1.2. Transformer 27
2.3.1.3. AC Cables 36
2.3.1.4. Cycloconverter 41
2.3.2. Control of the Proposed System 42
2.3.3. Simulation of the Proposed System 47
2.3.3.1. Different Insulation Levels 48
2.3.3.2. Fault Condition 54
2.4. Summary 62

3. DATA CENTER 63

3.1. Introduction/ Existing Architecture 63
3.2. Proposed Medium Frequency Data Center Structure 67

3.2.1. Analysis and Simulation of the Proposed System 70
3.2.1.1. Multi-Level AC-AC Converter 72
3.2.1.2. Medium Frequency Transformer 74
3.2.1.3. Three Phase PWM Inverter 86
3.2.1.4. Single Phase Boost PFC 87
3.2.1.5. Loads and UPS 88
3.3. Summary 90

4. HARDWARE RESULTS 91

4.1. Utility Scale PV Farm 91
4.1.1. Steady State Waveforms 96
4.1.2. Transient Waveforms 100
4.2. Data Center 105
4.2.1. Data Center with Resistive Load 106
4.2.2. Data Center with Boost PFC Load 109
4.3. Summary 112

5. SUMMARY 113

5.1. Conclusion 113
5.2. Future Work 114

REFERENCES 115

APPENDIX 123

LIST OF FIGURES

Page

Figure 1–1. Typical power system structure that include traditional and renewable energy sources [2] 1

Figure 1–2. Summary of Si, SiC and GaN relevant material properties (© 2014 IEEE [7]– Adapted with permission from the IEEE) 3

Figure 1–3. The integration on the market of SiC/GaN-based applications (© 2014 IEEE [6]– Adapted with permission from the IEEE) 3

Figure 1–4. Component cost structure per topology and switching frequency fsw. Σ misc is the PCB and IC costs, ΣC is the total capacitor cost and ΣCS is the cooling system cost. ΣL is the inductor cost and ΣSC is the semi-conductor cost. Where the output LCL filter is included in this analysis. (© 2013 IEEE [8] – Adapted with permission from the IEEE) 4

Figure 1–5. Volume breakdown of the employed component for different switching frequencies f sw. VC is the total capacitor volume, VL the total inductor volume and Vsink the volume of the required heat sink. (© 2013 IEEE [9]– Adapted with permission from the IEEE) 5

Figure 1–6. PV panels insulations [18] (Adapted with permission from The National Renewable Energy Laboratory [18]) 6

Figure 1–7. U.S. Utility PV Pipeline [20] (Adapted with permission from the from Solar Energy Industries Association, Inc® [20]) 7

Figure 1–8. U.S. Quarterly PV Installations by Market Segment [20] (Adapted with permission from the from Solar Energy Industries Association, Inc® [20]) 7

Figure 1–9. U.S. Renewable Electricity Nameplate Capacity by Source [19] (Adapted with permission from The National Renewable Energy Laboratory [19]) 8

Figure 1–10. Essential PV Power Plant Features[2] 9

Figure 1–11. Typical utility scale PV Farms structures[26] 9

Figure 1–12. Data center energy consumption prediction (Adapted with permission from Analytics Press [29]) 11

Figure 2–1. U.S electric nameplate capacity in 2013 [19]. (Adapted with permission from The National Renewable Energy Laboratory [19]) 15

Figure 2–2. Cost of different PV-converter concepts (Adapted with permission from Elsevier [35]) 16

Figure 2–3. Grid-connected PV system using an inverter with galvanic isolation (a) grid-side low-frequency (LF) transformer (b) DC side high-frequency (HF) transformer [36] 17

Figure 2–4. Grid connected PV system with transformer less inverter [36] 18

Figure 2–5. Overall efficiency for AC and DC wind farm (© 2013 IEEE [39]– Adapted with permission from the IEEE) 19

Figure 2–6. Location of Eggebek Solar Park [41] (Adapted with permission from Wikipedia [41]) 21

Figure 2–7. Eggebeck PV farm outline [23] 22

Figure 2–8. Proposed PV farm architecture 24

Figure 2–9. Typical three phase inverter with filter 25

Figure 2–10. VSI Filter transfer function 27

Figure 2–11. Max efficiency flow chart [17] 29

Figure 2–12. Min size flow chart [17] 29

Figure 2–13. Max efficiency transformer flux utilization ratio 31

Figure 2–14. Max efficiency transformer area product 31

Figure 2–15. Max efficiency transformer parameters expected efficiency 31

Figure 2–16. Max efficiency transformer leakage inductance 31

Figure 2–17. Min size transformer flux utilization ratio 32

Figure 2–18. Min size transformer parameters area product 32

Figure 2–19. Min size transformer parameters expected efficiency 32

Figure 2–20. Min size transformer leakage inductance 32

Figure 2–21. Metglass2605SA1 BH curve[45] 33

Figure 2–22. Metglass2605SA1 Core Loss at 1kHz[45] 33

Figure 2–23. Transformer FEA 3D model in ANSYS Comsol 34

Figure 2–24. Transformer time domain (a) primary voltage(b)primary current (c)secondary voltage(d)secondary current as generated by ANSYS Comsol FEA simulation 35

Figure 2–25. Transformer core losses as generated by ANSYS Comsol FEA simulation 35

Figure 2–26. Transformer 3D flux distribution at time = 12ms as generated by ANSYS Comsol simulation 36

Figure 2–27. cables in the proposed medium frequency structure 38

Figure 2–28. PI section modeling for power cable [46] 39

Figure 2–29. LV cable impedance frequency response 40

Figure 2–30. MV cable impedance frequency response 40

Figure 2–31. Three phase to three phase cycloconverter structure 41

Figure 2–32. Block diagram for PV farm sector arrangement 43

Figure 2–33. Block diagram for the PV inverter voltage controller 43

Figure 2–34. Block diagram for the cycloconverter controller 44

Figure 2–35. Flow chart for the inverter PV algorithm 46

Figure 2–36. Flow chart for the cycloconverter controller 46

Figure 2–37. The system simulation in PLECS 47

Figure 2–38. PV inverters synchronous reference frame voltage closed loop time domain command tracking response for different power levels 49

Figure 2–39. PV inverter line voltage time domain waveforms during different loading conditions (right) zoomed out view (left) zoomed in view 50

Figure 2–40. PV inverter line current time domain waveforms during different loading conditions (right) zoomed out view (left) zoomed in view 51

Figure 2–41. medium frequency network time domain waveforms voltage and current during different loading conditions (right) zoomed out view (left) zoomed in view 52

Figure 2–42. Cycloconverter active and reactive power closed loop time domain command tracking time domain response for different insulation levels 52

Figure 2–43. Cycloconverter time domain input voltage, input current and output switching voltage (right) zoomed out view (left) zoomed in view 53

Figure 2–44. Time domain grid voltage and grid injected current during different loading conditions (right) zoomed out view (left) zoomed in view 54

Figure 2–45. System simulation block diagram in PLECS at faulty condition 55

Figure 2–46. PV inverters synchronous reference frame voltage closed loop time domain command tracking response during normal and faulty condition 56

Figure 2–47. PV inverter line voltage time domain waveforms during normal and faulty condition (right) zoomed out view (left) zoomed in view 57

Figure 2–48. PV inverter line current time domain waveforms during normal and faulty condition (right) zoomed out view (left) zoomed in view 58

Figure 2–49. Medium Frequency grid time domain voltage and current waveforms during normal and faulty condition (right) zoomed out view (left) zoomed in view 59

Figure 2–50. Cycloconverter active and reactive power closed loop time domain command tracking time domain response for normal loading and faulty condition 59

Figure 2–51. Cycloconverter time domain input voltage, input current and output switching voltage waveforms during normal and faulty condition (right) zoomed out view (left) zoomed in view 60

Figure 2–52. Time domain grid voltage and grid injected current during normal loading and faulty conditions (right) zoomed out view (left) zoomed in view 61

Figure 2–53. Overall system efficiency 62

Figure 3–1. Power requirement for a typical data center [54] 64

Figure 3–2. Conventional 480V data center structure [60] 66

Figure 3–3. Medium voltage based data center architecture [60] 66

Figure 3–4. proposed data center structure based on MV-MF transformer 67

Figure 3–5. Details of the proposed data center MF-MV architecture using three limbs transformer 68

Figure 3–6. Details of the proposed data center MF-MV architecture using five limbs transformer 69

Figure 3–7. The flipped(modulated) grid input voltage waveform after the AC to AC converter 73

Figure 3–8. FFT of the medium frequency modulated grid voltage (transformer voltage) 73

Figure 3–9. Max efficiency transformer flux utilization ratio 75

Figure 3–10. Max efficiency transformer area product 75

Figure 3–11. Max efficiency transformer expected efficiency 76

Figure 3–12. Max efficiency transformer leakage inductance 76

Figure 3–13. Min size transformer flux utilization ratio 76

Figure 3–14. Min size transformer area product 76

Figure 3–15. Min size transformer expected efficiency 77

Figure 3–16. Min size transformer leakage inductance 77

Figure 3–17. Three limbs – three phase transformer 78

Figure 3–18. Five limbs – three phase transformer 78

Figure 3–19. Time domain wave forms for three limbs transformer (a)primary voltages (c) secondary voltages , five limbs transformer(b) primary voltages (d) secondary voltages 79

Figure 3–20. Time domain wave forms for three limbs transformer (a)primary currents (c) secondary currents , five limbs transformer(b) primary currents (d) secondary currents 80

Figure 3–21. Time domain waveforms for the proposed structure with different dead bands (a) three Limbs primary currents (b) five limbs primary

currents(c) three limbs secondary voltage (d) five limbs secondary voltages (e) three limbs secondary currents (f) five limbs secondary currents 81

Figure 3–22. Frequency domain response for the three limb- three phase transformer line current in case of no dead band 82

Figure 3–23. Zoomed in view for the frequency domain graphs for the three limbs and five limbs transformer designs during no deadband and with different deadband simualtions at 940Hz,300Hz and 5000Hz 83

Figure 3–24. Neutral current time domain waveforms for three limbs and five limbs transforms with and without different deadband simualtions 83

Figure 3–25. Flux distribution for the three limbs transformer at 46 msec 84

Figure 3–26. Flux distribution for the five limbs transformer at 46 msec 85

Figure 3–27. Three limbs and five limbs transformers core losses 85

Figure 3–28. Output voltage waveform for the three phase PWM inverter 86

Figure 3–29. Input voltage and current for the three single phase PFC 87

Figure 3–30. Output voltage waveforms for the three single PFC 88

Figure 3–31. grid filtered input voltages/currents 89

Figure 3–32. grid unfiltered voltage/current 89

Figure 4–1. PV farm lab setup arrangement 92

Figure 4–2. Actual PV farm lab complete setup 94

Figure 4–3. Actual PV farm setup inverters 95

Figure 4–4. Steady state time domain waveforms for min inverter voltage cases scope 1 96

Figure 4–5. Steady state time domain waveforms for min inverter voltage cases scope 2 97

Figure 4–6. Steady state time domain waveforms for normal inverter voltage cases scope 1 98

Figure 4–7. Steady state time domain waveforms for normal inverter voltage cases scope 2 98

Figure 4–8. Steady state time domain waveforms for maximum inverter voltage cases scope 1 99

Figure 4–9. Steady state time domain waveforms for maximum inverter voltage cases scope 2 99

Figure 4–10. Steady state time domain waveforms for zero inverter voltage cases scope 1 100

Figure 4–11. Steady state time domain waveforms for zero inverter voltage cases scope 2 100

Figure 4–12. Minimum to maximum inverter voltage cased transient time domain waveforms scope 1 101

Figure 4–13. Minimum to maximum inverter voltage cased transient time domain waveforms scope 2 102

Figure 4–14. Minimum to zero inverter voltage cased transient time domain waveforms scope 1 103

Figure 4–15. Minimum to zero inverter voltage cased transient time domain waveforms scope 2 103

Figure 4–16. Zero to normal inverter voltage cased transient time domain waveforms scope 1 104

Figure 4–17. Zero to normal inverter voltage cased transient time domain waveforms scope 2 104

Figure 4–18. Data center lab setup arrangement 105

Figure 4–19. Data center actual lab setup 106

Figure 4–20. Steady state time domain waveforms for data center with identical dead band resistive load scope 1 107

Figure 4–21. Steady state time domain waveforms for data center with identical dead band resistive load scope 2 107

Figure 4–22. Steady state time domain waveforms for data center with different dead band resistive load scope 1 108

Figure 4–23. Steady state time domain waveforms for data center with different dead band resistive load scope 2 108

Figure 4–24. Steady state time domain waveforms for data center with identical dead band boost PFC load scope 1 109

Figure 4–25. Steady state time domain waveforms for data center with identical dead band boost PFC load scope 2 110

Figure 4–26. Steady state time domain waveforms for data center with different dead band boost PFC load scope 1 111

Figure 4–27. Steady state time domain waveforms for data center with different dead band boost PFC load scope 2 111

LIST OF TABLES

Page

Table 2-1. PV inverter interface options with utility grid comparison [40] 20

Table 2-2.Three Phase Inverter/Filter Parameters 26

Table 2-3. PV Farm Transformer specifications 28

Table 2-4. Eggebek layout/cable summary 37

Table 2-5. Proposed Eggebek layout/cable summary 38

Table 2-6. Collection grid simulation time instant insulation level change summary 48

Table 3-1. Data Center Load information [54] 71

Table 3-2. Devices selected for the proposed structure 71

Table 3-3. Data center Transformer specifications 74

Table 4-1. PV setup circuit parameters 93

Table 4-2. PV Different cases voltages 94

1. INTRODUCTION

The fact that the loads are located far from the generation forced the power system structure, theory and regulations; the main focus is to supply the loads with the required voltage/current maintaining the highest reliability and in the most efficient conditions. Before power electronics, the voltage level was the only degree of freedom (i.e. the control parameter); hence, the transformer was the key controlling element. The generators' output voltages is limited by its insulation level, then the transformer is used to increase the voltage level to increase the transmission efficiency, several transformers are used at the transmission line receiving end to step down the voltage as required by the load [1].

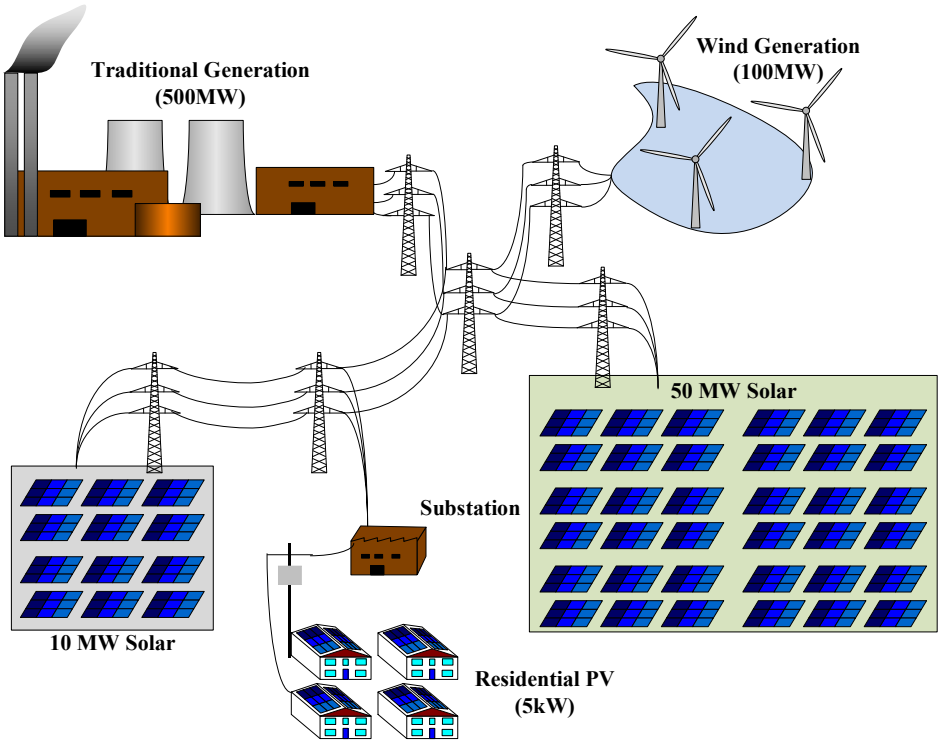

Figure 1–1. Typical power system structure that include traditional and renewable energy sources [2]

The power electronics devices added altering the voltage frequency as a new system's degree of freedom, this results in more flexible power system architectures. This added flexibility was an essential factor to include the renewable energy sources in the conventional power systems as shown in Figure 1–1[2]. Now, the input and the output of the power electronics based converter could be of different voltage and frequency levels. This conversion process could be done in different stages with different combinations based on the input and output voltage amplitude /frequency and the system requirements such as efficiency, reliability …etc.[3]

Wide Band Gap (WBG) devices resulted from the continuous improvement in the power electronic devices technology. These devices come in two main categories; Silicon Carbide (SiC) devices and Gallium Nitride (GaN). Compared to the conventional Silicon (Si) devices, The WBG devices have higher blocking voltage, lower losses and higher switching frequencies and high reliability (Figure 1–2) [4, 5]. These devices open the door for a higher dense power electronics converter across all the industrial markets such as motor drives, photovoltaic (PV) inverters, automotive industry …etc. (Figure 1–3 [6]).

This work focuses on developing high dense power architectures for both PV Farms and Data Centers (DS) taking advantages of aforementioned device improvements. The fact that the WBG devices can switch at higher frequencies with high efficiency enables replacing bulky passive components (i.e. inductors, transformers and capacitors) with smaller counterparts hence results in a dense power converter stages.

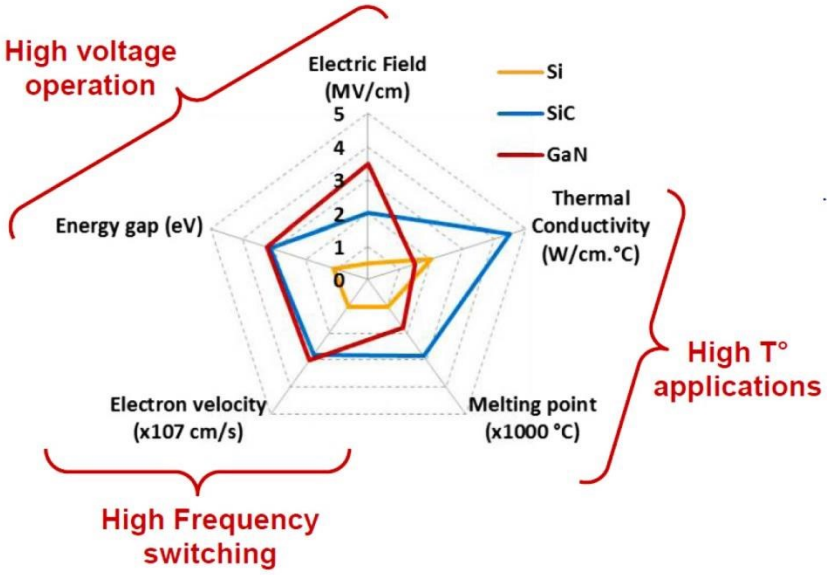

Figure 1–2. Summary of Si, SiC and GaN relevant material properties (© 2014 IEEE [7]– Adapted with permission from the IEEE)

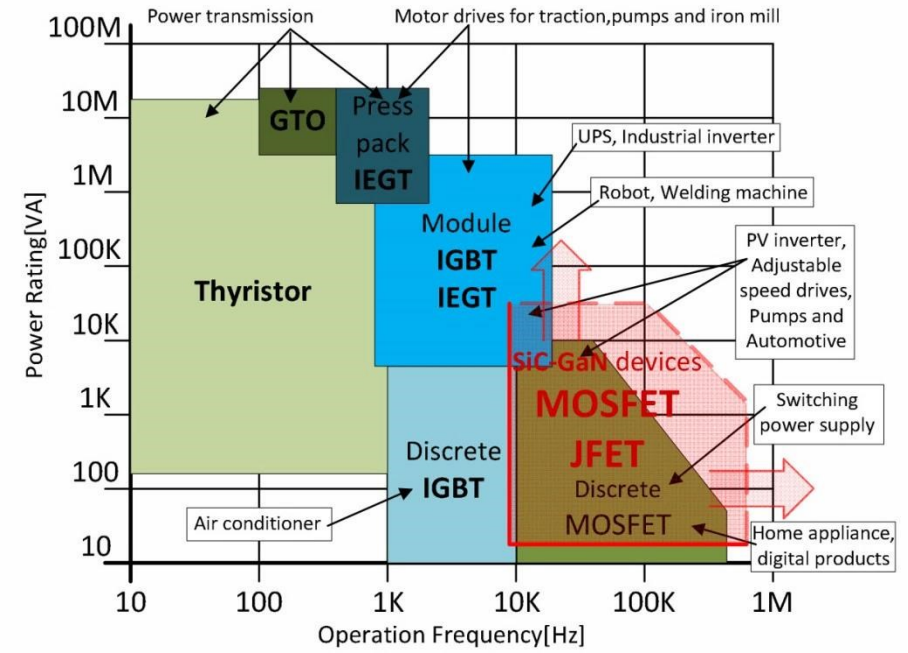

Figure 1–3. The integration on the market of SiC/GaN-based applications (© 2014 IEEE [6]– Adapted with permission from the IEEE)

1.1. High Density Power Supply

The power electronics converter comprise power electronics switches with its auxiliary gate drive circuits, voltage and current sensors, capacitors, inductors and heat sinks and transformers. The price and volume break down for five different topologies of 10 kW three phase inverter, (2LVSI – 2level voltage source inverter, 2LZSI - 2Level Z-source inverter, 2LVSI+BC - 2level VSI with adjusting input side DC/DC boost converter, 3LI+BC - 3level I-type topology with boost converter, 3LT+BC - 3level T-type topology with boost converter), are shown in (Figure 1–4, Figure 1–5 [8, 9]), it can be seen that the inductor forms a major part of the inverter volume and cost, in some adjustable speed drive cases it can reach up to 50% of the inverter size itself [10].

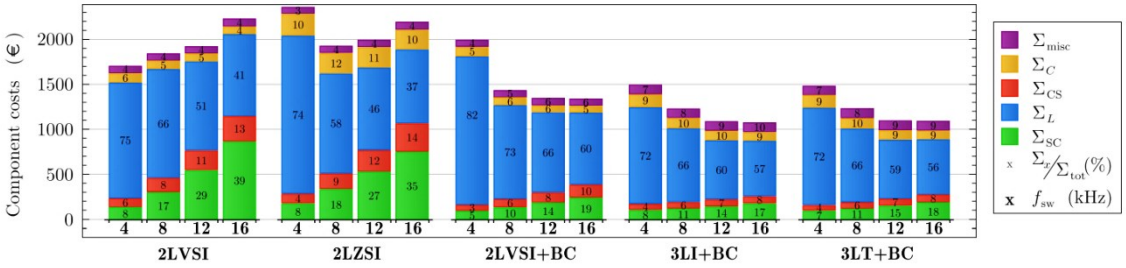

Figure 1–4. Component cost structure per topology and switching frequency f_{sw}. Σ_{misc} is the PCB and IC costs, Σ_C is the total capacitor cost and Σ_{CS} is the cooling system cost. Σ_L is the inductor cost and Σ_{SC} is the semi-conductor cost. Where the output LCL filter is included in this analysis. (© 2013 IEEE [8] – Adapted with permission from the IEEE)

If galvanic isolation is required in the system a low frequency transformer will add to a the total system size by major part and in some cases it can be half the system size so most of the efforts towards the increasing the density of the power converter targeted operating the transformer at higher frequency levels in what is called Solid State Transformer (SST) and it was adopted across different fields such as wind farms, PV

micro grids, traction application …etc[11-16]. Therefore, the key to high dense power converter is to optimize the converter's magnetic based components (i.e. transformer and inductors).

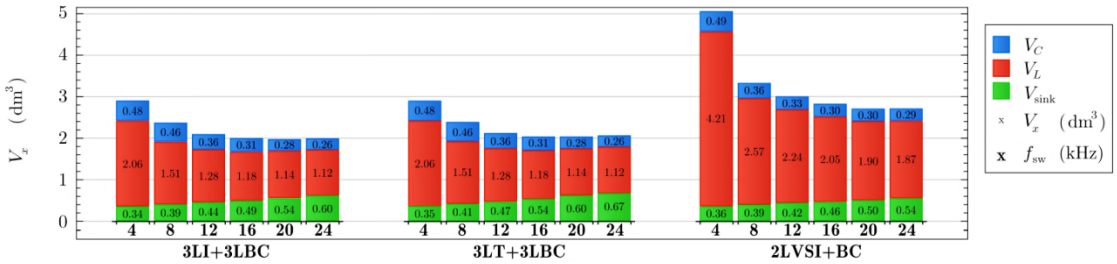

Figure 1–5. Volume breakdown of the employed component for different switching frequencies f sw. VC is the total capacitor volume, VL the total inductor volume and Vsink the volume of the required heat sink. (© 2013 IEEE [9]– Adapted with permission from the IEEE)

A transformer core can carry the same amount of flux lines at a smaller area (assuming same flux density) by increasing the operating frequency as indicated by (1-1), however, this may lead to higher losses if the operating flux density is not chosen appropriately. Several cores could be chosen from starting with conventional silicon steel passing through amorphous cores till reaching the nano-crystalline cores. The first will suffer from high losses compared to the latter two but it has lower price [17]. So the optimization in this work is to design the transformer at medium frequency range (0.5 to 2 kHz) to enable usage of relatively low cost material such as silicon still or amorphous cores while decreasing the size of the core and increasing the power converter density.

$$V = 4.44fNaB \tag{1-1}$$

Where V is the transformer voltage, f is the operating frequency, N is the number of turns, a is the cross section area and B is the operating flux density

1.2. Utility Scale PV Farm

Solar photovoltaic (PV) installations are one of the fastest growing renewable energy installations and these installations range from several watts to several Megawatts (Figure 1–6) and it can always be integrated to the utility grid (Figure 1–1).

Figure 1–6. PV panels insulations [18] (Adapted with permission from The National Renewable Energy Laboratory [18])

In 2013, the U.S. PV installed capacity was 4751 MW with a 41% increase when compared the year before (Figure 1–8, Figure 1–9) and 64% from 2000 to 2013 and the U.S Department of Energy (DoE) studies indicates that the PV installations increase year after year (Figure 1–9) [19, 20]. This increase is derived by fossil fuel depletion predications, environmental awareness and economical profit. Year after year, the research efforts in PV technology overcome the challenges that face PV integration

to the grid such as PV collecting grid architecture, reliability, efficiency, plant level control, remote monitoring, protection and advanced grid friendly features [2, 21, 22].

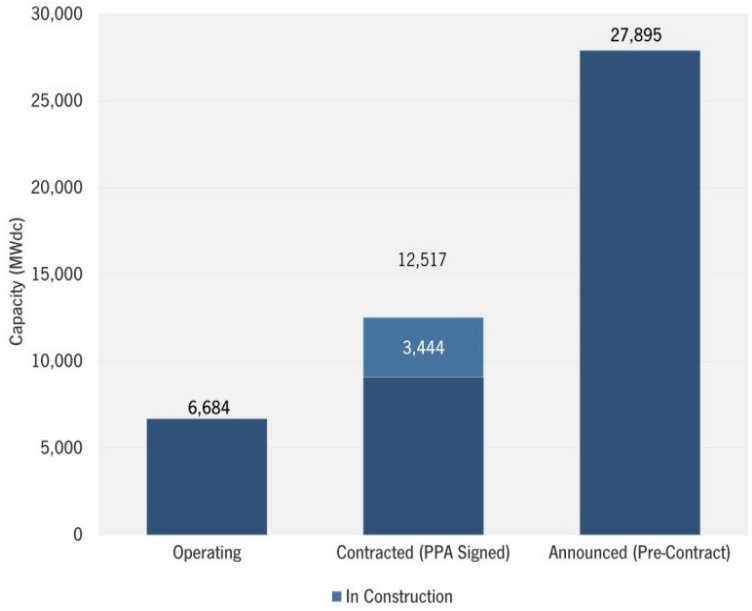

Figure 1–7. U.S. Utility PV Pipeline [20] (Adapted with permission from the from Solar Energy Industries Association, Inc® [20])

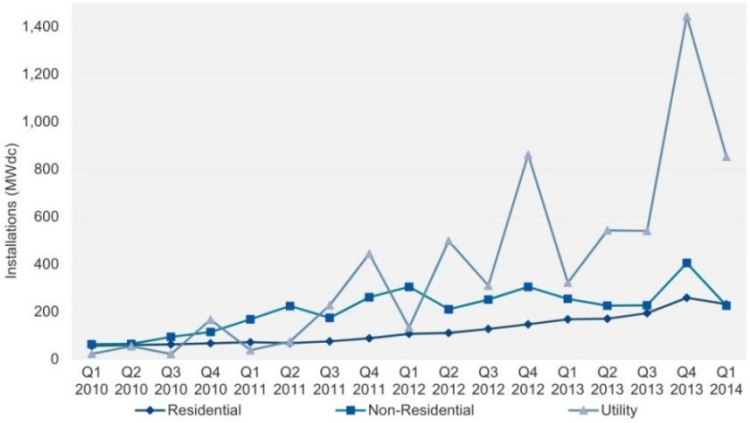

Figure 1–8. U.S. Quarterly PV Installations by Market Segment [20] (Adapted with permission from the from Solar Energy Industries Association, Inc® [20])

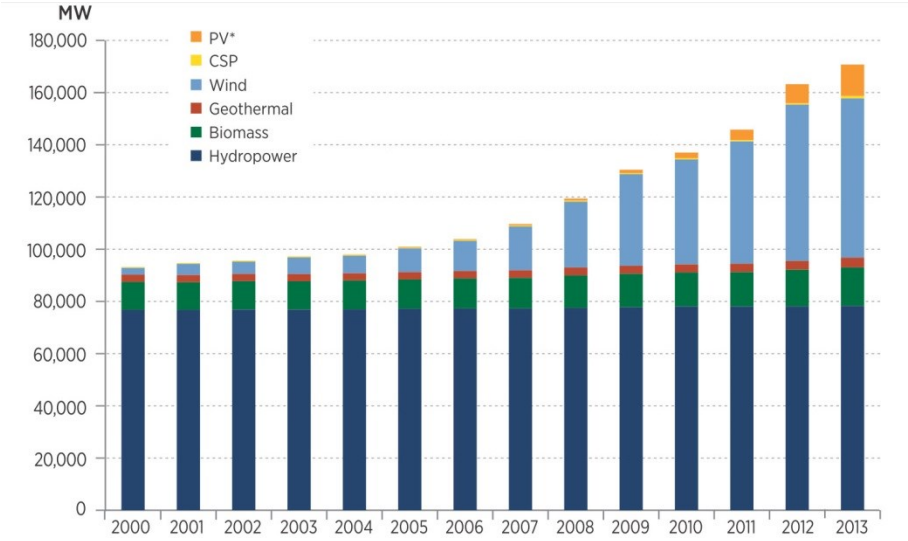

Figure 1–9. U.S. Renewable Electricity Nameplate Capacity by Source [19] (Adapted with permission from The National Renewable Energy Laboratory [19])

A typical DC panel generates 240 Watts at about 42 V DC [23]. In PV farms, The PV panels are connected in series/parallel combination to generate a specific amount of power and construct a specific DC output voltage. The power electronics converters, which interface the PV panels to the grid, must extract the maximum amount of power from the PV panels, which is known by maximum power point tracking (MPPT), with minimum losses, afterwards a line frequency transformer provides electric isolation between the PV panels and the utility grid [24, 25]. Several structures can be employed for the power electronics converters such as central converter, string converter with common DC bus, string converter with common AC bus (Figure 1–11)[26]. The tradeoffs between the aforementioned are modularity, efficiency, MPPT behavior during different shading conditions [18, 27, 28].

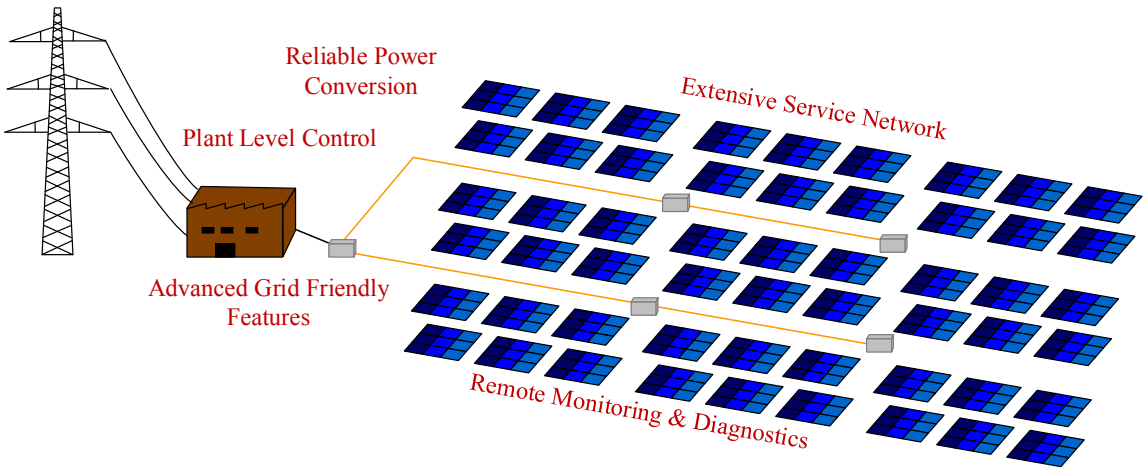

Figure 1–10. Essential PV Power Plant Features[2]

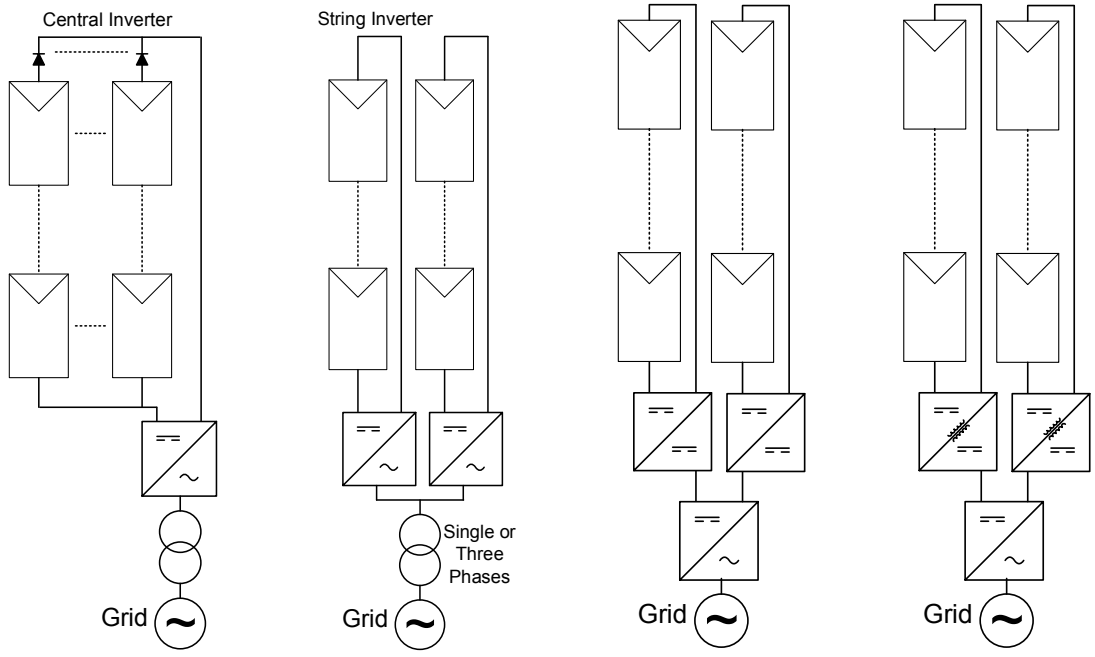

Figure 1–11. Typical utility scale PV Farms structures[26]

The first part of this research work presents new power architecture for PV farm that employ sinusoidal medium frequency voltage on the transformer to take advantage

of the passive elements size reduction. The proposed architecture is modular in nature therefore it enhances the system expandability and integration cost. A complete system analysis was carried out to ensure the system performance in the medium frequency range. Finally a new controller was introduced and implemented for the system operation that showed high robustness and fast dynamic performance.

1.3. Data Center

Total electricity usage by data centers in 2010 was estimated to be 1.3%, Figure 1–12, of all electricity use for the world and 2% of all electricity use for the US equal to annual electricity costs of $7.4 billion [29]. In 2011, Emerson estimated the total number of data center worldwide to be 510,000 where 6,500 of them consumes electricity equal to the state of Utah [30, 31]. In 2015, the data center is expected to consume 360B kWh[31].

If the current trend persists, global data center carbon dioxide emissions are poised to equal that of the airline industry; almost quadrupling between 2010 and 2020 [32]. This makes it important for researchers to investigate better architectures to improve the efficiency and power density of future data center power converters which was the first and third most commanded data center features by 1500 company CIO's in a survey conducted by Gartner Executive Programs (EXP) in 2009 [33].

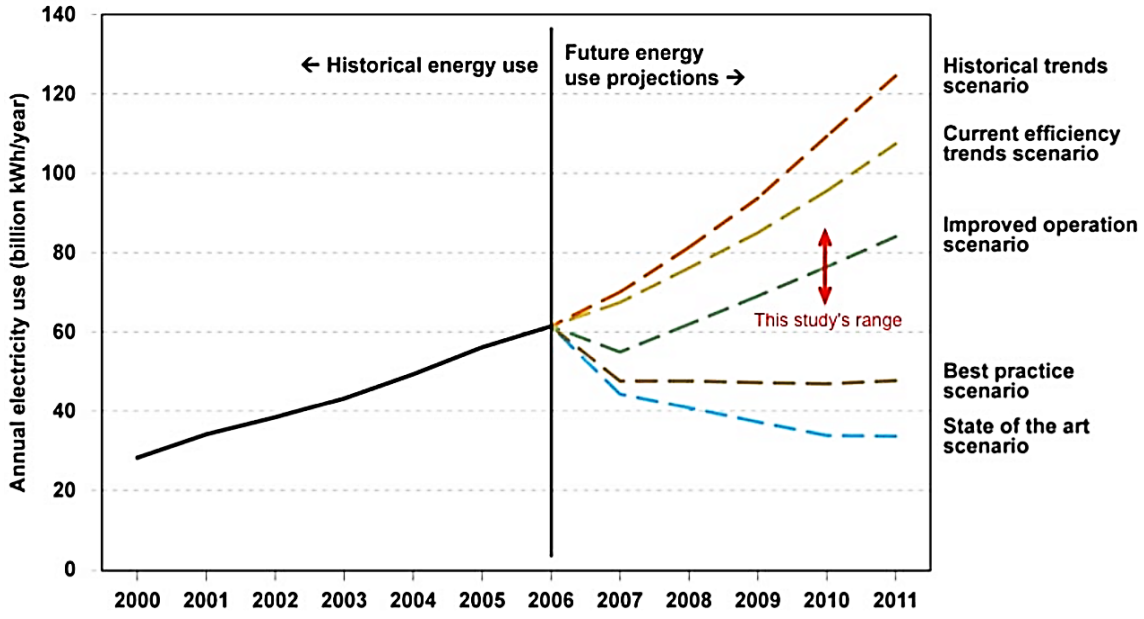

Figure 1–12. Data center energy consumption prediction (Adapted with permission from Analytics Press [29])

The second part of this research work focuses on developing a new architecture for data center based on implementing medium frequency concepts with minimal modification on the system inputs and outputs. The proposed structure maintained the same input grid voltage level and provided the required load voltage level.

1.4. Research Objective

High dense power converters is the one of the newly added targets to the power electronics converter features' list that includes high reliability, high efficiency and flexibility of operations. The advancement of power electronics switches and the WBG devices technology provides the required tool to combine all the aforementioned features in power electronics converters.

This research focuses on developing new power architecture for both utility scale PV farms and data center by employing medium frequency voltages.

The first part of this dissertation is focused on utility scale PV farms, the proposed architecture is developed using modular inverter transformer stages, each comprise several parallel connected inverters that are connected to the input of a medium frequency transformer. The transformer outputs of each stage are series connected to construct the medium frequency medium frequency PV farm collection grid. Afterwards, a Thyristor based ac to ac converter is used to convert the medium frequency voltage to a low frequency voltage which is the final stage required for grid integration. A thorough analysis for the system components will be presented that includes power electronics components selection, passive elements selection and transformer design and verification using Finite Element Analysis (FEA) software comparing different magnetic materials for cores. A new control strategy was developed for the proposed structure, extensive simulation results that shows the system performance under normal and faulty conditions are presented. Finally a scaled down lab prototype is built and tested in different conditions to proof the validity of proposed structure and its control.

The second part focuses on developing high dense power architecture for data center power supply. The main idea is to convert the input sinusoidal voltage to pulsating sinusoidal voltage at medium frequency using ac to ac converter; this will decrease the transformer size as it will process the power at medium frequency. The intermediate stage for the ac to ac converter is a week dc link, this result in a small size capacitor requirement within the proposed structure. Two three phase transformer

designs are investigated using FEA simulation; one with three limbs and the other with five limbs and the best is selected for the final implementation. A complete system simulation is performed and a scaled down prototype for the system is implemented to validate the proposed structure.

1.5. Outline of Dissertation

This work is divided in to five sections. Section 1 gives an introduction about high density power converter and points out the opportunities to build on. Afterwards give a motivational background about the utility scale PV farms and data center power supplies and shows the importance of developing new solutions for them. The section ends by declaring the research objective.

Section 2 focuses on the proposed architecture for the utility scale PV farm. It starts with a literature survey about the current PV structure and then details a state of the art PV farm in Germany. The proposed structure is given considering the same PV farm data. Then a detailed analysis of the structure is given. A control strategy is also presented and tested in different cases to validate its robustness.

Section 3 shows the proposed high density power converter for data center. It starts with literature survey on the data center power supply. Afterwards, a detailed analysis of the system is presented. Extensive FEA models for two transformer designs are investigated and the best solution is recommended.

Hardware experimental results for the two proposed systems are shown in Section 4. The showed experimental results prove the validity of the proposed structure

and their controller robustness during different operating condition and during transient periods.

Finally, the final conclusion and summary are presented in Section 5 and the future research opportunities are revealed.

2. UTILITY SCALE PHOTOVOLTAIC FARMS

The U.S. PV penetration as a renewable energy source in 2013 is about 1.1% of the total renewable energy generation that is 15% of the total energy generated (Figure 2–1), the US department of energy is expecting that this will increase to 20% in year 2050 [19].

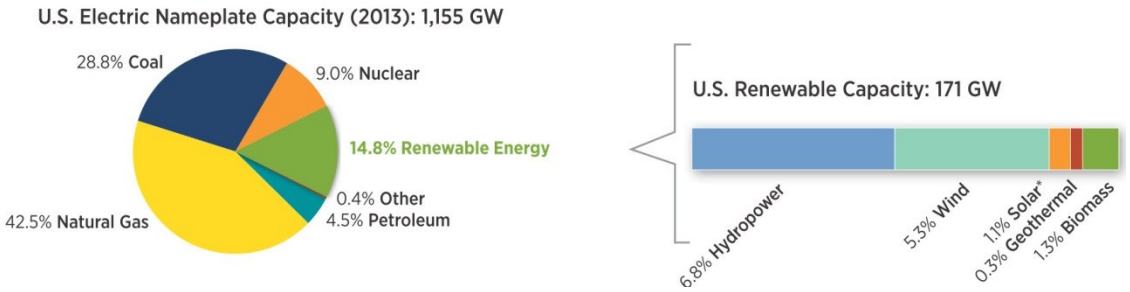

Figure 2–1. U.S electric nameplate capacity in 2013 [19]. (Adapted with permission from The National Renewable Energy Laboratory [19])

This requires high dense and more efficient utility scale PV farm architecture. This section of the dissertation introduces a detailed proposal for the utility scale PV farm architecture that employs medium frequency transformers. The section starts by an overview of the current structures and shows the merits of the proposed architecture compared to them. A case study for an actual utility scale PV farm will form the basis for comparison between the proposed and the current state of the art utility scale PV farms. A complete system analysis is presented to investigate the feasibility of the proposal that includes a FEA of the transformer design. Afterwards, a system controller is showed and a thorough simulation cases are presented to test the controller robustness

and dynamic performance. This section will end by a summary and a conclusion for the main findings of this proposal.

2.1. Introduction/Existing Architecture

As mentioned in the first section, several structures can be implemented to harness the sun power (Figure 1–11). Central, multi-string structures are most economical for megawatt scale PV farms and results in the lowest watts per dollar as shown in Figure 2–2. Economic studies were carried out to determine the optimum range for the inverter unit that should be used to construct a megawatts scale PV farm and the investigation of concludes that based on existing inverter technology at present, the economical size of inverters range from 8 kW to 100 kW[34].

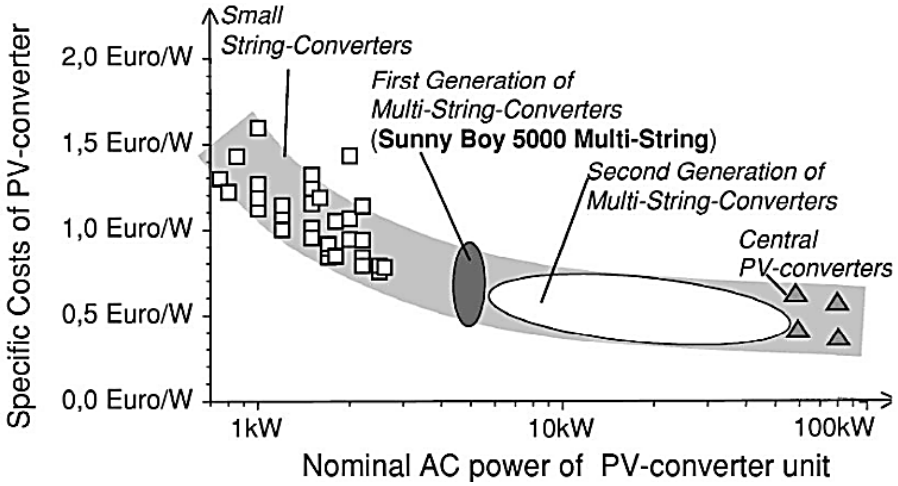

Figure 2–2. Cost of different PV-converter concepts (Adapted with permission from Elsevier [35])

The electrical (galvanic) isolation between the PV panels and the utility grid is one requirement for the PV farm. The inverter can either be isolated on not isolated from the grid. The transformer provides this isolation in two main ways, either in low

frequency (Figure 2–3-a) or at high frequency with intermediate DC stage introduced in the conversion stage (Figure 2–3-b). The transformer with low frequency will have bigger size compared to the high frequency transformer; however, adding the extra conversion stage will decrease the overall system efficiency. Some countries such as UK, Italy and US require galvanic isolation but other countries such as Germany and Spain galvanic isolation is not mandated. As system with no galvanic isolation contains only the inverter stage without the transformer is shown in Figure 2–4.

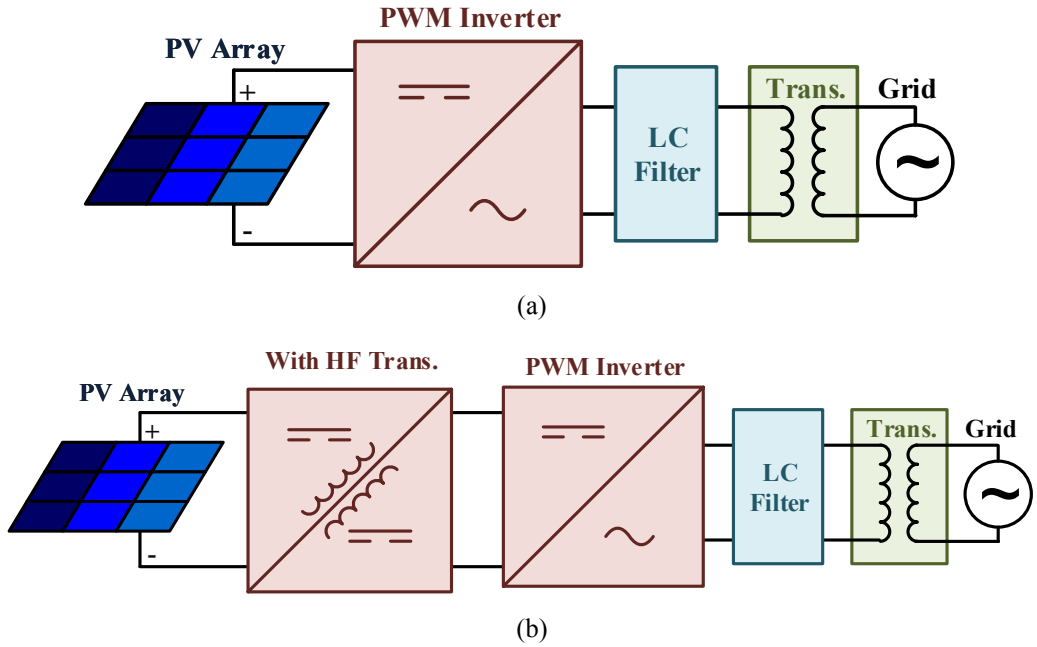

Figure 2–3. Grid-connected PV system using an inverter with galvanic isolation (a) grid-side low-frequency (LF) transformer (b) DC side high-frequency (HF) transformer [36]

The DC connection, based on HF transformer (Figure 2–3-b), of the semi string PV farm structure is investigated and compared considering different metrics such as system modularity, efficiency, reliability, cost and DC connectivity and it showed that

these systems are promising however they suffer from the high price due to usage of HF transformers that requires pricy core materials [37].

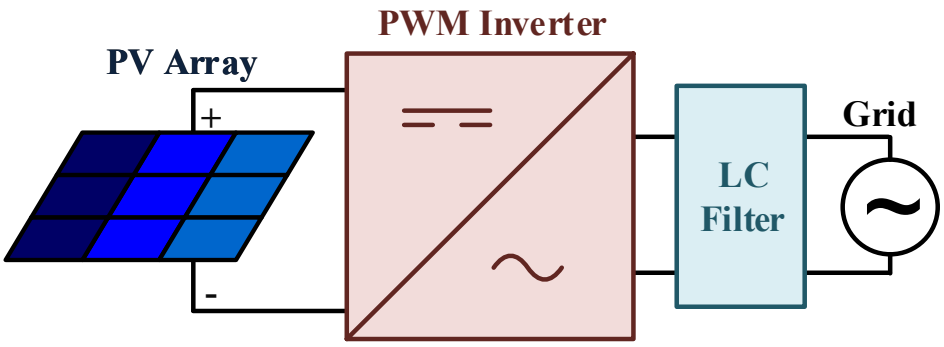

Figure 2–4. Grid connected PV system with transformer less inverter [36]

All of the Smart transformer (ST) have intermitted DC link. A tradeoff between increasing the transformer switching frequency, to increase the converter power density, and the price of the core materials should come to play and the answer to that is to build the inner farm collection grid using medium frequency voltage as in [38]. The same solution investigated in wind farms in [39]. Figure 2–5 shows a summery for the results, it can be noted that the increase of the collection grid frequency improves the overall efficiency if the system is well designed plus it decreases the system passive components size. The main limiting factor for this is the cable losses and reactive power consumption, in this study, the cable length was 5km.

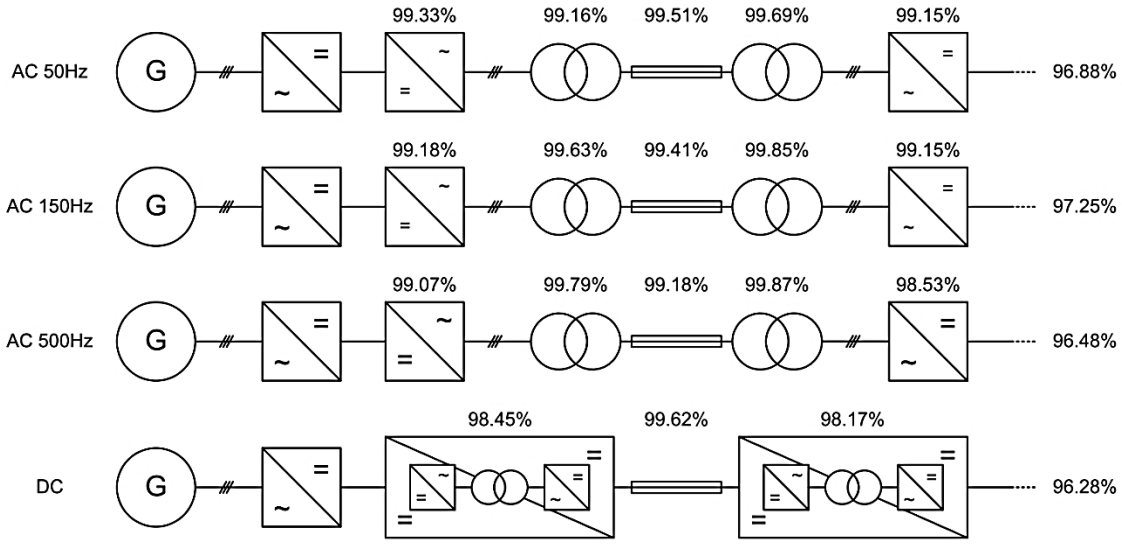

Figure 2–5. Overall efficiency for AC and DC wind farm (© 2013 IEEE [39]– Adapted with permission from the IEEE)

A summery for a comparison between three interface types between the PV inverters and the utility grid is in Table 2-1 [40]. The DC bus is assumed to provide no galvanic isolation in this comparison. The High Frequency AC (HFAC) grid frequency value is left undetermined as a design parameter. As can be note, the AC collection grid in general will be the only option if the galvanic isolation is one of the requirements as in our case. Since the length of the cable will be limited to small section the cons of the HFAC system will be minimal. The proposed structure in the coming section will have a robust control structure yet simple hence the second challenge in the system is checked of the demerit's list. The coming section will outline the proposed structure in details and shows the list of merits that could be gained over the 60 Hz AC bus counterpart.

TABLE 2-1. PV INVERTER INTERFACE OPTIONS WITH UTILITY GRID COMPARISON [40]

Interface Type	DC bus	60 Hz AC bus	HFAC bus
Merits	- Higher reliability - Lower losses - Longer grid length - Lower costs - High power density due to elimination of magnetic transformer	- Higher reliability - Easier connection to the utility grid - Possible galvanic isolation - Easier adjustment of voltage levels - Lower average costs	- Lower volume and weight - Improvement of fluorescent lighting - Direct connection high frequency motors and compressors - Smaller passive elements - Galvanic isolation with smaller high frequency transformers
Demerits	- High volume and weight due to electrolytic capacitor - Less compatibility of voltage levels - Higher corrosion of electrodes - No galvanic isolation	- High volume and weight - Stringent synchronization requirement - Higher load effects - Reduced grid length - Bulky line frequency transformer	- Smaller grid length - Higher cost - Complexity of design and control - Increase in voltage drops and power losses in the line
Applications	- Renewable source with DC output - Requirement for longer grid length	- Renewable sources with variable AC output - Direct connection through induction generator - Requirement for galvanic isolation	- Any renewable sources - Requirement of smaller volume and weight higher power density

2.2. Case Study

Eggebek solar park is a PV farm in north part of Germany (Figure 2–6) that generates 80 MW of electric power and it is considered one of the biggest PV farms all over the world [23], its data will be used for comparison as a design example. Its layout is shown in Figure 2–7; a semi-string structure is employed to construct the collection grid. Each three phase VSI is used to process 100kW at 480V/60Hz, afterwards all the inverters are connected in parallel to a line frequency transformer that steps up the voltage forty times. This system suffers from two main drawbacks:

1. A transformer with a high turns' ratio (40) which is hard to manufacture.
2. The PV collection grid is of low voltage that results in high current and high losses in the cables.

Figure 2–6. Location of Eggebek Solar Park [41] (Adapted with permission from Wikipedia [41])

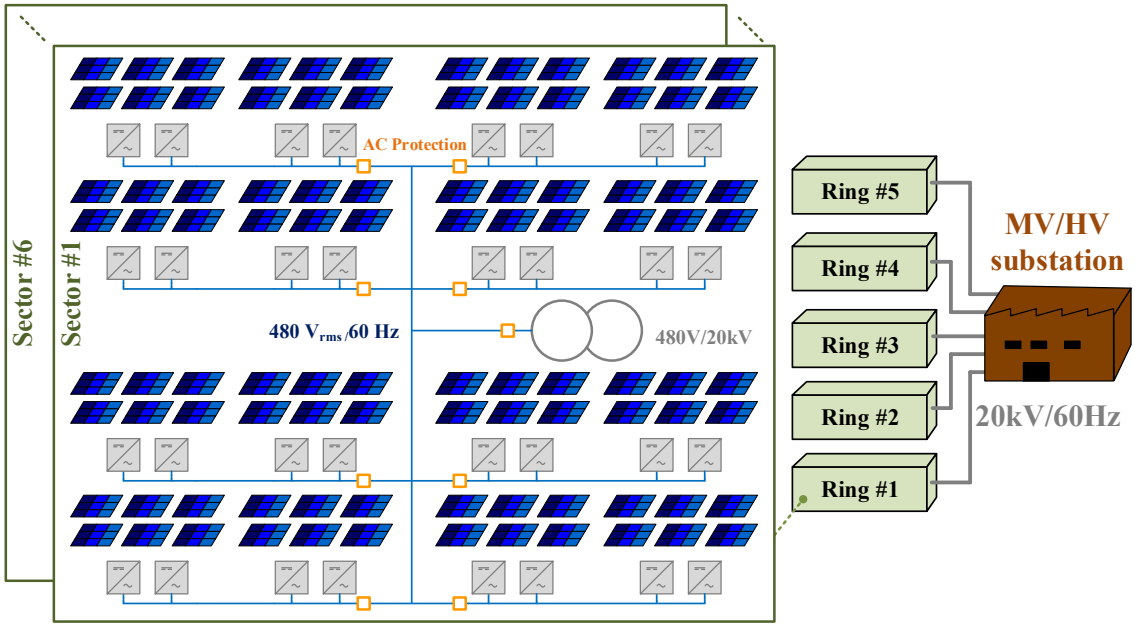

Figure 2–7. Eggebeck PV farm outline [23]

2.3. Proposed Medium Frequency AC Collection Grid

The proposed MF-MV in Figure 2–8 overcomes these two main drawbacks. The three phase VSI generates 600V/1000Hz. Distributed MF transformers will step up this voltage and their outputs are cascaded to construct the MV for the collecting grid. A three phase cyclo-converter converts the MV-MF voltage to the grid voltage.

The advantages of the proposed MV-MF PV grid are summarized in the following points

- The distributed MF transformer provides the required isolation between the PV and the power grid

- The proposed PV grid architecture is modular that increase the system expansion ability, facilitate independent operation, decrease cost and reduce repair mean time [37].
- The MF transformers are cascaded to construct the MV-MF PV collection grid, therefore the three phase VSI will be subjected to low voltage level that allow usage of Lower voltage IGBTs/MOSFETs while maintaining a low transformer turns' ratio.
- The overall efficiency of the grid is expected to be high since the AC collection grid is at higher voltage.
- The three phase VSI filter size is small because of the MF in the collection grid.
- The overall system significantly reduces the amount of material in the cables and transformer in the collection system.
- The MF transformer can be packaged alongside the inverters in an extender box. This configuration eliminates not only the bulky line frequency transformer but also reduces site preparation (elimination of concrete pads / access rods) and allows more room for PV arrays.

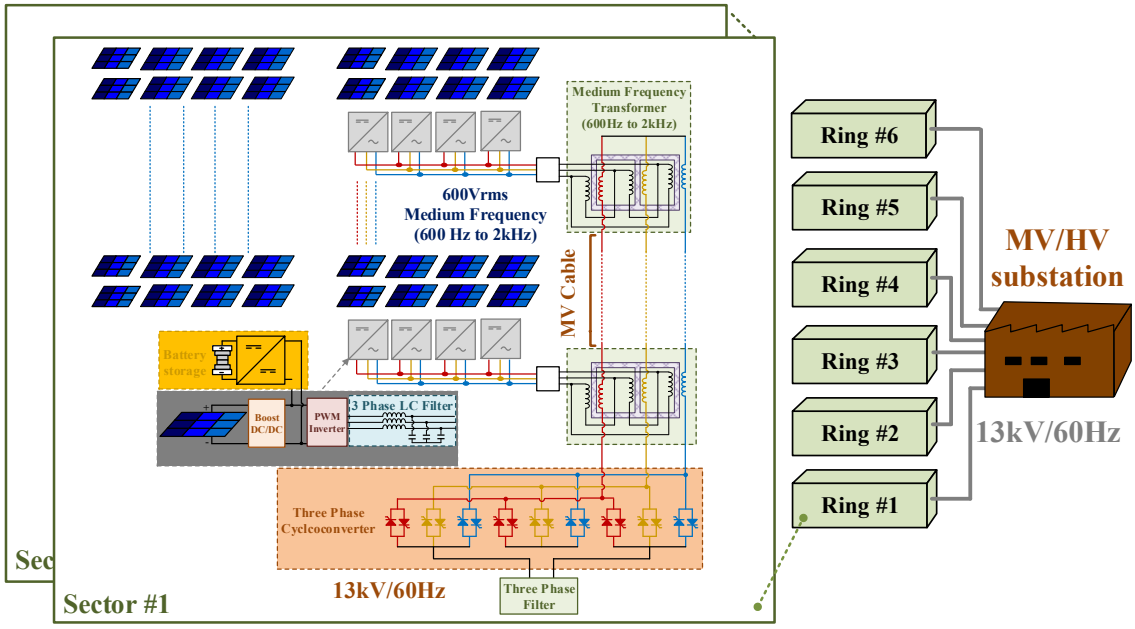

Figure 2–8. Proposed PV farm architecture

2.3.1. Analysis of the Proposed System

The Proposed MV-MF PV collection grid is shown in Figure 2–8. It comprises four main components:

1. Three phase inverter
2. MF transformer
3. MF cables and
4. Three phase cyclo-converter.

Each of these components are discussed in details below

2.3.1.1. Three Phase Inverter

A three phase VSI converts the regulated PV string output voltage to MF voltage. The three phase inverter is connected to the grid using three phase LC filter that is used

to filter out the inverter harmonics as in Figure 2–9. The filter parameters can be calculated using (2-1) and (2-2)[42]. It can be seen that when the frequency increases, both the filter inductance and capacitance decrease. Equation (2-3) and (2-4) are used to calculate the inverter conduction and switching losses respectively based on SiC MOSFETS [43].

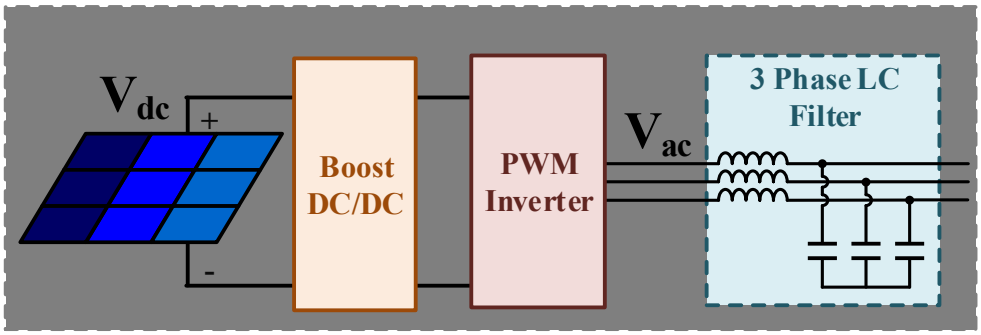

Figure 2–9. Typical three phase inverter with filter

$$L_{filter} = \frac{V_{dc}}{8 * \Delta I_L * f_s} \tag{2-1}$$

$$C_{filter} = \frac{P_{rated}}{3 * \omega_g * V_g^2} \tag{2-2}$$

Where V_{dc} is the rated dc link voltage, ΔI_L is the allowed current ripple, f_s is the inverter switching frequency, P_{rated} is the processed power through the filter, ω_g is the medium frequency grid voltage and V_g is the medium frequency grid line voltage.

$$P_{conduction} = I_{on}^2 * R_{dsOn} * \frac{V_{out}}{V_{dc}} \tag{2-3}$$

$$P_{switching} = \left(\frac{V_{dc} * I_{on} * \left(t_{on} + t_{off}\right)}{2} + C_{oss} * V_{dc}^2 \right) F_s \tag{2-4}$$

Where I_{on} is rms current through MOSFET, R_{dsOn} is the MOSFET turn on resistance,

V_{out} is the output rms voltage, t_{on}, t_{off} are the MOSFET turn on and turn off time and C_{oss} is the MOSFET output capacitance.

The summery for each three phase inverter is in Table 2-2 and the filter I_{out}/V_{out} transfer function is shown in Figure 2–10. It can be seen that the filter crosses the 0dB line as almost 1 kHz and introduces a resonance at 10 kHz. If needed, the resonance can be damped by passive, active techniques or hybrid that combines both of them.

TABLE 2-2.THREE PHASE INVERTER/FILTER PARAMETERS

Parameter	**3-Phase VSI**
Rated Power	15kW
On State RMS Current	14A
Output Voltage	600V
Selected Device	Cree C2M0080120D [44]
Switching Frequency	20kHz
Grid Frequency	1kHz
L_{filter}	900μH
C_{filter}	0.3μF
Overall Efficiency	99.1%

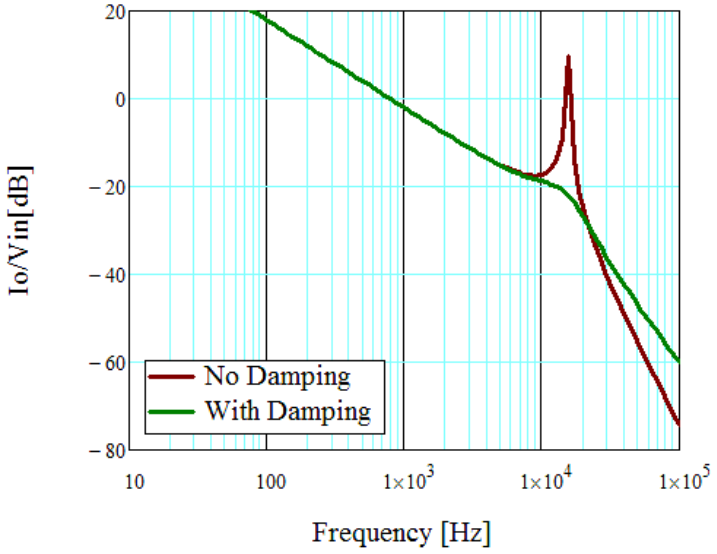

Figure 2–10. VSI Filter transfer function

2.3.1.2. Transformer

The medium frequency transformer will be distributed over the PV farm as shown in Figure 2–8. Its primary side winding are connected in delta to trap the third harmonics and its secondary side windings will have its six terminals exposed to allow for series connecting the output. This will allow cascading the transformer output to construct the MV for the collection grid.

$$B_o = \frac{[h_c k_a \Delta T]^{\frac{2}{3}}}{2^{\frac{2}{3}}[\rho_w k_w k_u]^{\frac{1}{12}}[k_c K_c f^{\alpha}]^{\frac{7}{12}}}\left[\frac{K_v f k_f k_u}{\sum VA}\right]^{\frac{1}{6}} \tag{2-5}$$

$$A_p = \left[\frac{\sqrt{2}\sum VA}{K_v f B_o k_f K_t \sqrt{k_u \Delta T}}\right]^{\frac{8}{7}} \tag{2-6}$$

$$J_o = K_t \sqrt{\frac{\Delta T}{2k_u}} \frac{1}{\sqrt[8]{A_p}} \tag{2-7}$$

The transformer specifications are in Table 2-3. Two design approaches are adopted for transformer designing and the design steps for both approaches are in the flowcharts in Figure 2–11 and Figure 2–12.

$$A_{p1} = \left[\frac{\sqrt{2}\ \sum VA}{K_v f B_o k_f K_t \sqrt{k_u \Delta T}} \right]^{\frac{8}{7}} \tag{2-8}$$

$$A_{pi+1} = A_{pi} - \frac{a_0 A_{pi}^2 - a_1 A_{pi}^{\frac{7}{4}} + a_2}{2a_0 A_{pi} - \frac{7}{4} a_1 A_{pi}^{\frac{3}{4}}} \tag{2-9}$$

$$J_o = \sqrt{\frac{h_c k_a \sqrt{A_p} \Delta T - V_c K_c f^{\alpha} B_{max}^{\beta}}{\rho_w V_w k_u}} \tag{2-10}$$

$$N = \frac{V_{rms}}{K_v f B_{max} A_m} \tag{2-11}$$

TABLE 2-3. PV FARM TRANSFORMER SPECIFICATIONS

Input voltage	600 V
Output voltage	2.2 kV
Rated power	150 kW
Connection	Delta/Star

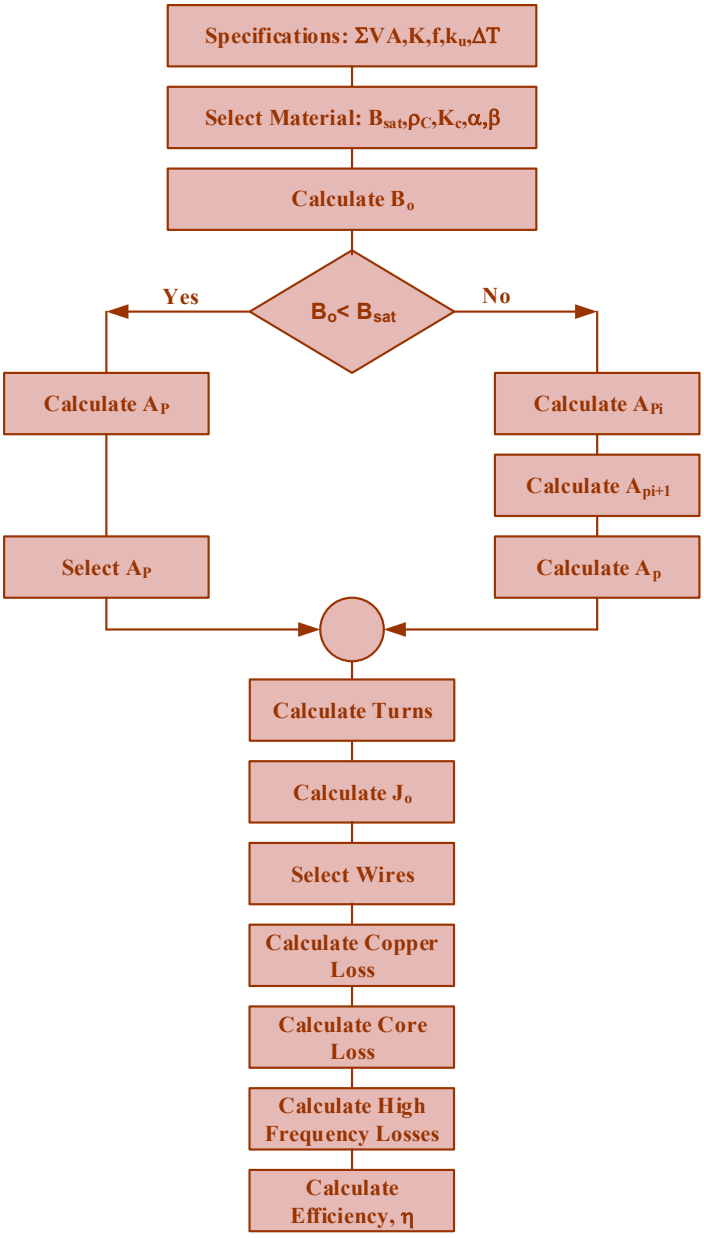

Figure 2–11. Max efficiency flow chart [17]

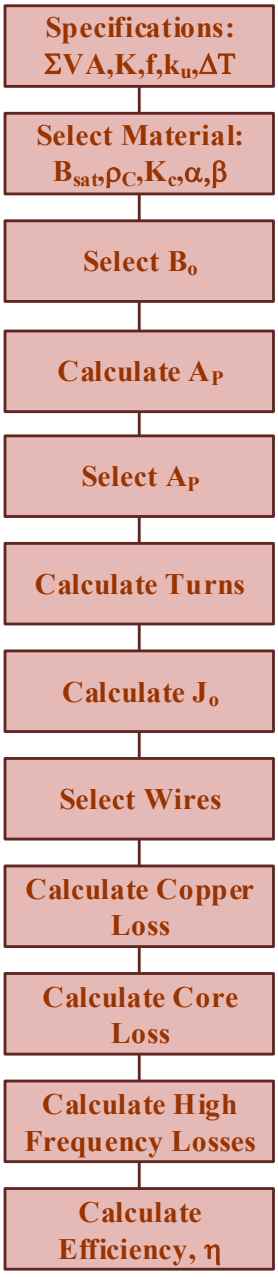

Figure 2–12. Min size flow chart [17]

The maximum efficiency approach, Figure 2–11, is adopted when the efficiency is the top priority in the design criteria. The transformer's operating flux density is determined by (2-5) when the core losses equal the winding losses; the area product is

calculated using (2-6) and the current density are calculated using (2-7). If the calculated flux density is higher than B_{max} then the transformer can't operate at that point, then the operating flux value is set to a value that is lower than the maximum flux density value, here it is set to be $85\% * B_{max}$, then (2-9) and (2-10) is used to calculate the new transformer area product and current density respectively. Modifying the initial area product that is calculated as in (2-8) is essential to avoid overdesigning the transformer core[17].

A summery for different transformer designs are shown in Figure 2–13-Figure 2–16 considering different materials and a frequency range that starts from 60Hz to 2000Hz. It can be noted that the flux utilization decreases when the frequency increases (Figure 2–13). This resulted from the fact that the losses has to be minimum so reducing the transformer's operating flux is the possible way to decrease the transformer core losses to maintain a minimum losses (i.e. high efficiency). Another observation is that at low frequency, the optimum flux value is always higher than the maximum allowed by the materials, so that the preset value is always used and the resultant efficiency is always lower than the other cases as in Figure 2–15 but overall the efficiency is expected to be over 99%. As expected for the same power and frequency, the nano-crcytaline transformer will be the smallest in size and the amorphous cores came after it as in Figure 2–14 but with the frequency increase the size difference is not high due to the fact that the flux need to be optimized to maintain low operating losses.

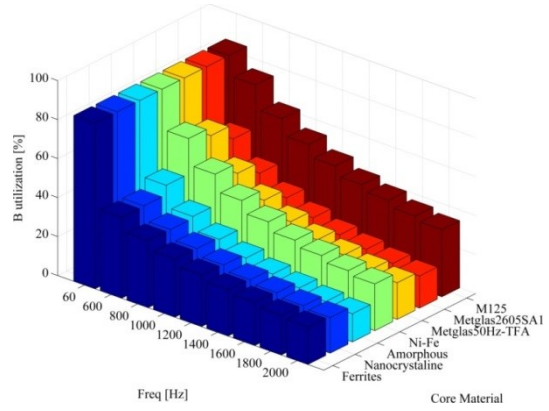

Figure 2–13. Max efficiency transformer flux utilization ratio

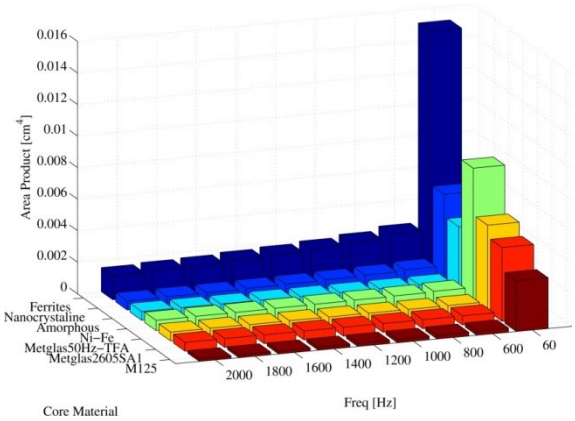

Figure 2–14. Max efficiency transformer area product

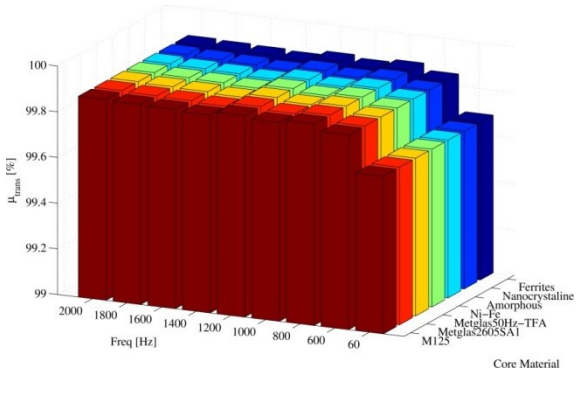

Figure 2–15. Max efficiency transformer parameters expected efficiency

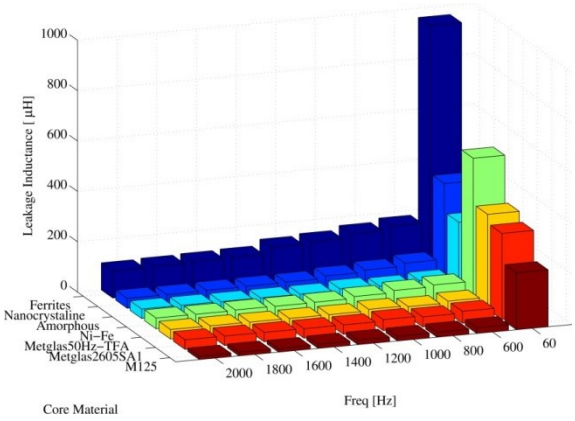

Figure 2–16. Max efficiency transformer leakage inductance

On the other hand; the min size approach (Figure 2–12), is adopted when the transformer size if the top priority. The operating flux density is chosen to be 95% of the maximum value. The area product and the current density are calculated using (2-9) and (2-10) to avoid transformer over design.

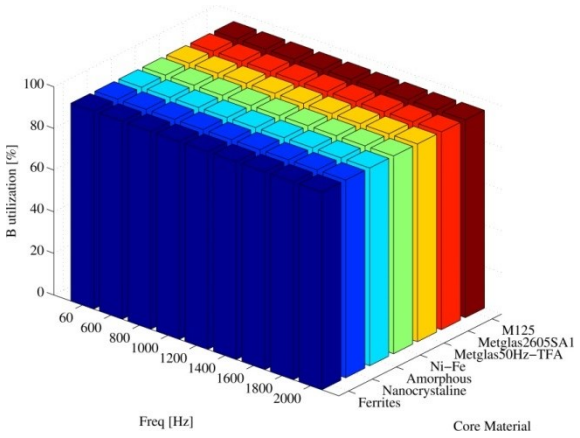

Figure 2–17. Min size transformer flux utilization ratio

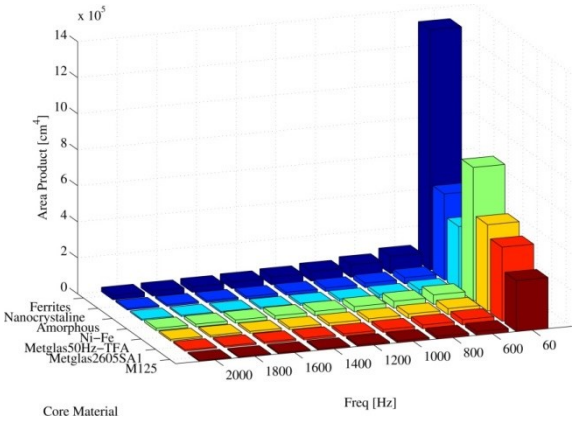

Figure 2–18. Min size transformer parameters area product

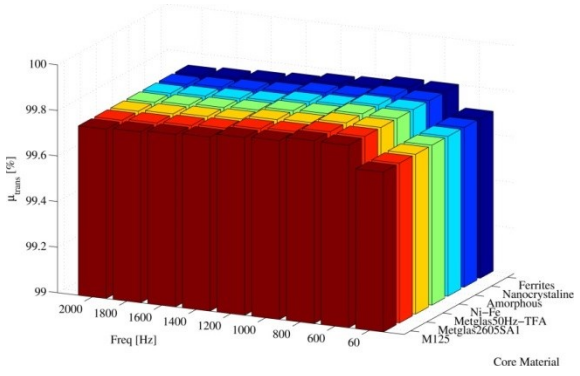

Figure 2–19. Min size transformer parameters expected efficiency

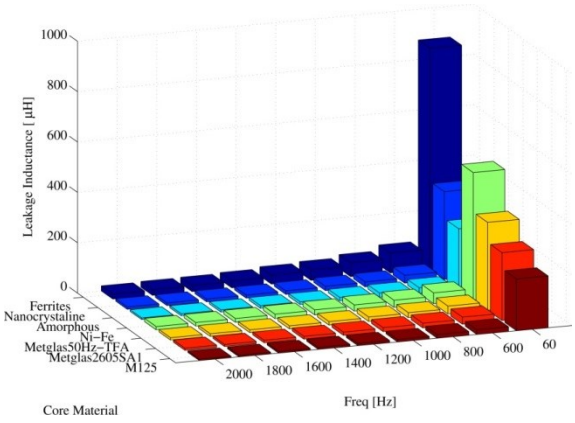

Figure 2–20. Min size transformer leakage inductance

Figure 2–17 - Figure 2–20 show a summery for the transformer design cases that were done using minimum size approach. The transformer area product, window area * core cross section area, is lower than the former case and tradeoff is the resultant efficiency which is lower than the maximum efficiency approach Figure 2–17. However, in both cases the expected transformer efficiency is above 99 % (Figure 2–19) and the

transformer size is shown to be smaller than the 60Hz counterpart Figure 2–18. This will result in a low cost compact transformer design and where it can be packaged alongside the inverters in an extender box. This configuration reduces site preparation (elimination of concrete pads / access rods) and allows more room for PV arrays.

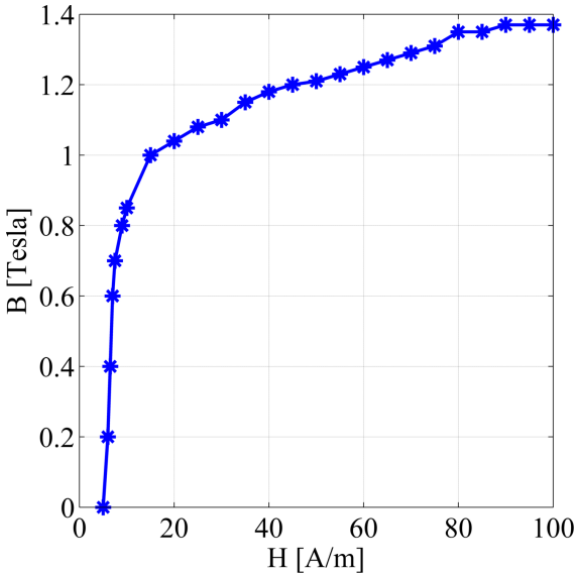

Figure 2–21. Metglass2605SA1 BH curve[45]

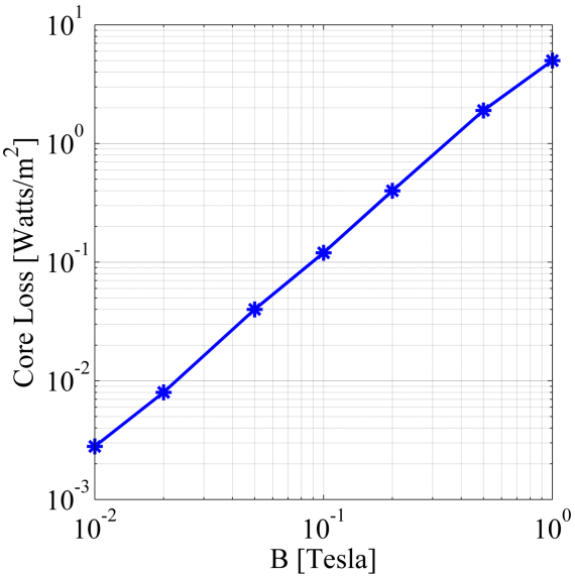

Figure 2–22. Metglass2605SA1 Core Loss at 1kHz[45]

A 1 kHz transformer of Metglass2605SA1 max efficiency is selected and verified in ANSYS Maxwell. The Metglass2605SA1 properties are shown in Figure 2–21 and Figure 2–22. The transformer 3D model is in Figure 2–23, the core is in blue, the primary and secondary winding are in orange and green respectively. An exponentially sinusoidal input voltage is applied on the transformer terminals to avoid the inrush current effects. The transformer is loaded with its rated load.

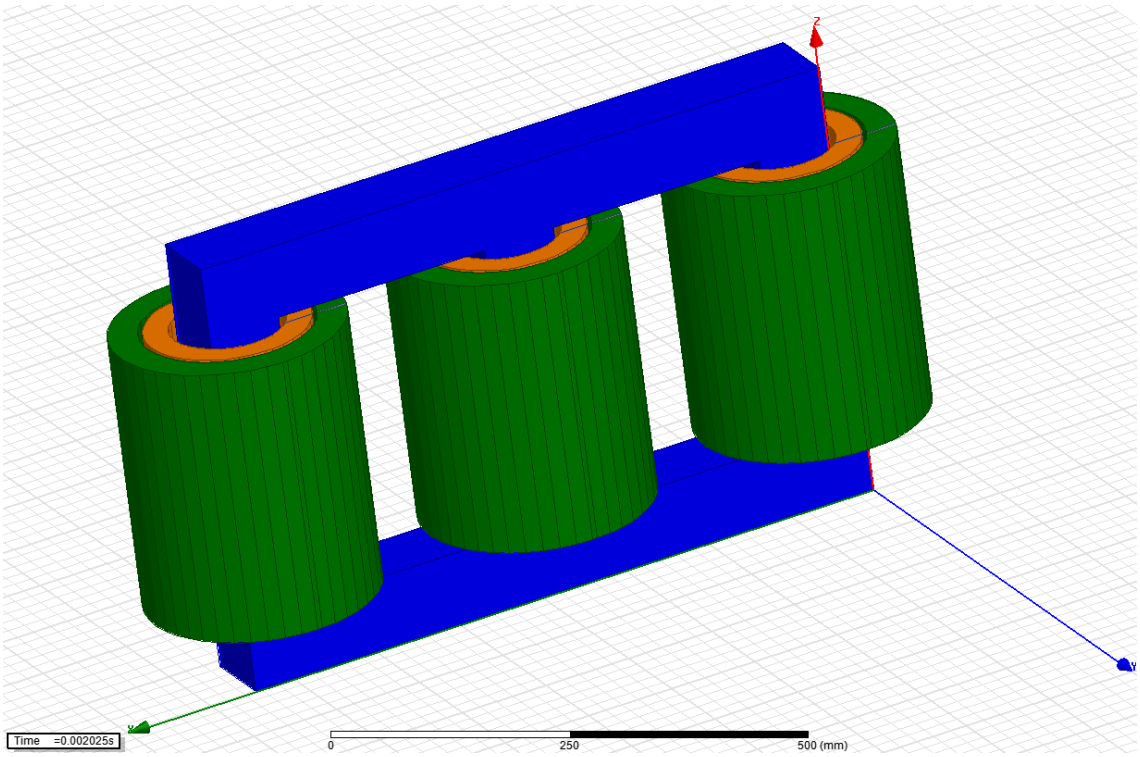

Figure 2–23. Transformer FEA 3D model in ANSYS Comsol

The transformer primary voltage and current are shown in Figure 2–24(a) and (b) respectively, the transformer secondary voltage and current are shown in Figure 2–24(c) and (d) respectively. The core losses are shown in Figure 2–25 and the average value is found to be 116W. This will result in a transformer efficiency of 99.923% as expected. The transformer's flux distribution is shown in Figure 2–26; the average value is 0.67T which is 45% of the maximum allowed flux value as expected from the design (Figure 2–16-upper right).

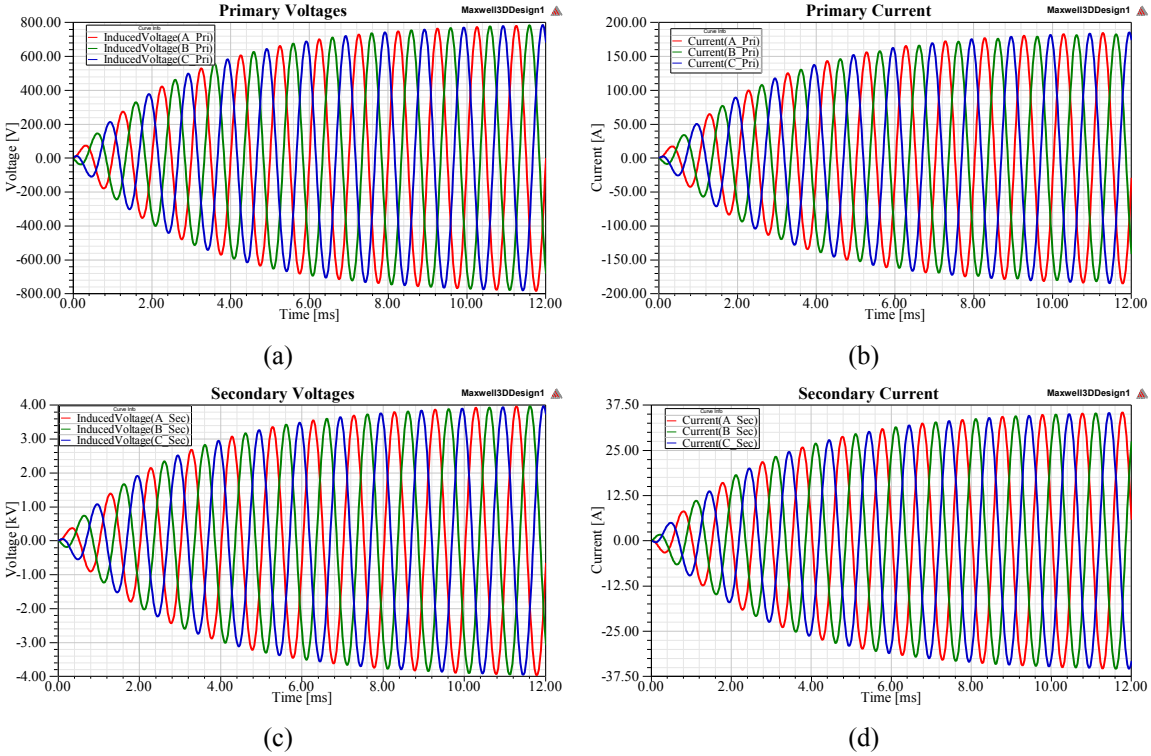

Figure 2–24. Transformer time domain (a) primary voltage(b)primary current (c)secondary voltage(d)secondary current as generated by ANSYS Comsol FEA simulation

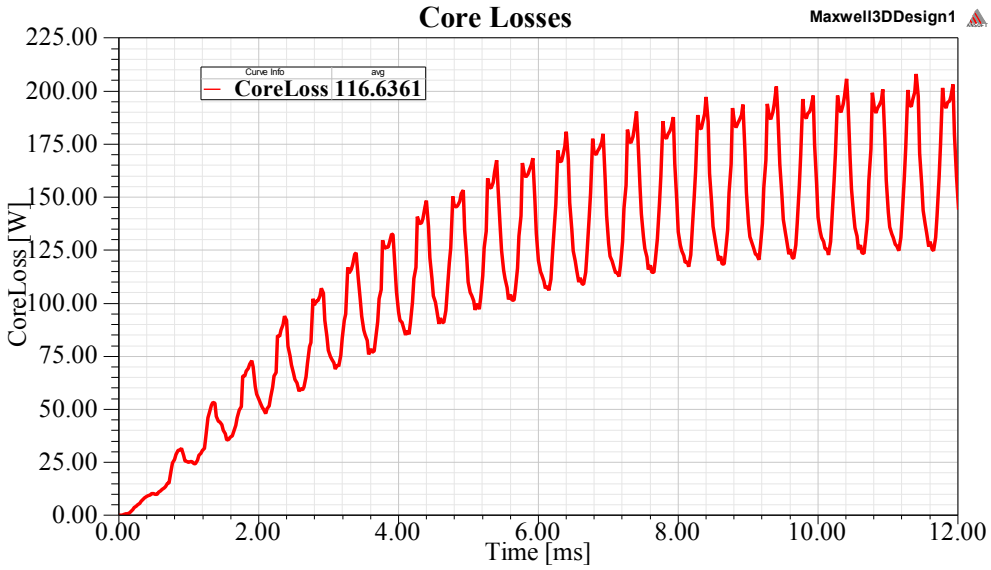

Figure 2–25. Transformer core losses as generated by ANSYS Comsol FEA simulation

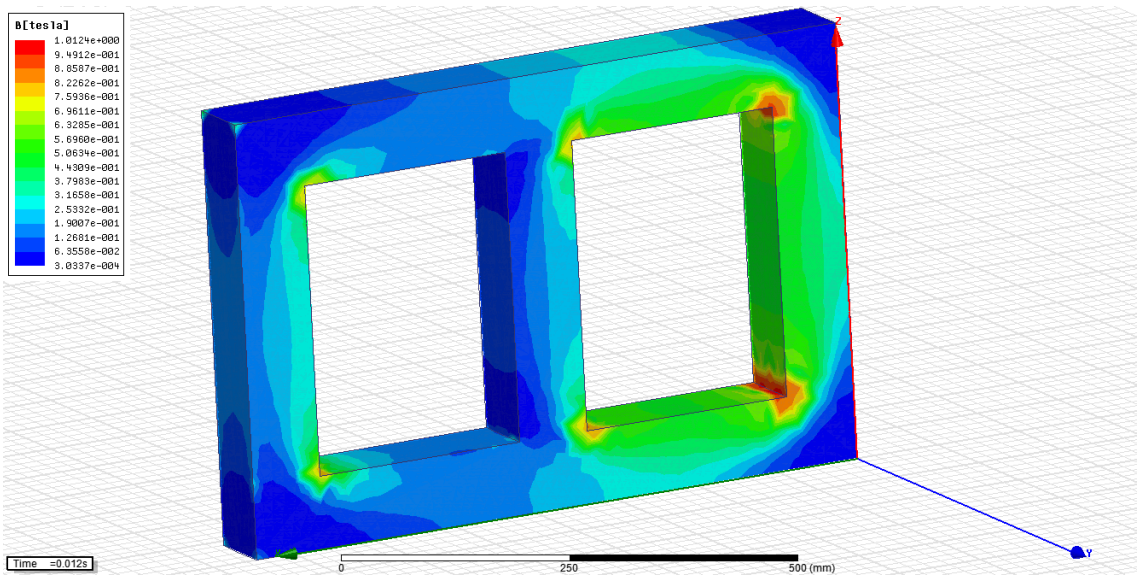

Figure 2–26. Transformer 3D flux distribution at time = 12ms as generated by ANSYS Comsol simulation

2.3.1.3. AC Cables

Cables connect the MF transformers terminals to construct the MV-MF collection grid. It is desirable to choose cables with low inductance to improve the transmission quality and low resistance to increase the transmission efficiency. To calculate the cable ac resistance at the medium frequency (2-12)–(2-16) will be used[46].

$$R_{ac} = R_{dc}\left(1 + Y_s + Y_p\right) \tag{2-12}$$

$$Y_s = \frac{x_s}{192 + 0.8x_x} \tag{2-13}$$

$$x_s = \left(\frac{8\pi f}{R_{dc}} k_s 10^{-7}\right)^2 \tag{2-14}$$

$$Y_p = \frac{x_p}{192 + 0.8x_p} {d_c}^2 \left(0.312{d_c}^2 + \frac{1.18}{0.27 + \frac{x_p}{192 + 0.8x_p}}\right) \tag{2-15}$$

$$x_p = \left(\frac{8\pi f}{R_{dc}} 10^{-7}\right)^2 \tag{2-16}$$

Where R_{ac} is the cable ac resistance per km, R_{dc} the cable dc resistance per km, Y_s is the skin effect factor and Y_p is the proximity effect factor, f is the cable operating frequency and d_c is the cable diameter and k_s is the cable layout factor.

The skin effect and proximity effect are included in these equations, they must be considered since the cable operating frequency is high. A summery for the cables used in the Eggebek PV farm is in Table 2-4, this will be used for comparison with proposed architecture. Figure 2–27 shows the location of the CB cable, i.e. the low voltage cable, and the MV cables, i.e. the cables within the sectors and the rings. The cable parameters are summarized in Table 2-5.

TABLE 2-4. EGGEBEK LAYOUT/CABLE SUMMARY

		CB	**Sector**	**Ring**
Rating	***Power***	90kW	2.29MW	16MW
	Voltage	480V	20kV	20kV
	Current	108A	66A	462A
	Frequency	60Hz	60Hz	60Hz
Cable	***Avg. Dis.***	0.096km	0.337km	0.843km
	Selected[47]	CPI-T104-U16	CX4-T103-U13	CX4-T103-U30
	Ω/km	0.628	0.668	0.08
	Losses	1.228kW	1.7kW	24.89kW
	Efficiency	98.65%	99.93%	99.84%
Efficiency Total		98.43%		

TABLE 2-5. PROPOSED EGGEBEK LAYOUT/CABLE SUMMARY

		CB	Sector	Ring
Rating	***Power***	150kW	1.5MW	13.5MW
	Voltage	480V	13kV	13kV
	Current	180A	67A	592A
	Frequency	60Hz	1000Hz	60Hz
Cable	***Avg. Dis.***	0.078km	0.349km	0.873km
	Selected[47]	CP1-T104-U16	CX3-T103-U12	CX3-T101-U60
	Ω/km	0.232	0.927	0.039
	Losses	1.015kW	2.488kW	20.73kW
	Efficiency	99.33%	99.83%	99.85%
Efficiency Total		99.01%		

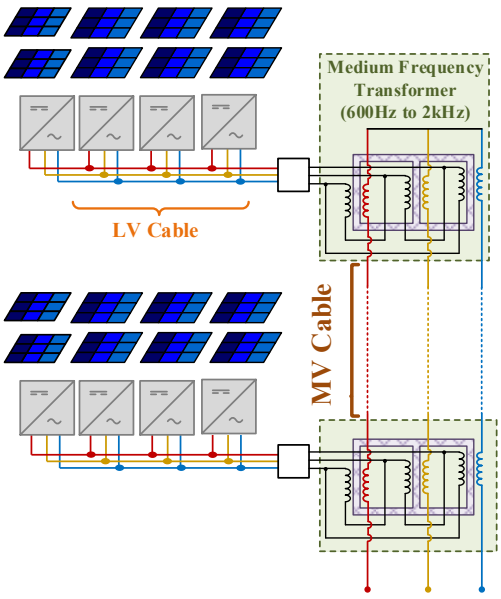

Figure 2–27. cables in the proposed medium frequency structure

To investigate the cable resonance frequency, the PI section modeling approach is adopted [46]. Equation 2-17 is used to determine the required number of PI section that is sufficient to fully model the cable within the frequency of interest. Figure 2–29 shows the low voltage cable input impedance, it can be seen that this section don't impose any resonance in the system. Figure 2–30 shows the medium voltage cable input impedance frequency response and it can be noted that the resonance took place around 100 kHz which is 5 times the inverter switching frequency and won't have any impact on the system.

$$N_{\pi} = \frac{8 * f_{max} * l}{v_e} \tag{2-17}$$

Where f_{max} is the maximum study frequency, l is the cable length, v_e is the propagation velocity

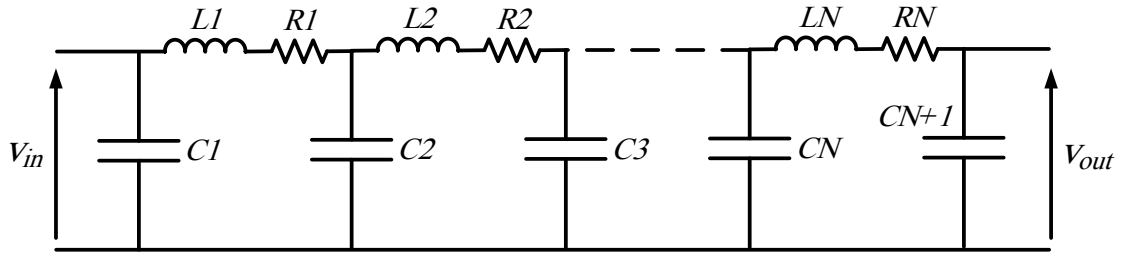

Figure 2–28. PI section modeling for power cable [46]

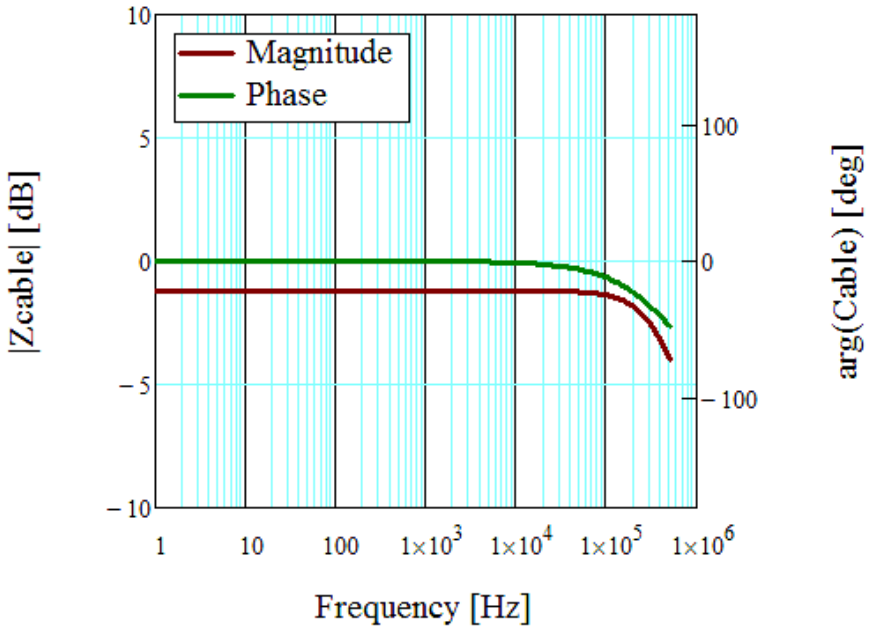

Figure 2–29. LV cable impedance frequency response

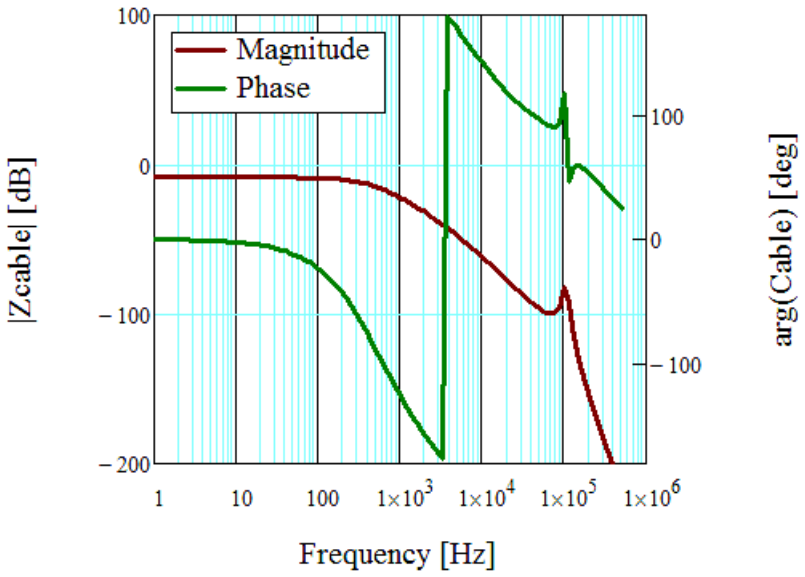

Figure 2–30. MV cable impedance frequency response

2.3.1.4. Cycloconverter

The MV-MF voltage is converted to low frequency voltage using a three phase to three phase cycloconverter as shown in Figure 2–31. A Thyristor based AC-AC matrix converter is used due to the familiarity with the device operation and its ability to be stacked in series to withstand higher voltage levels. The wideband gap based Thyristor can also be used to get higher AC-AC conversion efficiency. The Thyristor conduction and switching losses can be found using (2-18) and (2-19) respectively [48]. The cycloconverter switched in either load commutation mode or forced commutation mode [49, 50]. The load commutation based switching in [49] will encounter smaller switching losses when compared to the forced commutation switching in [50], however, the later will have the advantage of controlled power factor operation but the former is limited by leading power factor operation. The forced commutation switching scheme in [50] is implemented in this work.

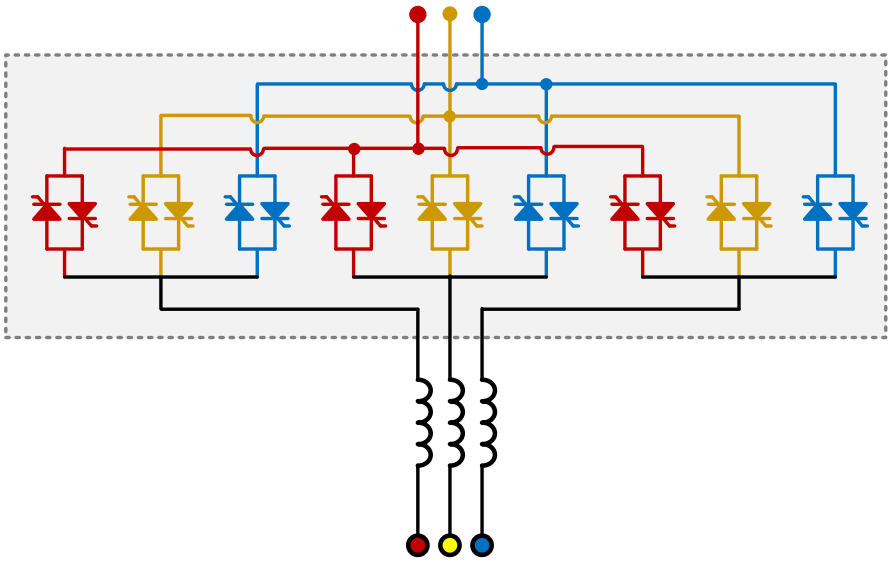

Figure 2–31. Three phase to three phase cycloconverter structure

$$P_{conduction} = V_{frd} I_{av} + R_{on} I_{rms}^2 \quad (2\text{-}18)$$

$$P_{switching} = Q_{rr} V_{rev} 0.5 F_s \quad (2\text{-}19)$$

2.3.2. Control of the Proposed System

One sector block diagram is shown in Figure 2–32. Equations (2-20)-(2-23) show the system constraints. The current in all transformers outputs must be equal because the transformers primary windings' are series connected (2-20). The MF voltage is the sum of all the transformers output (2-21) and the total power injected to the grid is the power available by each inverter set minus the system losses (2-22). The fourth constrain is imposed by the cycloconverter, the MF voltage must be greater than the grid voltage by $\sqrt{3}$ (2-23).

$$I_1 = \cdots I_n = I = I_{MF} \quad (2\text{-}20)$$

$$\sum_{i=1}^{n} V_i = V_{MF} \quad (2\text{-}21)$$

$$\sum_{i=1}^{n} P_i = P_g - P_{loss} \quad (2\text{-}22)$$

$$V_{MF} = \sqrt{3} V_g \quad (2\text{-}23)$$

$$V_{InvOutMin} = \frac{V_{CylcoMin}}{n_{Inv} * N_{trans}} = \frac{\sqrt{3} * V_g}{n_{Inv} * N_{trans}} \quad (2\text{-}24)$$

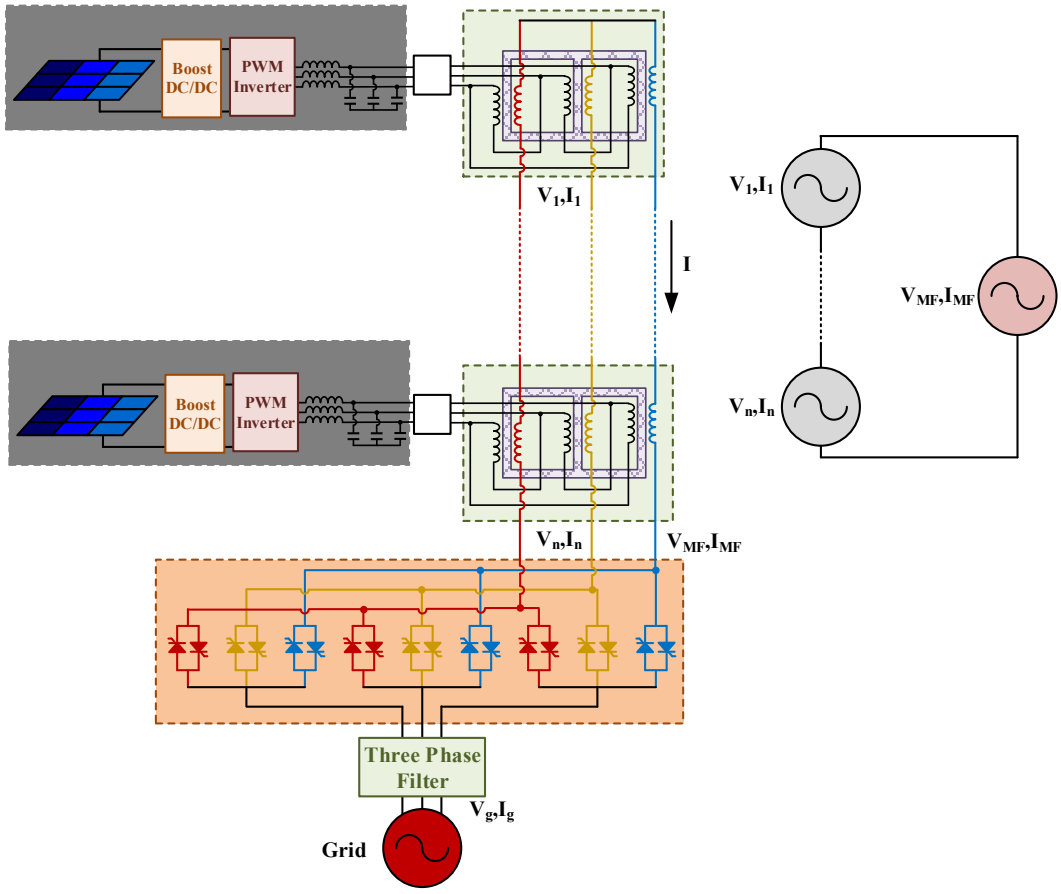

Figure 2–32. Block diagram for PV farm sector arrangement

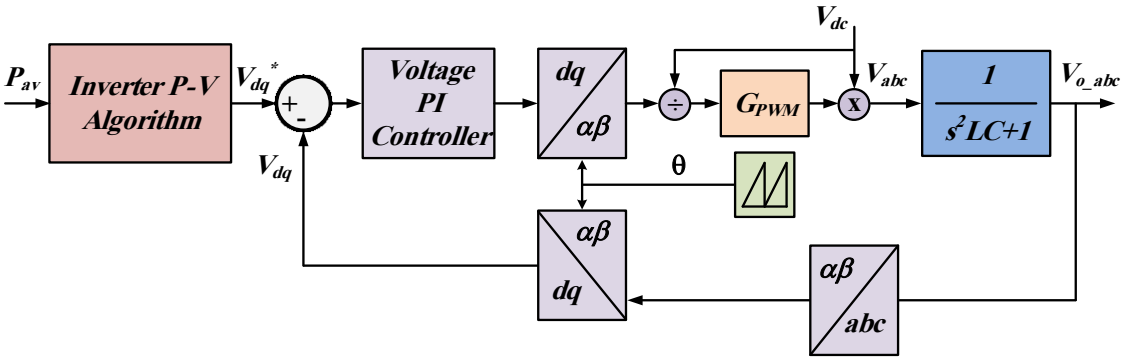

Figure 2–33. Block diagram for the PV inverter voltage controller

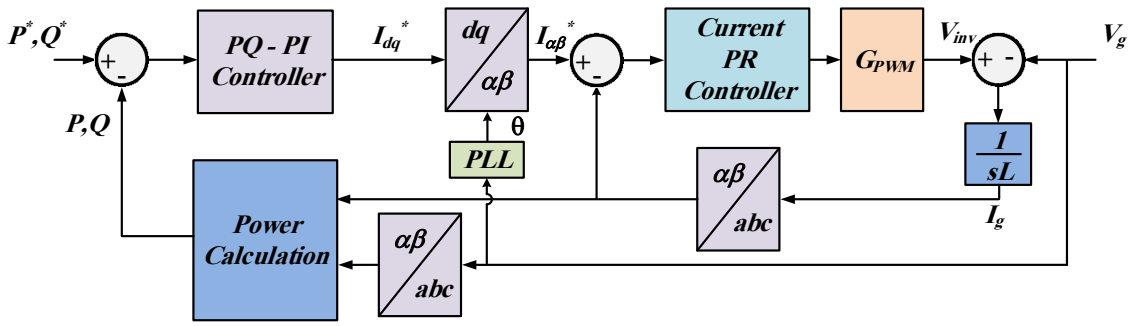

Figure 2–34. Block diagram for the cycloconverter controller

The controller strategy for each sector has two parts. The first is the PV inverter controller (Figure 2–33) and the second is the cycloconverter controller (Figure 2–34). The inverters will be responsible for the collection grid voltage while the cycloconverter is responsible for the collection grid current. It is assumed that all the inverters and the cycloconverter are sharing a communication channel.

The PV inverter is chosen to be closed loop voltage controller implemented in dq frame(Synchronous frame) and it should be heavily relying on its integral part, this controller should not have a fast sudden changes to ensure the stability of the system [51]. The controller commanded voltage is calculated using the inverter PV algorithm that its flow chart is shown in Figure 2–35, the first step for the algorithm is to determine the maximum available power at the inverter and send it to the cycloconverter controller. In case of faulty condition and the fault in the inverter feeder, the inverter will command zero voltage. The inverter will command voltage either in normal operation or if it is not the faulty one. A Droop like controller will determine the output voltage of the inverter. If the available power at the inverter is higher than 85% of the nominal power then the

applied voltage will be directly proportional with available power. If the available power is lower than the 85% of the nominal power, then the converter voltage is inversely proportional to the available power. The maximum voltage output is limited by the converter maximum overvoltage limit which can be 10%. The 85% limit of power is calculated from the minimum voltage limit that is imposed by the cycloconverter operation (2-23), number of inverters and transformer turns ratio. This control strategy allows for maximum power tracking and maintains the voltage in the required level for valid operation and is simple.

The cycloconverter controller will act as a power load (i.e. closed loop power) and its controller block diagram is shown in Figure 2–34.The commanded power to the controller is calculated by the algorithm shown in Figure 2–36. The first step for the algorithm is to sum all the available inverter powers from all the sector inverters, then after subtracting the system losses, the resultant power is injected to the grid at unity power factor. This will ensure that the commanded current is always within the capability of each inverter and the inverter voltage controller will ensure that each inverter is operating at maximum efficiency and maintaining its voltage limit. The inner controller current loop is implemented in the stationary reference frame using proportional resonant controller[51]. The command for this controller is the active and reactive power errors that are calculated using the commanded instantaneous counter parts that can be calculated using (2-25) and (2-26)[52].

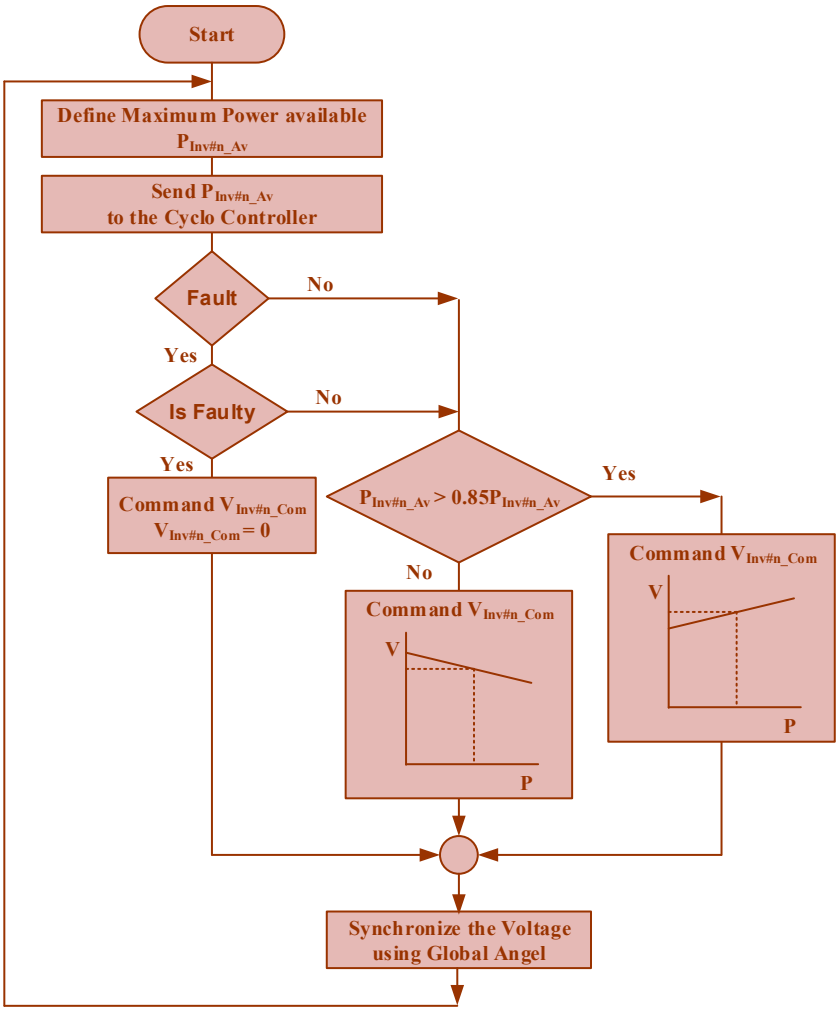

Figure 2–35. Flow chart for the inverter PV algorithm

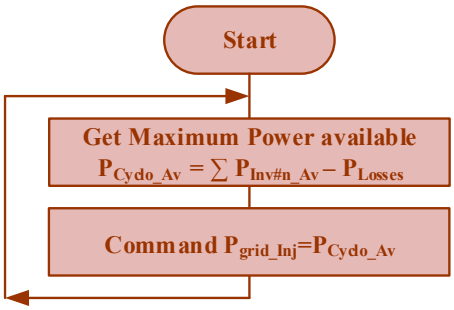

Figure 2–36. Flow chart for the cycloconverter controller

$$p = v_\alpha i_\alpha + v_\beta i_\beta \tag{2-25}$$

$$q = v_\beta i_\alpha - v_\alpha i_\beta \tag{2-26}$$

Where p is the active power and q is the reactive power, v and i are the voltage and current respectively, and α and β are the stationary components of the voltage and current ins the stationary reference frame

2.3.3.Simulation of the Proposed System

PLECS is used to simulate the system and validate the proposed structure and its controller. Three inverters/transformer cells were used along with the cycloconverter and grid as in Figure 2–37. Each cell can process 150kW of power with a total power processed of 450kW at normal loading conditions.

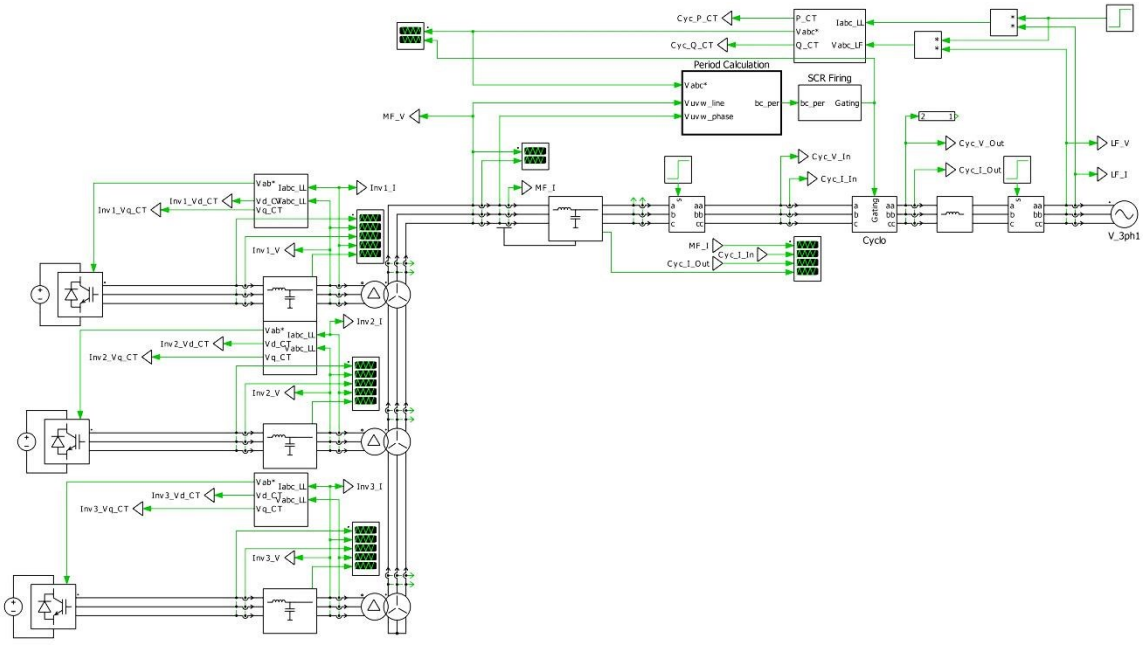

Figure 2–37. The system simulation in PLECS

2.3.3.1. Different Insulation Levels

Different insulation levels are simulated to examine the controller dynamic performance; the insulation level (that is reflected on the PV inverter voltage) is changed by quarter of its value and the voltage commands are change accordingly. The moments of insulation level change are indicated by gray lines in the below time domain figures and they are summarized in Table 2-6.

TABLE 2-6. COLLECTION GRID SIMULATION TIME INSTANT INSULATION LEVEL CHANGE SUMMARY

Time[sec] / Power [PU]	0	1/60	5/60	9/60	13/60	17/60
Inverter 1	1	1	0.5	0.5	0.75	1
Inverter 2	1	1	0.5	0.25	1	1
Inverter 3	1	1	1	0.5	0.25	1
Cycloconverter	0	3	2	1.25	2	3

Figure 2–38 shows the PV inverters closed loop voltage command tracking response, it can be seen the all the inverter has a stable fast response. The inverters' voltage and currents are shown in Figure 2–39, Figure 2–40 respectively. It can be noticed that each PV inverter voltage can be controller individually based on the available power level while all the inverters are sharing the same current since the transformer output terminals are series connected. Figure 2–41 shows the collection grid voltage and current, it can be seen that both of them are changing with the different insulation level, however, the voltage levels are changing more clearly. The

cycloconverter commanded active and reactive powers are changing with the different insulation level and the cycloconverter closed loop command tracking operation is shown in Figure 2–42. The cycloconverter input current and voltage are both changing with the different insulation level since it is acting a power load.

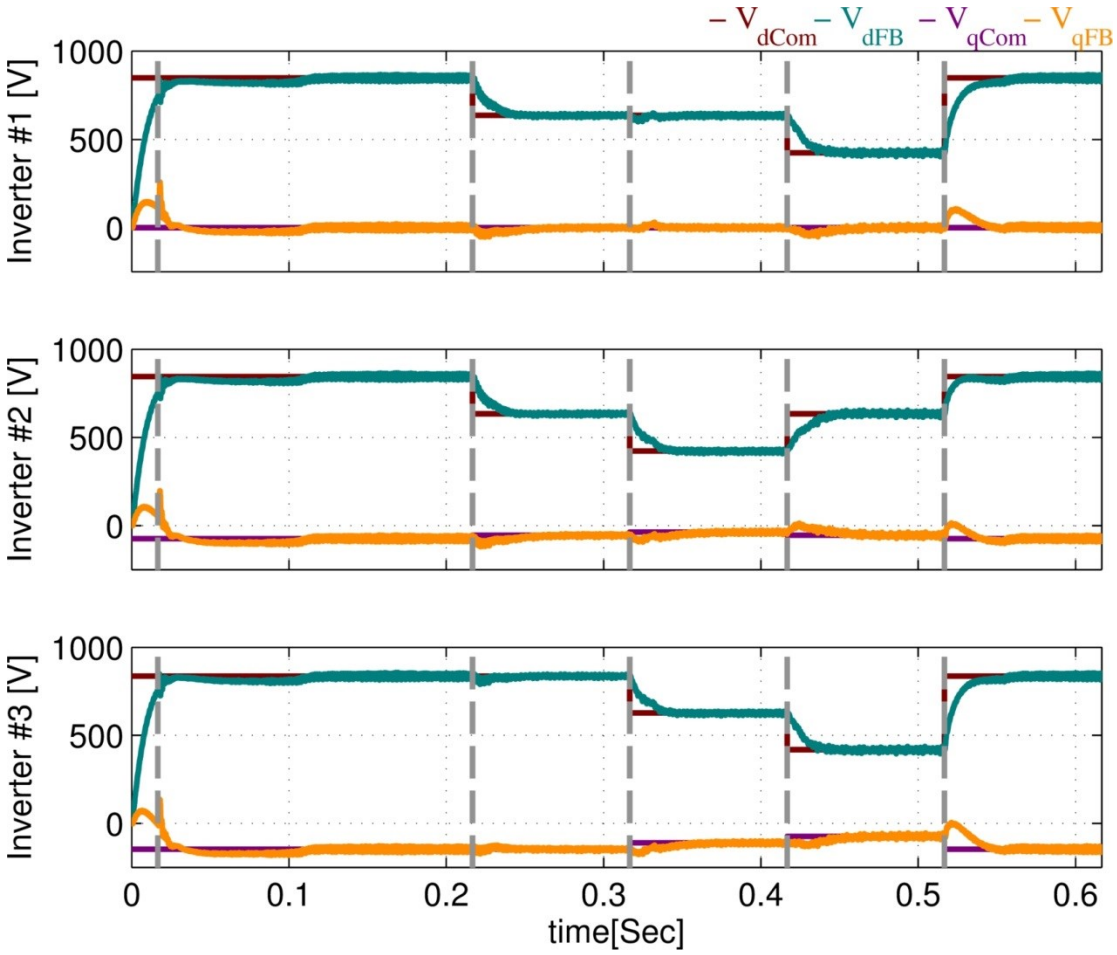

Figure 2–38. PV inverters synchronous reference frame voltage closed loop time domain command tracking response for different power levels

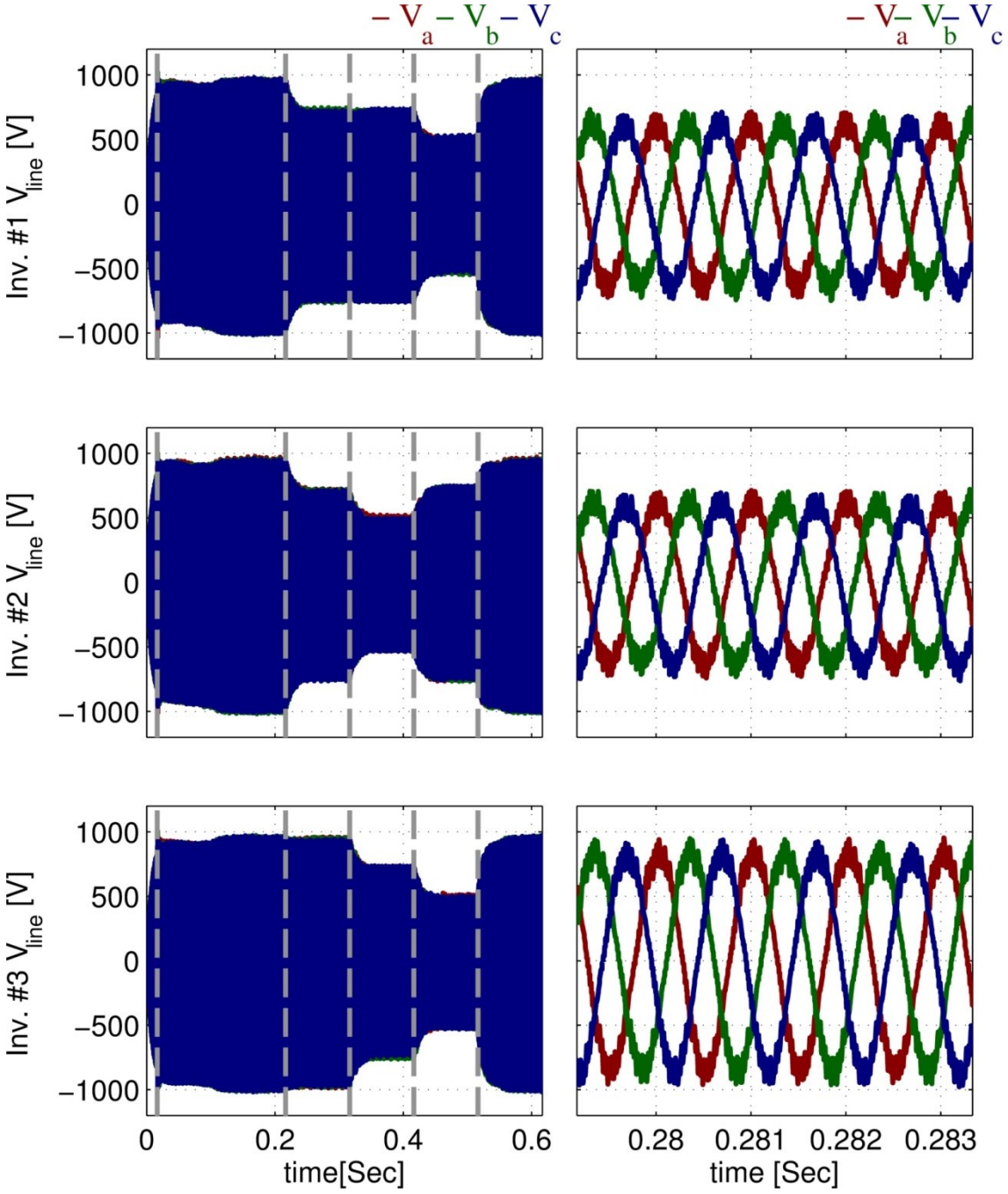

Figure 2–39. PV inverter line voltage time domain waveforms during different loading conditions (right) zoomed out view (left) zoomed in view

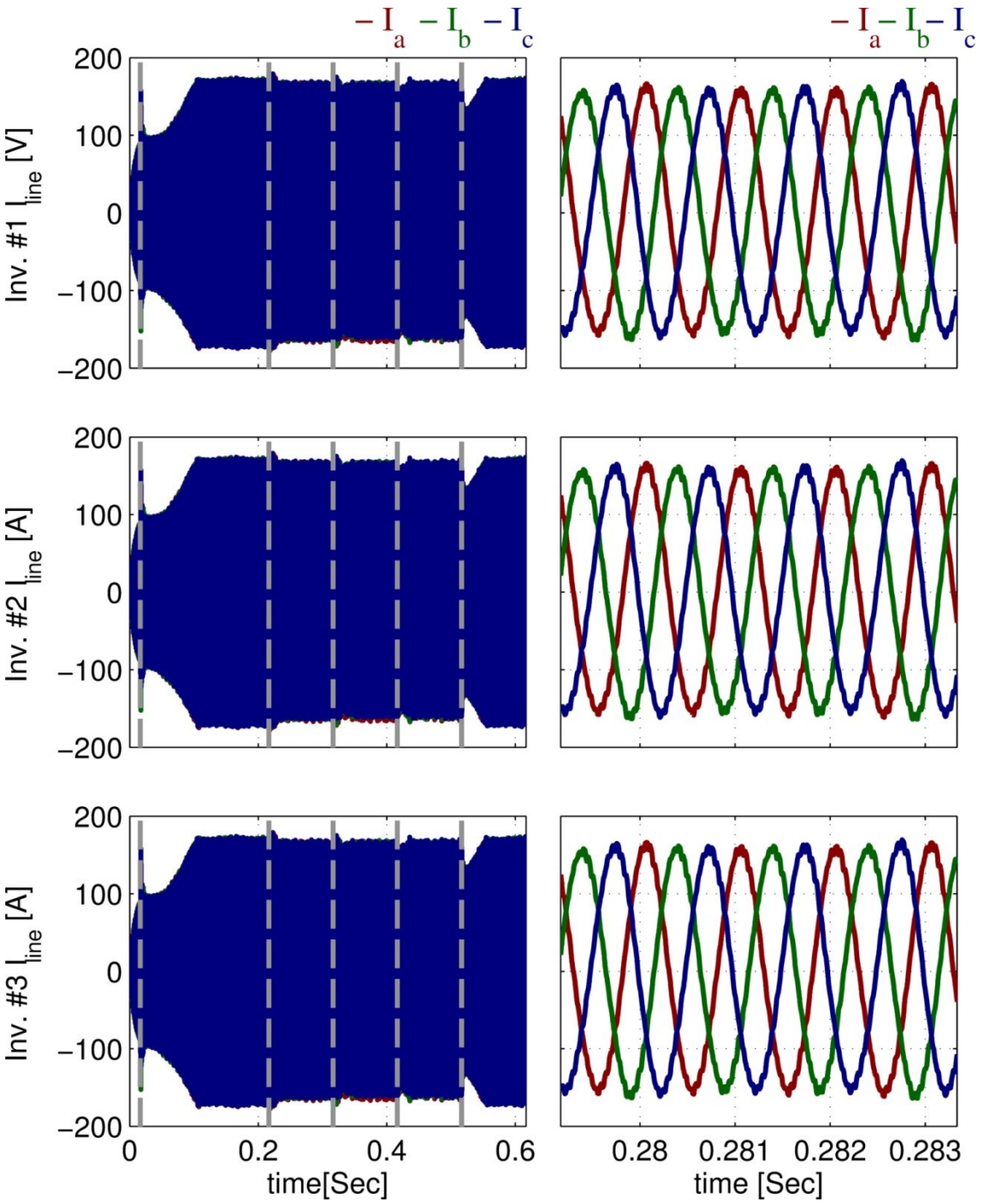

Figure 2–40. PV inverter line current time domain waveforms during different loading conditions (right) zoomed out view (left) zoomed in view

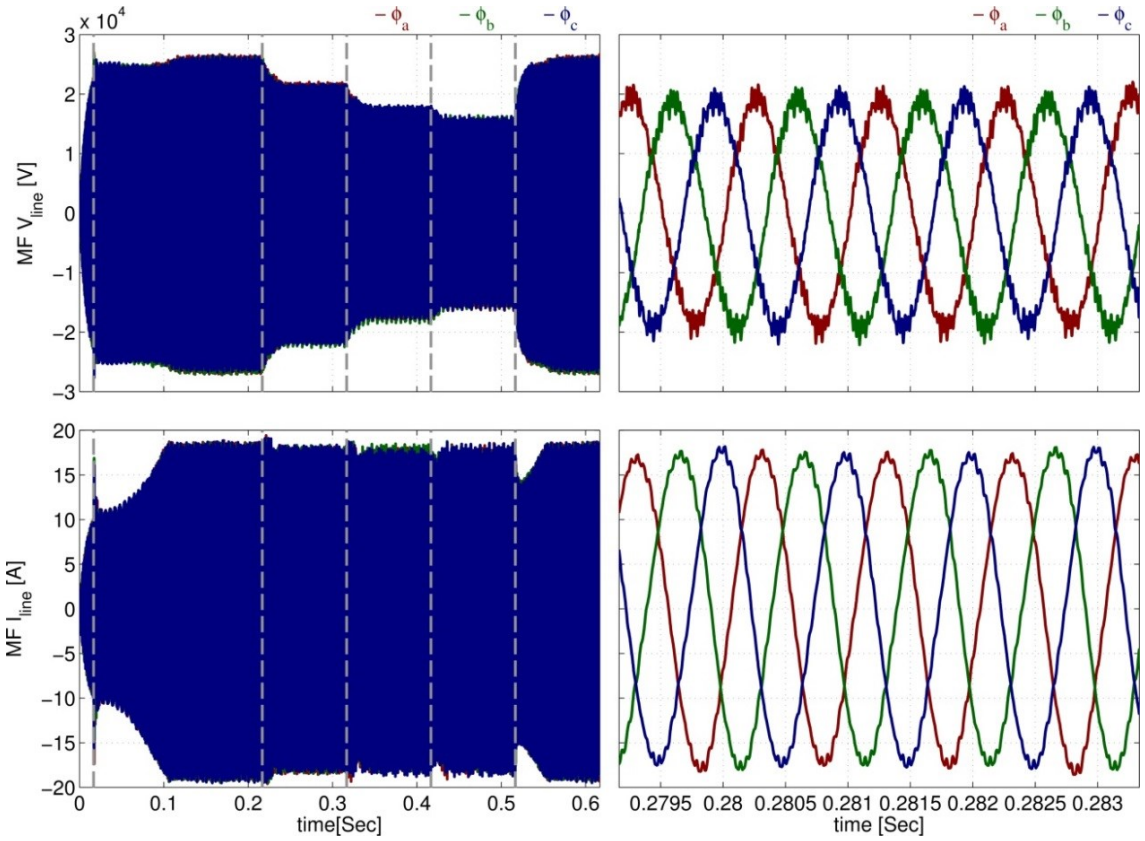

Figure 2–41. medium frequency network time domain waveforms voltage and current during different loading conditions (right) zoomed out view (left) zoomed in view

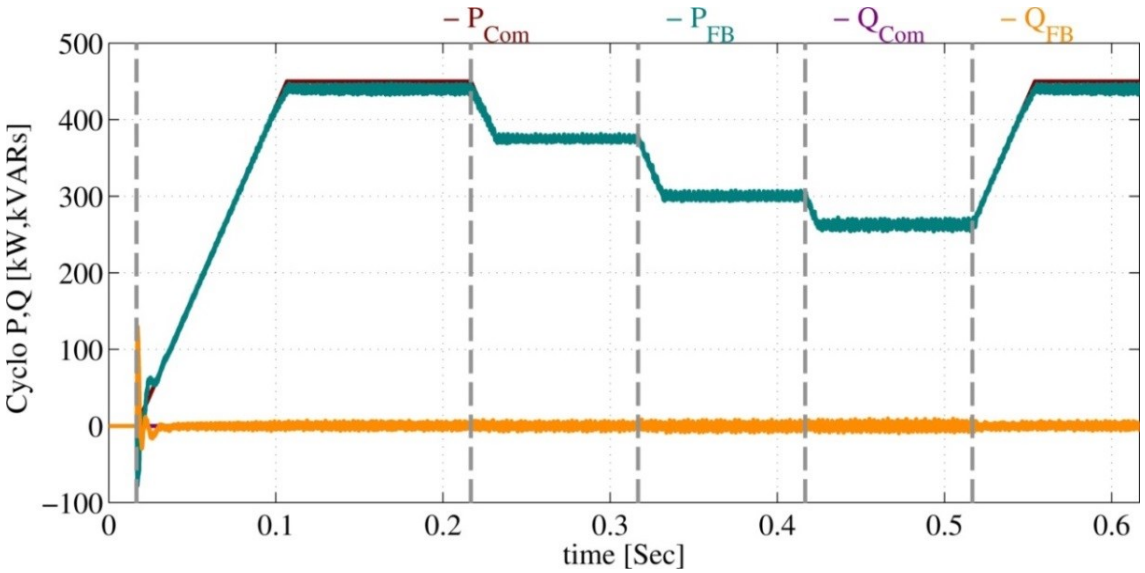

Figure 2–42. Cycloconverter active and reactive power closed loop time domain command tracking time domain response for different insulation levels

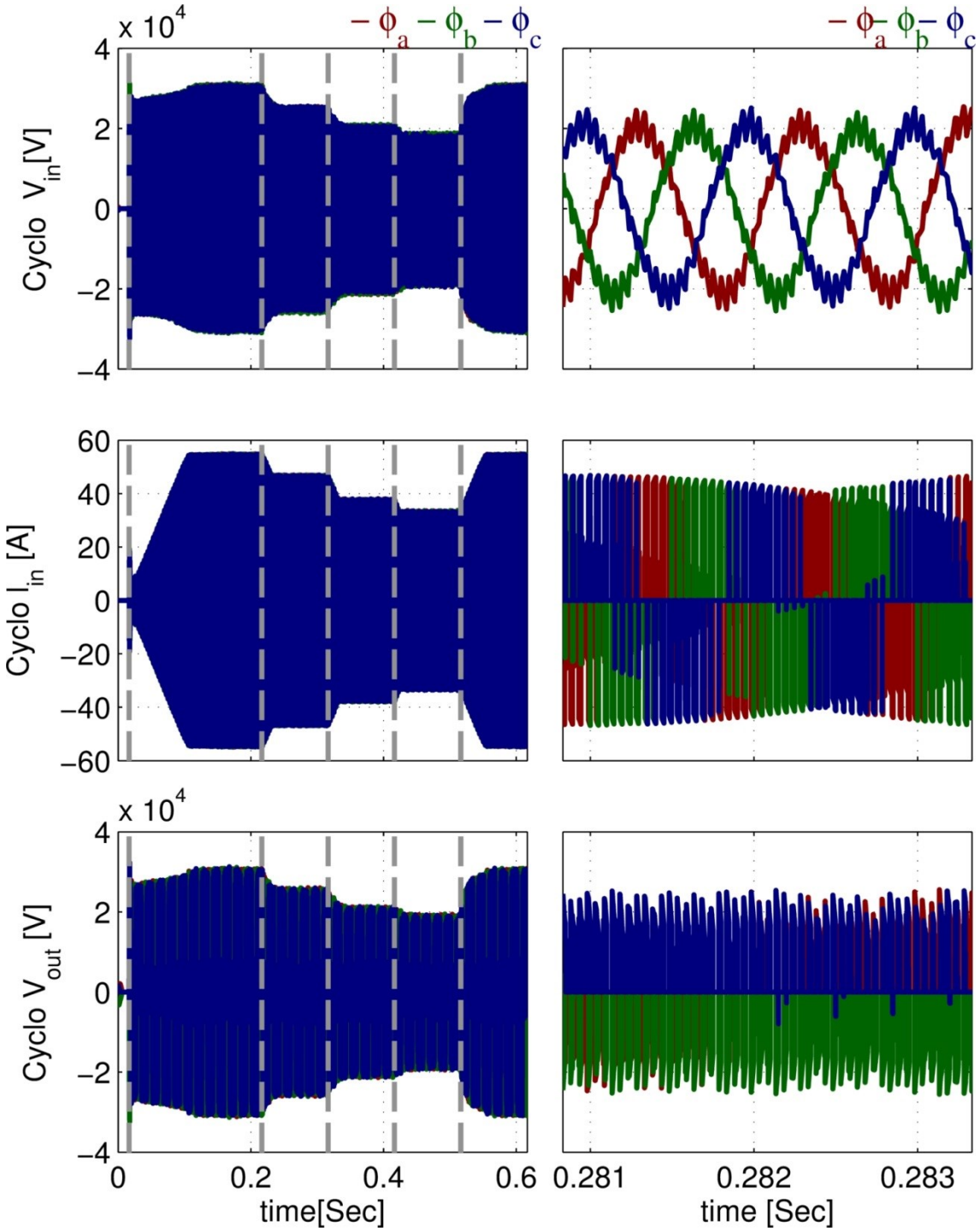

Figure 2–43. Cycloconverter time domain input voltage, input current and output switching voltage (right) zoomed out view (left) zoomed in view

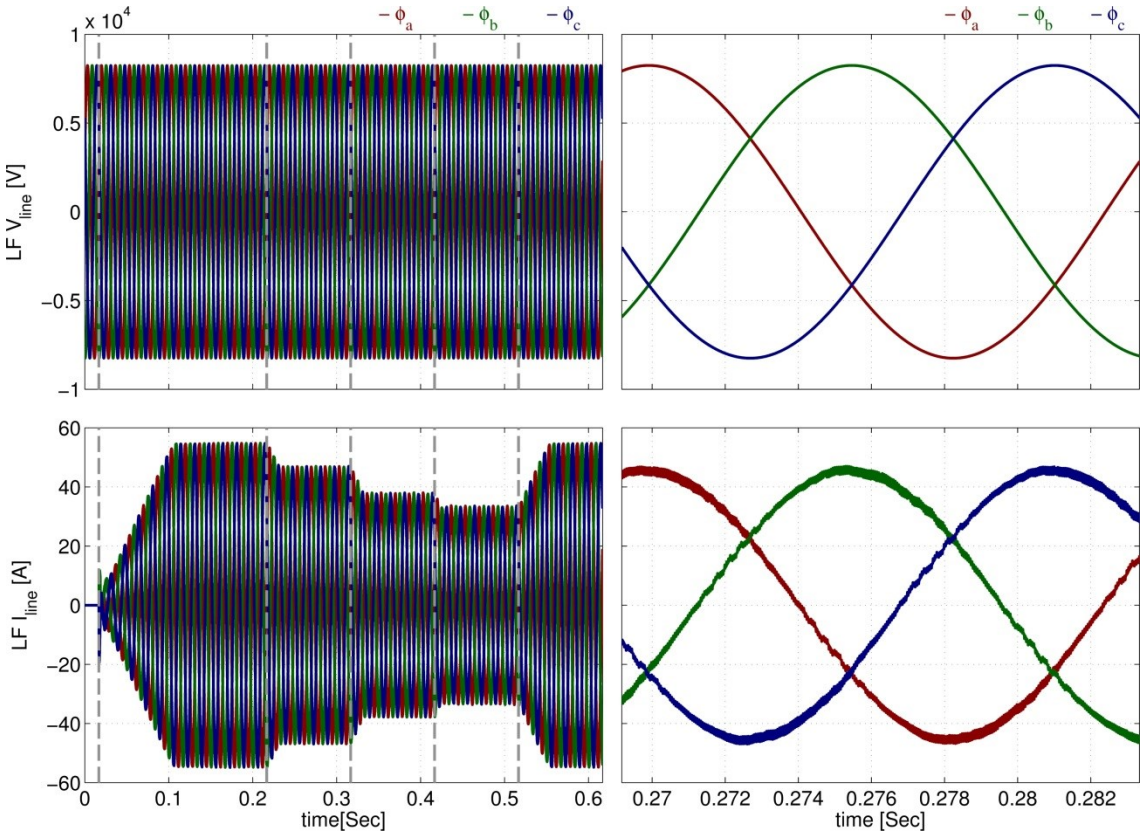

Figure 2–44. Time domain grid voltage and grid injected current during different loading conditions (right) zoomed out view (left) zoomed in view

The cycloconverter input voltage, input current and output switched voltage are shown in Figure 2–43 and the utility grid voltage and injected current are shown in Figure 2–44. The injected current is changing based on the available power and the zoomed view for the grid voltage and injected current proofs that success of the cycloconverter controller to operate at unity power factor.

2.3.3.2. Fault Condition

Figure 2–45 shows the same system but in faulty condition where the third inverter will be switched out. It is assumed that the other two inverters could generate an extra voltage of 0.5PU to support the grid voltage after the outage of the faulty inverter.

This assumption is valid only in this simulation case because the target is to test the controller robustness, however, in the real condition; there will be seven inverters, so if one goes out, the rest should provide an extra 1/6 PU voltage.

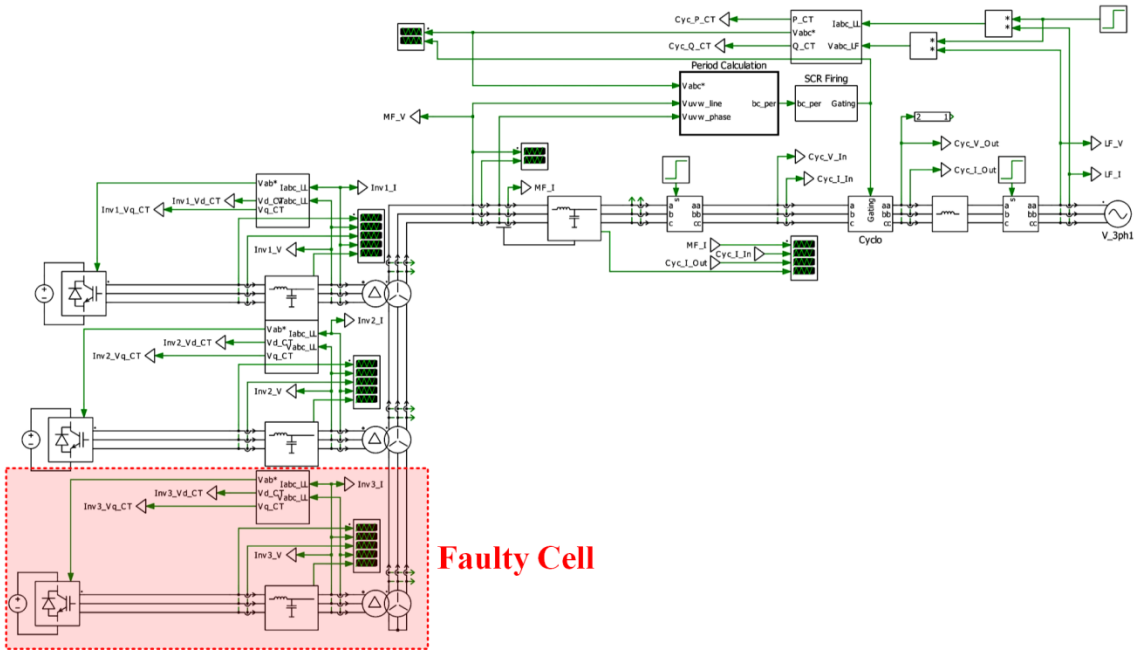

Figure 2–45. System simulation block diagram in PLECS at faulty condition

The voltage closed loop command tracking for the three inverters is shown in Figure 2–46 and as can be seen that the system controller will withstand the fault status and increase the two inverter voltages to maintain the MF collection grid voltage and sustain the collection grid operation. The inverters voltage and currents are shown in Figure 2–47 and Figure 2–48 respectively. It should be noted that the total voltage stays the same however; due to the power decrease the collection grid (i.e. medium frequency) current decreased (Figure 2–49) and the two inverter currents followed this command while they are having the same current value.

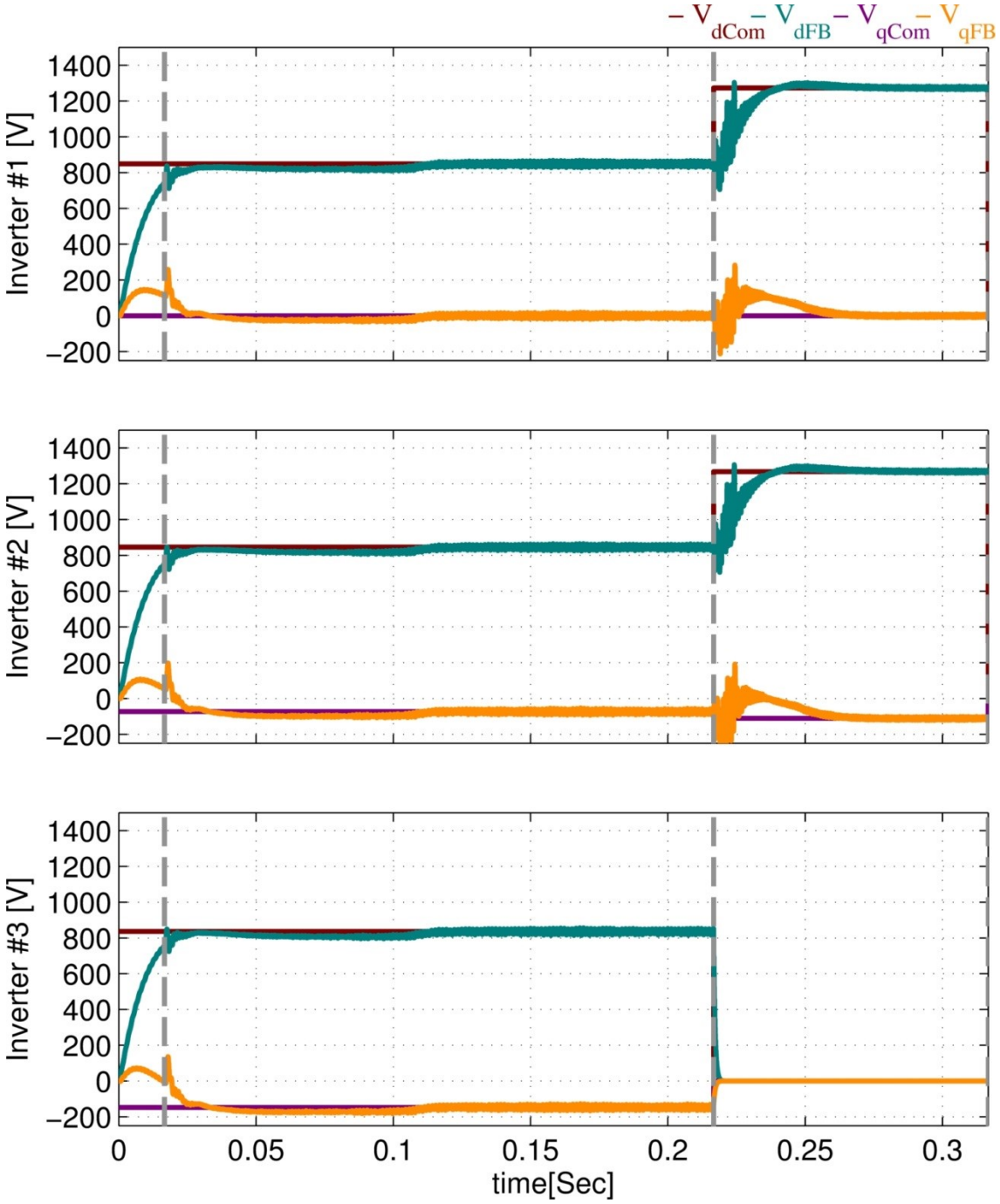

Figure 2–46. PV inverters synchronous reference frame voltage closed loop time domain command tracking response during normal and faulty condition

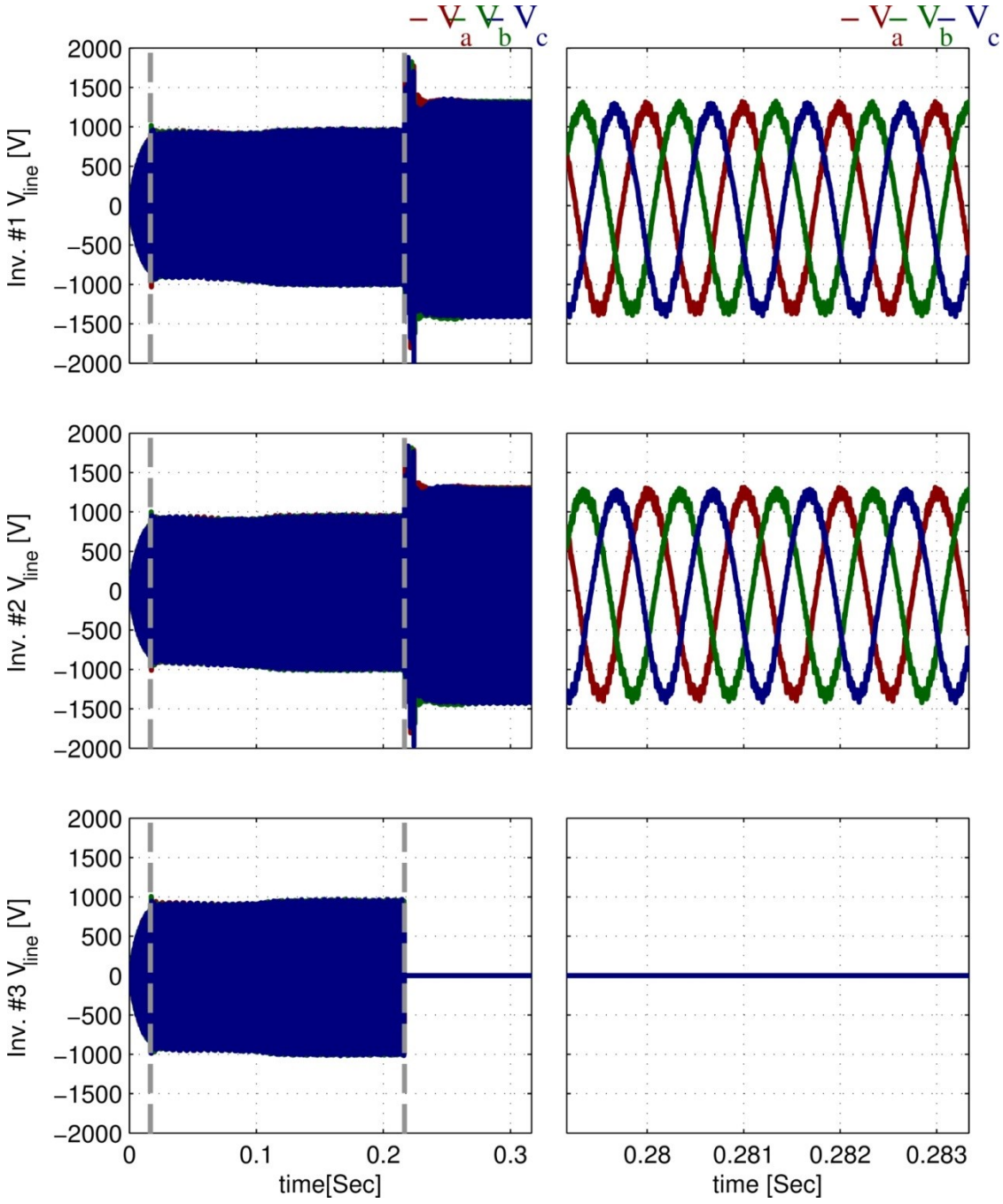

Figure 2–47. PV inverter line voltage time domain waveforms during normal and faulty condition (right) zoomed out view (left) zoomed in view

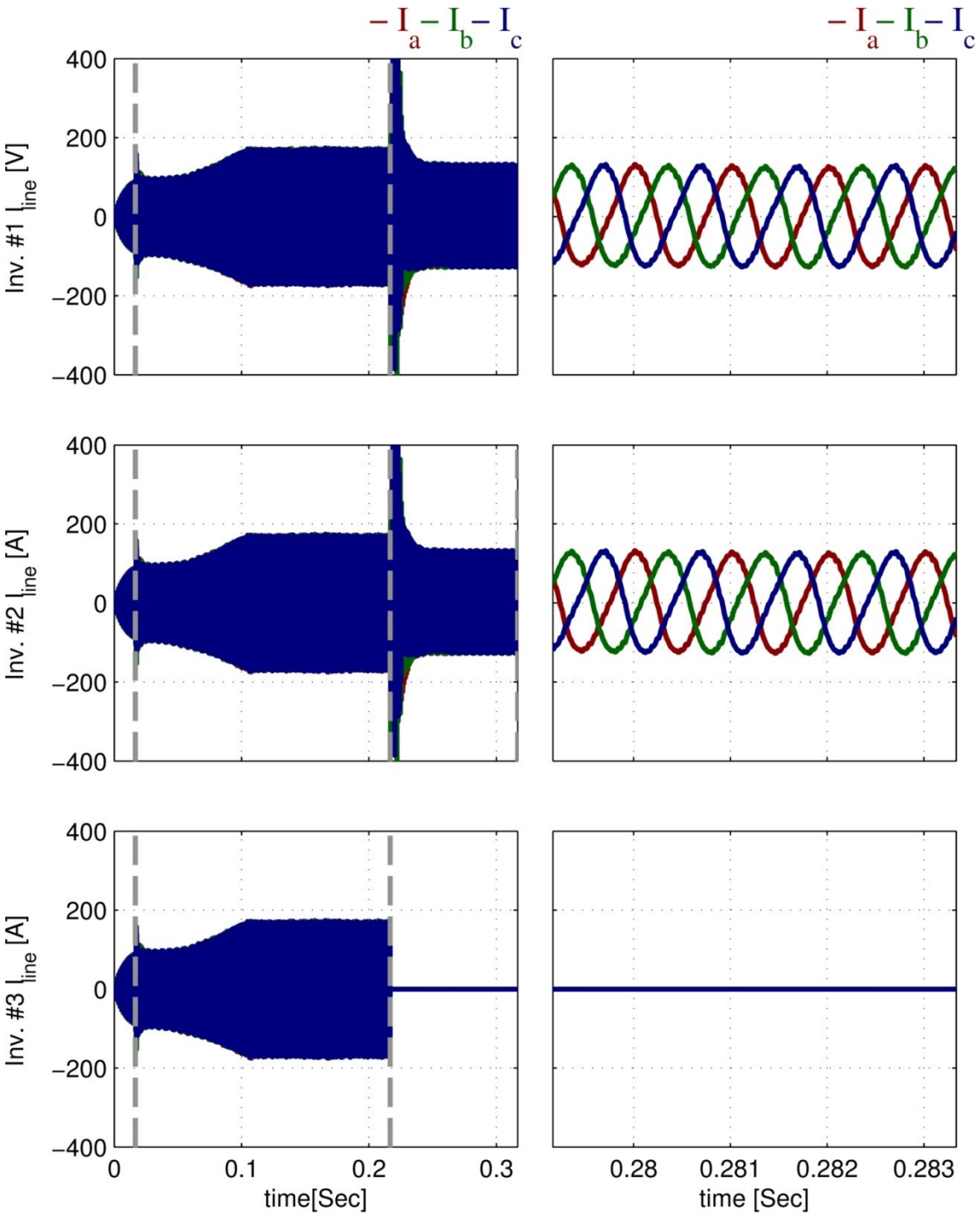

Figure 2–48. PV inverter line current time domain waveforms during normal and faulty condition (right) zoomed out view (left) zoomed in view

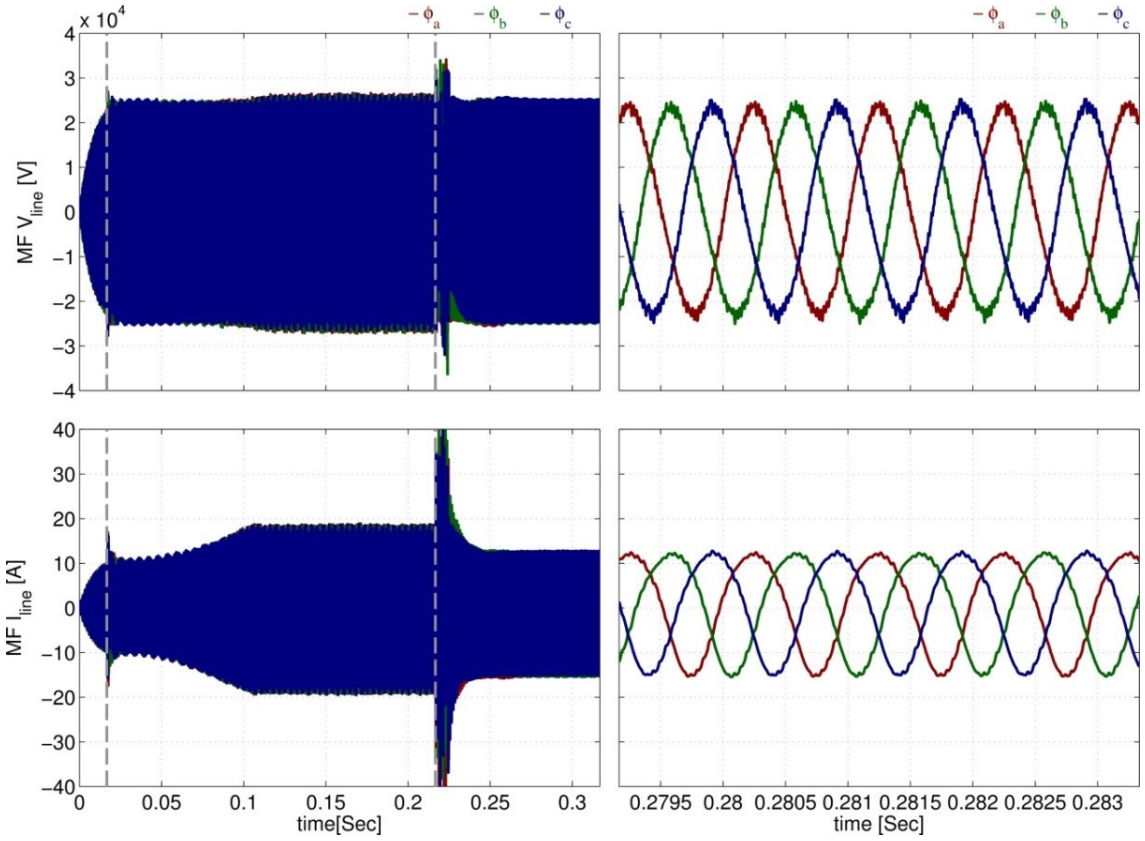

Figure 2–49. Medium Frequency grid time domain voltage and current waveforms during normal and faulty condition (right) zoomed out view (left) zoomed in view

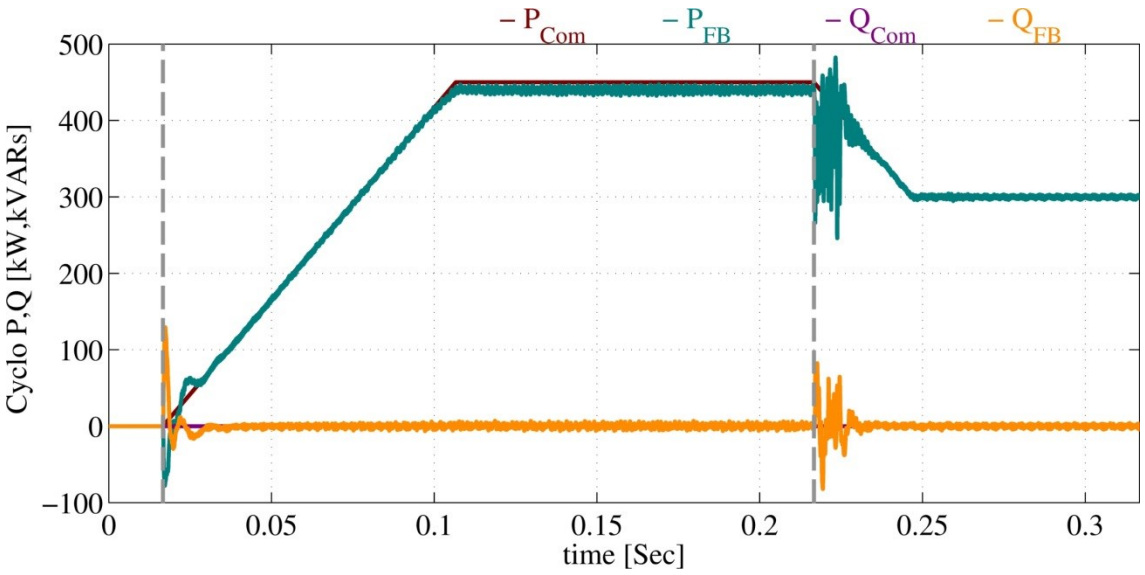

Figure 2–50. Cycloconverter active and reactive power closed loop time domain command tracking time domain response for normal loading and faulty condition

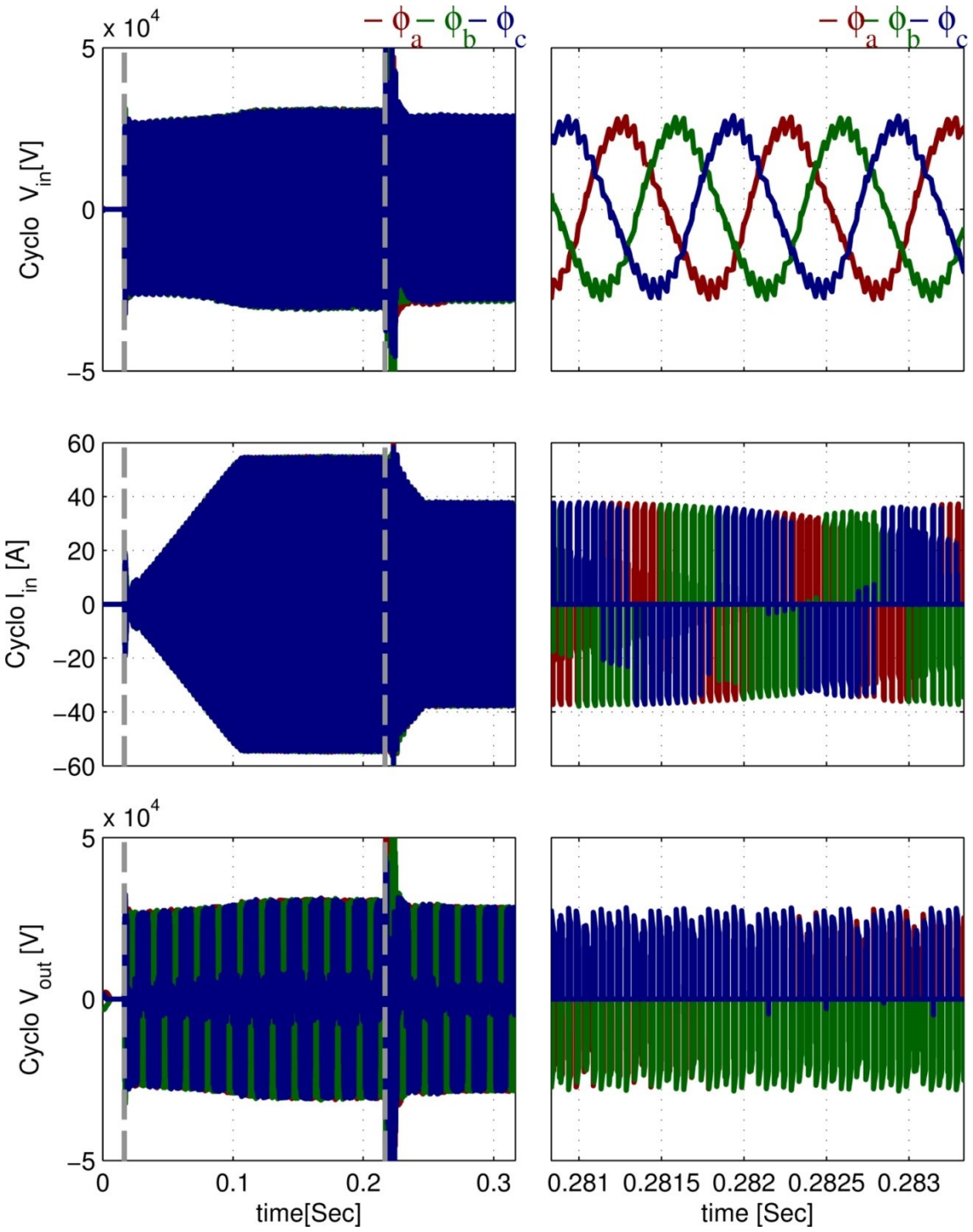

Figure 2–51. Cycloconverter time domain input voltage, input current and output switching voltage waveforms during normal and faulty condition (right) zoomed out view (left) zoomed in view

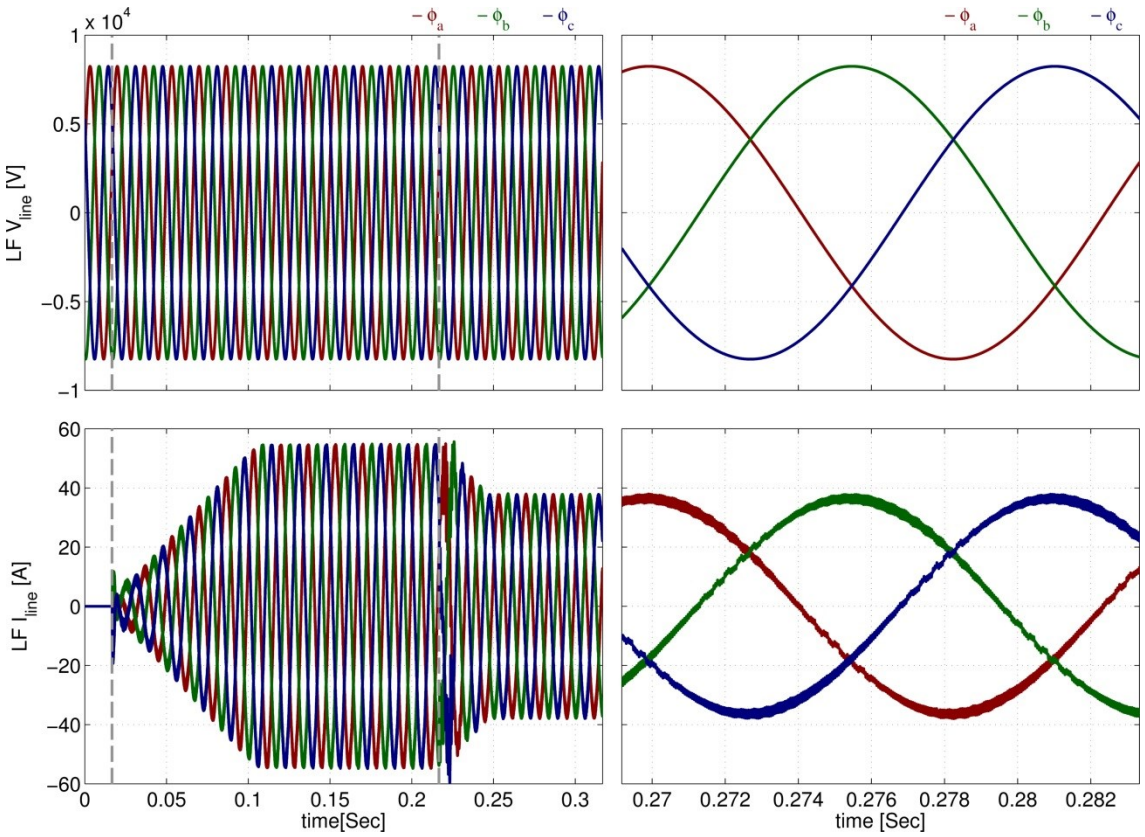

Figure 2–52. Time domain grid voltage and grid injected current during normal loading and faulty conditions (right) zoomed out view (left) zoomed in view

The cycloconverter, at the same time, decreased the commanded power to the sum of the available to maintain the normal operation as indicated by its command tracking performance in Figure 2–50. The input voltage, input current and output switching voltage of the cycloconverter are shown in Figure 2–51. Finally, the grid voltage and injected currents are shown in Figure 2–52 and they proof the seamless robust operation of the collection grid system during the fault.

2.4. Summary

This section shows in details new collection grid architecture for PV farms based on medium frequency transformers. The proposed system is analyzed and it is shown that the overall system efficiency will improve by 2% as shown Figure 2–53 and the transformer will decrease by one quarter. The system elements were desigend starting by the inverter, filters, cables, transformer and the cyclconverter. The designed transformer was verified usin FEA and it is shown to have a smaller size the conventional transformer. A control startegy was developed and verified in normal and fautly condition. A scaled down hardware protoype for the system will be shown in section 4.

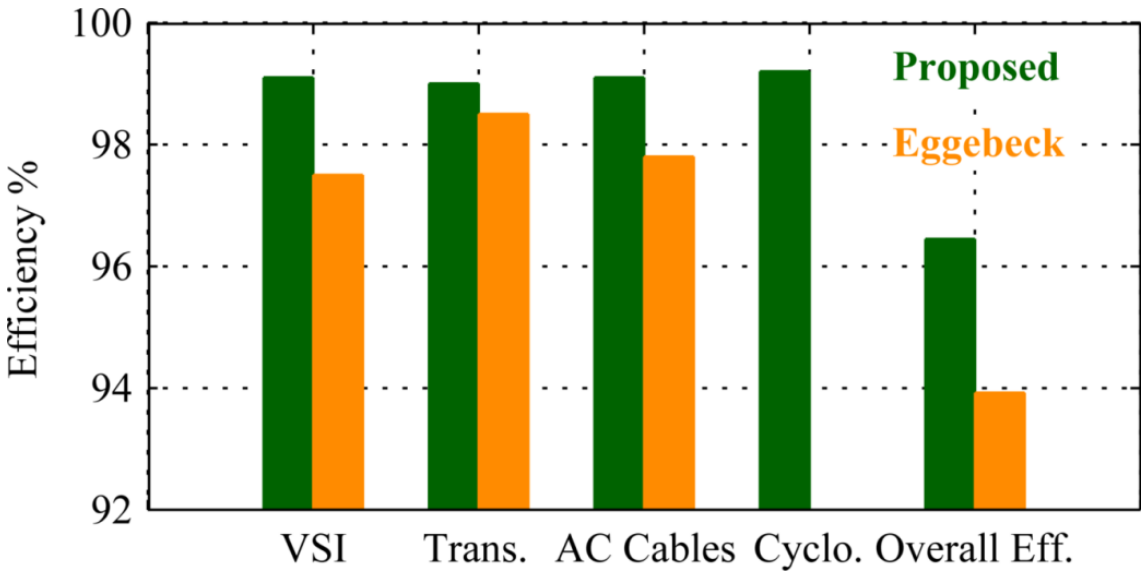

Figure 2–53. Overall system efficiency

3. DATA CENTER

A data center (DC) power distribution system (PDS) converts the utility grid voltage to the different voltage levels needed for the building, back-up, rack, etc. The total power required in some data centers is in the range of several megawatts[53]. A typical load distribution for a data center is shown in Figure 3–1 [54]. The cyber world gets bigger and bigger every day and the IT based loads is expected to double every year and the storage based loads are expected to increase by almost 70 times in the coming years[31]. With this huge market, the requirement for high density power supply is a must. This section of the thesis will introduce a new architecture for data center power supply by implementing a medium frequency and ac to ac converters that aims to increase the density of the power supply. It also includes a detailed analysis for the designed transformer and a comparison between two transformer designs options namely three limbs and five limbs transformers. A detailed simulation results are also included to validate the proposed structure. The key findings are summarized at the section end.

3.1. Introduction/ Existing Architecture

In this section, a medium-voltage (MV) data center power distribution system (DC-PDS) architecture using medium-frequency (MF) link transformer isolation is introduced. The proposed approach significantly improves power density while maintaining high efficiency compared to conventional line-frequency based solutions. The approach also contributes to a reduction in PVC or copper used in conventional DC-PDS. First the MV transformed from the utility, is interfaced

with a MV switch gear system and a diesel power generator (DPG) system. Then this MV is converted to the low voltages (LVs) required by the loads via MF transformer. The MF transformer primary side windings are connected to stacked AC-AC converters. The LV secondary windings are interfaced with several load systems and battery energy storage system (BESS) using different topologies like boost power factor corrector (PFC), PWM inverter, etc. The presence of MV switch gear and MF transformer in the architecture results in higher efficiency and power density.

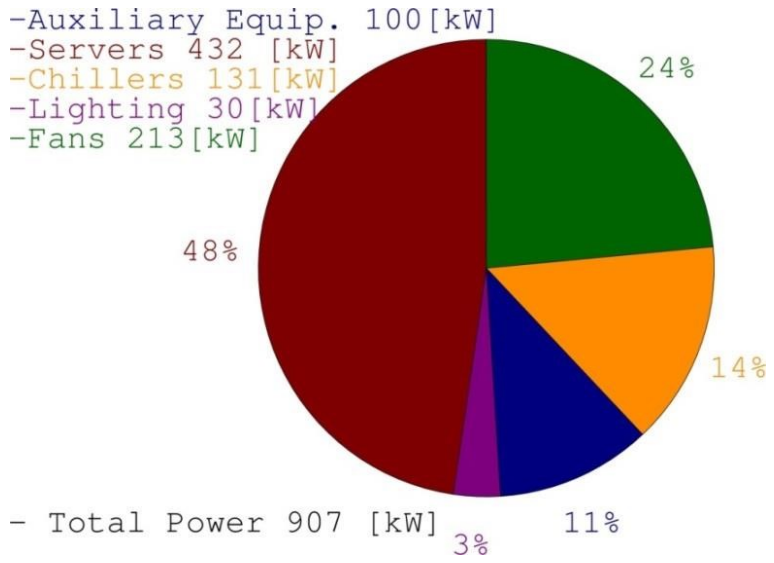

Figure 3–1. Power requirement for a typical data center [54]

The research efforts in boost Power Factor Correction (PFC) emerged a lot overtime due to the high demand of this power converter for IT and data storage loads. A conventional diode front end rectifier directly connected to the IT load, which is a nonlinear load, will result in a high input current harmonics that will impose high input

filter requirement and decrease the input power factor. A boost PFC provides the solution for such a problem; it forms an intermediate stage between the nonlinear load and the grid where it forces the input current to follow the grid voltage mimicking a resistive load operation. The common structure for this converter type is a diode rectifier followed by a boost converter, the diode rectifier can either be single phase or three phase depending on the input grid [55-57]. To decrease the output DC link requirement the output of these converters can be connected in parallel as in [58]. The boost PFC may also use transformers to provide isolation between the input grid and the output load [59].

The state-of-the-art DC-PDS architecture is designed around 480V systems , mainly because they are traditionally considered safe and most circuit breakers, uninterruptable power supplies, etc. are designed at that voltage [60]. When the power requirement is larger, medium voltage from the utility is initially stepped down to 480V using a line frequency transformer and then this is converted to the useful voltage levels in the data center (Figure 3–2) [53, 60-63].But for large power levels, 480V circuit breakers may be very large in order to quench the stronger arc; also the higher currents can make the overall system less efficient. In order to overcome these disadvantages, a 4160V based DC-PDS is proposed in [60]. While the 4160V circuit breaker system may be smaller in size, the distribution transformers operating at line frequency impacts the power density of the system and may add further to the cost. Figure 3–3 shows the diagram of a 4160V based DC-PDS.

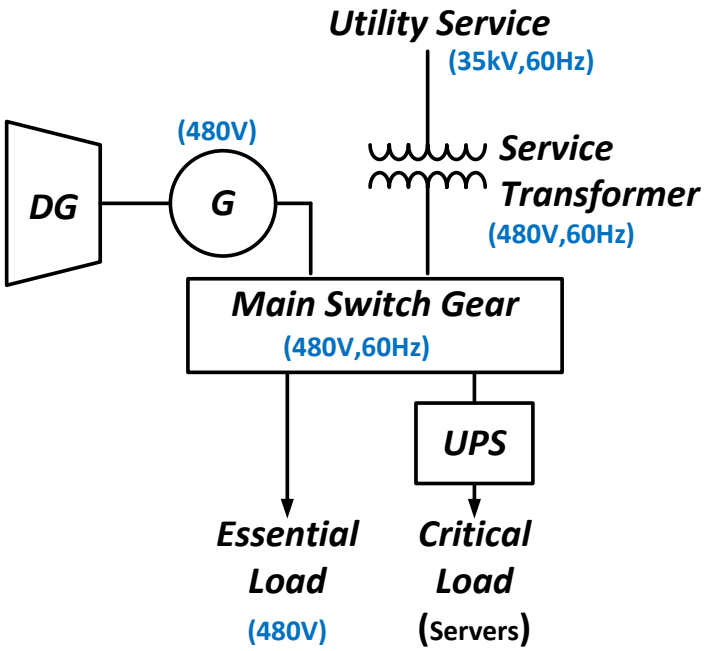

Figure 3–2. Conventional 480V data center structure [60]

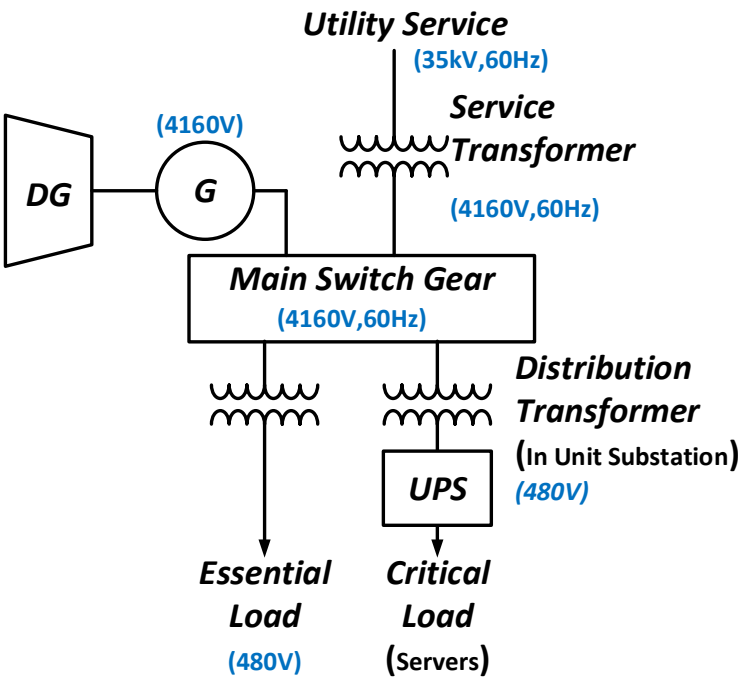

Figure 3–3. Medium voltage based data center architecture [60]

3.2. Proposed Medium Frequency Data Center Structure

In order to overcome the above-stated issues, this research proposes a MV DC-PDS architecture using medium frequency (MF) distribution transformer as shown in Figure 3–4. To employ a MF transformer, converters are needed on both sides to interface the transformer with the appropriate voltage and frequency for the operation of the critical loads, essential loads, BESS, etc.

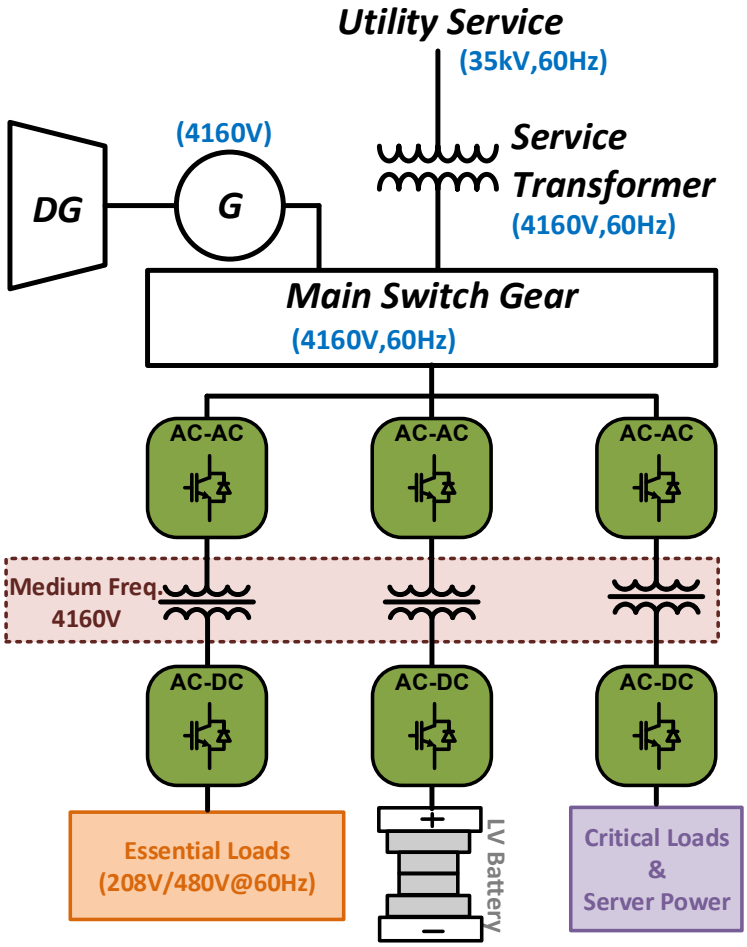

Figure 3–4. proposed data center structure based on MV-MF transformer

Figure 3–5 shows one of the approaches where a 3-port topology is used for this purpose, using AC-AC converters on the utility side, single phase-boost PFCs on the load side and a PWM inverter on the BESS side. The outputs of the single phase-boost PFC can be connected in parallel to lessen the reactive power requirement [56] Since the DC-link in the AC-AC converter is pulsating, electrolytic capacitors can be eliminated and the device voltage de-rating can be simplified; thus further increasing the power density. If there are more loads, supplementary windings can be added to the MF transformer or separate transformers themselves can be used. Also the AC-AC converter can be simplified to a uni-directional AC-AC converter with diode front-end if unity power factor has to be always maintained [64]. Figure 3–6 shows the proposed structure with a five limbs transformer. The following sections will include a detailed comparison between the two structures and a recommendation with the best solution is given.

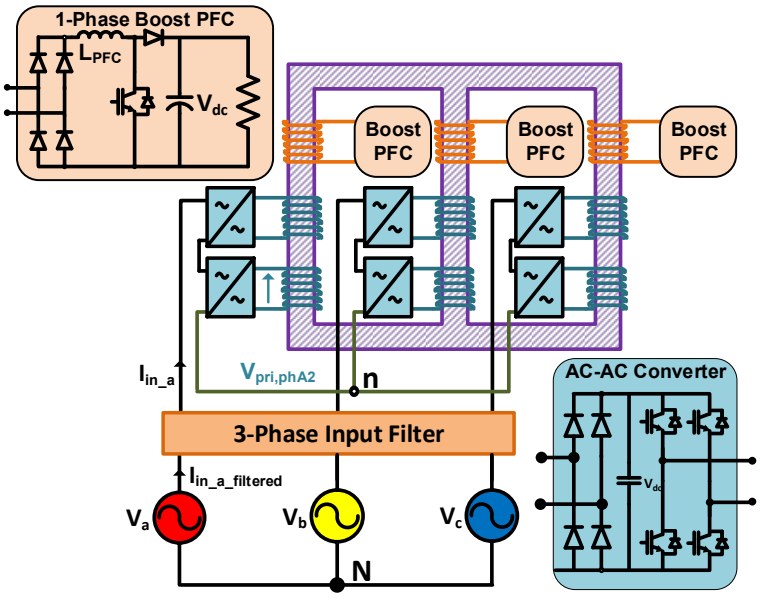

Figure 3–5. Details of the proposed data center MF-MV architecture using three limbs transformer

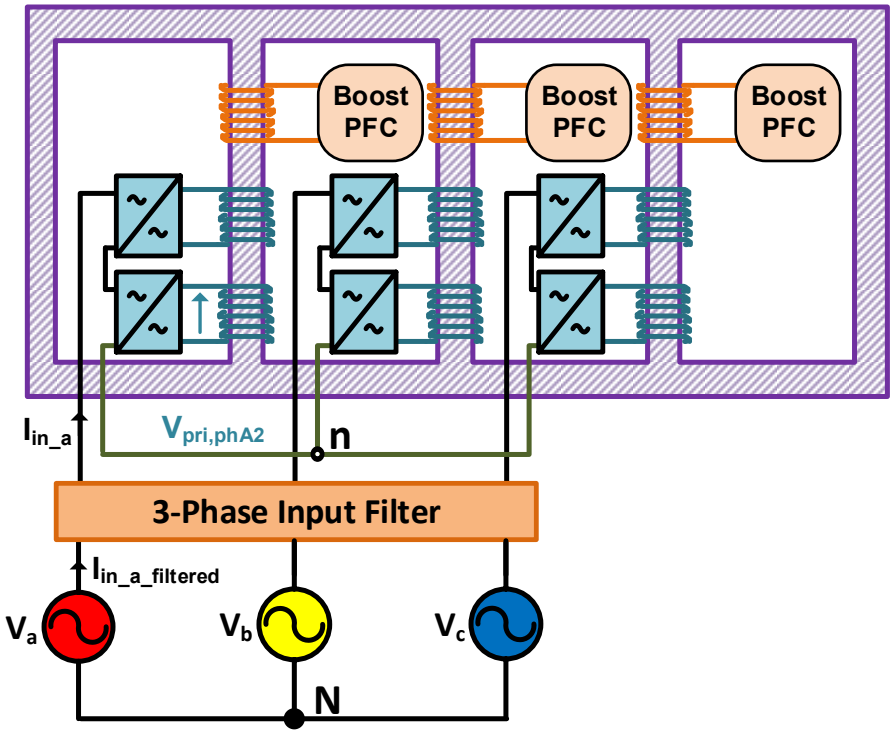

Figure 3–6. Details of the proposed data center MF-MV architecture using five limbs transformer

Advantages of the proposed DC-PDS architecture (Figure 3–4) are as follows:

- The MF link transformer provides galvanic isolation as well as proper voltage matching between the utility, the loads and the BESS. It also contributes to reduced size/weight while maintaining high efficiency [13].
- MV devices improve the overall efficiency – can contribute in better Power Usage Effectiveness (PUE) of the data center.
- The input side AC-AC converters are series connected, employing lower voltage IGBTs/ MOSFETs and voltage sharing is guaranteed by transformer coupling and input capacitors.

- As the AC-AC converters are switched at medium frequency, the switching losses are low.
- MV circuit breakers are smaller, less costly and better in response time compared to LV circuit breakers [60].
- This architecture can lead to significant reduction in PVC or copper used in conventional DC-PDS.
- The medium frequency voltage can be used to feed the lighting load. This will improve the fluorescent lighting [40].

Figure 3–4 shows the proposed DC-PDS architecture, using MV circuit breakers and MF transformer. The system is controlled to minimize the current harmonics and to improve the grid side power factor (PF). The entire PDS architecture in Figure 3–5 and Figure 3–6 can be divided into the following 5 sub-sections:

1. Multi-level AC-AC converter
2. Medium frequency transformer
3. 3-phase PWM inverter
4. Single phase-boost PFC
5. Loads and UPS.

3.2.1. Analysis and Simulation of the Proposed System

These five sub-sections are discussed below. The data center load reported in [54] is used as a reference for the presented design example and the load parameters are summarized in Table 3-1.

TABLE 3-1. DATA CENTER LOAD INFORMATION [54]

Direct use Power(kW)		**Supporting Equipment Power(kW)**			**Total Power**
Server Load	***Lights***	***Auxiliary equipment***	***Central Chiller***	***Fans and cooling***	
432	30	100	131	213	907

The architecture in Figure 3–4 is employed to supply the load. The total power can be processed through either one 1MW transformer or two 0.5 MW transformer where the voltage waveform is of a 60 Hz multiplied by Medium Frequency square wave. The diodes and IGBTs that are used in the PFCs are indicated Table 3-2. The single Phase PFC is switching at 20kHz.The three phase PWM rectifier comprise three IGBT modules [65] and the AC-AC converters comprises lower current IGBT modules in [66]. Each AC-AC converter module withstands 1200V so four of them will be cascaded to withstand the 4180V.

TABLE 3-2. DEVICES SELECTED FOR THE PROPOSED STRUCTURE

Inverter	**Rating**		**Selected Device**
	Current(A)	***Voltage(V)***	
Single phase PFC diode	208	480	240U(R) [67]
Three Phase PFC diode	360	480	SD403C[68]
Single phase PFC IGBT	208	480	IGW75N60T[69]
Three Phase PWM rectifier	360	480	FF450R12IE4[65]
AC-AC Converters	65	4160	FF100R12YT3[66]

3.2.1.1. Multi-Level AC-AC Converter

Each AC-AC converter block consists from one 1-phase H-bridge connected in back to back configuration with a single phase diode rectifier bridge since the power is in one direction. The AC-AC converter block has two tasks:

1- To convert the line frequency voltage (grid voltage) to medium frequency voltage (transformer primary voltage)

2- To convert the medium frequency voltage (transformer secondary voltage) to a low frequency voltage (three phase boost PFC input voltage).

The modularity and expandability are the main advantages of this approach. To withstand the high input voltage, several AC-AC converter blocks could be stacked in series where its output is connected to the transformer core using separate winding as in Figure 3–5, Figure 3–6. The flipped voltage waveforms are shown in Figure 3–7.

The frequency spectrum (FFT) of output voltage is shown in **Error! Reference source not found.**. The output is a multiplication of the input low frequency sine wave and higher frequency square wave switching function. The output voltage can be calculated using (3-1)-(3-3). As can be noted from the FFT graph, the fundamental frequency of the modulated voltage is equal to 940Hz and 1060Hz. That is equal to square wave frequency, 1 kHz, $\pm$ the grid frequency, 60Hz. The rest of the voltage components appear at the odd multiples of the square wave frequency as expected.

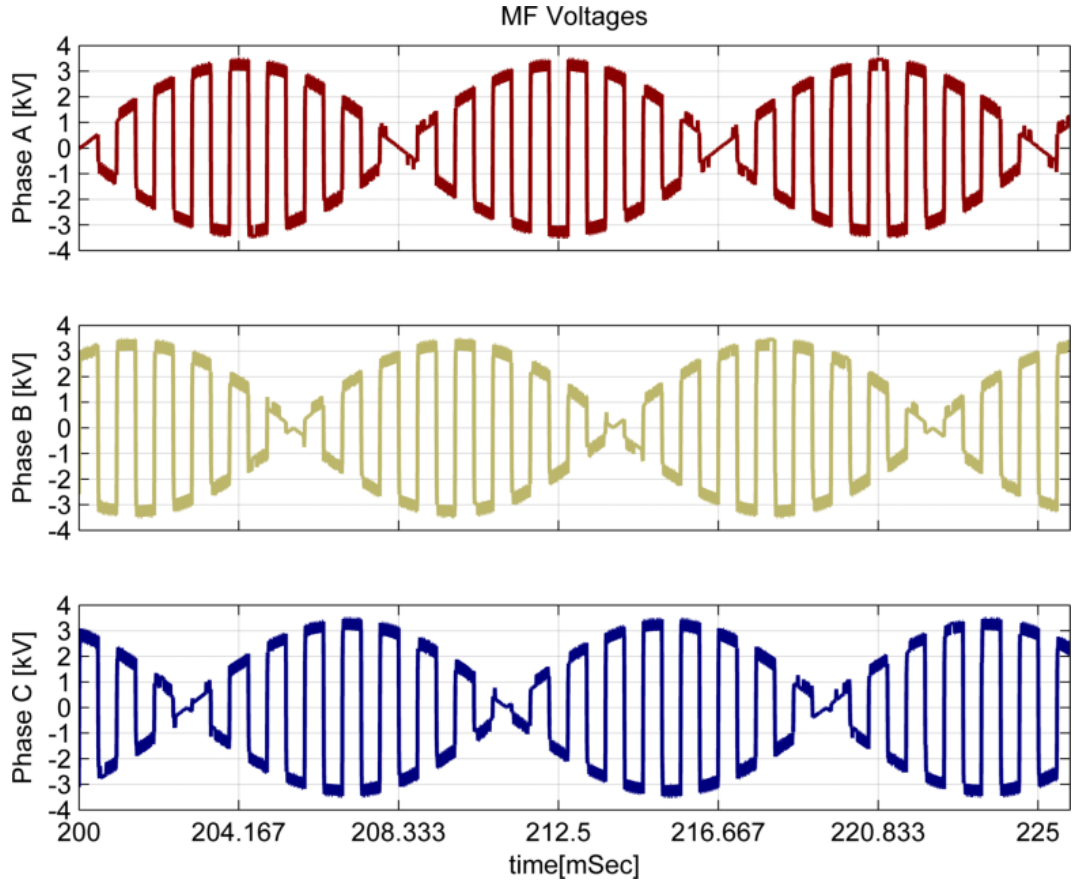

Figure 3–7. The flipped(modulated) grid input voltage waveform after the AC to AC converter

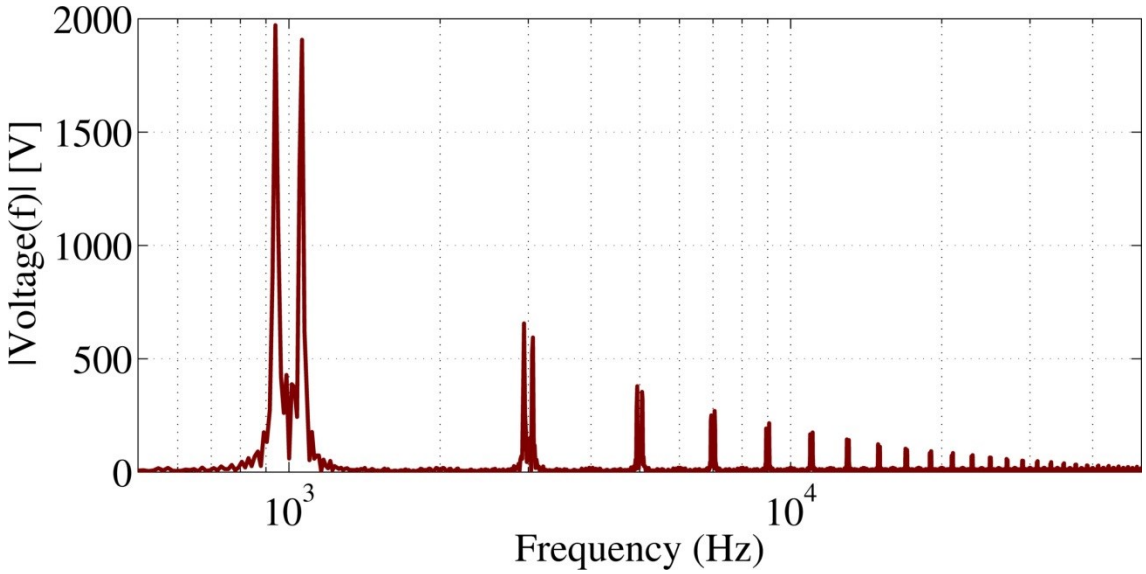

Figure 3–8. FFT of the medium frequency modulated grid voltage (transformer voltage)

$$V_g = \sqrt{2} * V_{rms} * \sin(\omega_g * t) \tag{3-1}$$

$$Square = \frac{4}{\pi} * \sum_{n=1,3,5....}^{\infty} \frac{1}{n} \sin(n * \omega_s * t) \tag{3-2}$$

$$V_{mod} = V_{rms} * \begin{bmatrix} 0.9 * \sin[\{\omega_s \pm \omega_g\} * t] \\ +0.23 * \sin[\{3\omega_s \pm \omega_g\} * t] \\ +0.15 * \sin[\{5\omega_s \pm \omega_g\} * t] \\ +high\ order\ terms \end{bmatrix} \tag{3-3}$$

where V_g is the input grid voltage, square is the modulation square signal and V_{mod} is the final modulated signal

3.2.1.2. Medium Frequency Transformer

The MF transformer is the core of the proposed structure. High power density is its main advantage for application where the overall system size is of high importance such as wind-turbines[64] and traction [70]. A MF transformer is designed using the same approach as in the PV farm section. The transformer parameters are in Table 3-3.

TABLE 3-3. DATA CENTER TRANSFORMER SPECIFICATIONS

Input voltage	4100 V
Output voltage	200 V
Rated power	150 kW
Connection	Delta/Star

The maximum efficiency transformer designs are in Figure 3–9- Figure 3–12 and the minimum size designs are in Figure 3–13-Figure 3–16. As mentioned in the

previous section, the maximum efficiency designs are implemented when the required transformer efficiency is the main system concern but when the size is the biggest concern the min size designs should be adopted. This is the main reason that when comparing the flux utilization is the two designs in Figure 3–9 and Figure 3–13 one can notice that the flux for min size is fixed to 85% of the maximum flux density while it is adapted (relaxed) to lower values based on the design criteria in Figure 2–11 to achieve higher efficiency. The direct result for this appears in area product and expected efficiency graphs. We can notice that to achieve higher efficiency, Figure 3–11, the operated flux density should be decreased which means higher area product as in Figure 3–10, i.e. transformer size.

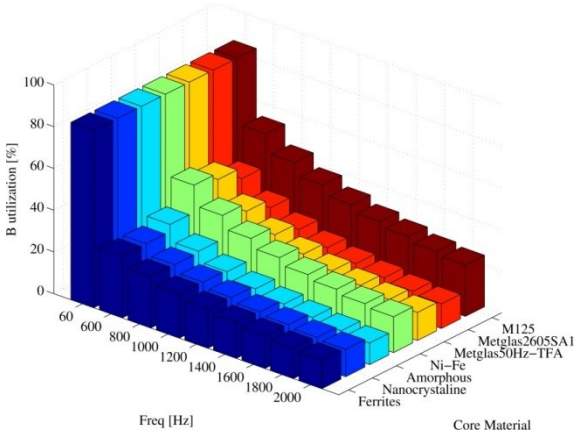

Figure 3–9. Max efficiency transformer flux utilization ratio

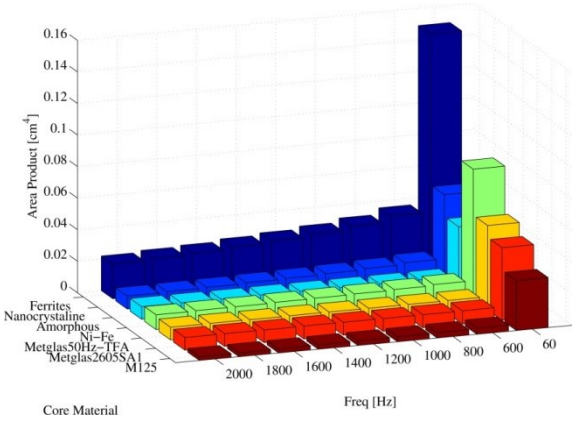

Figure 3–10. Max efficiency transformer area product

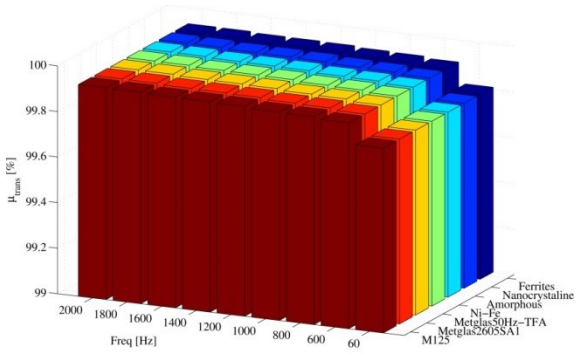

Figure 3–11. Max efficiency transformer expected efficiency

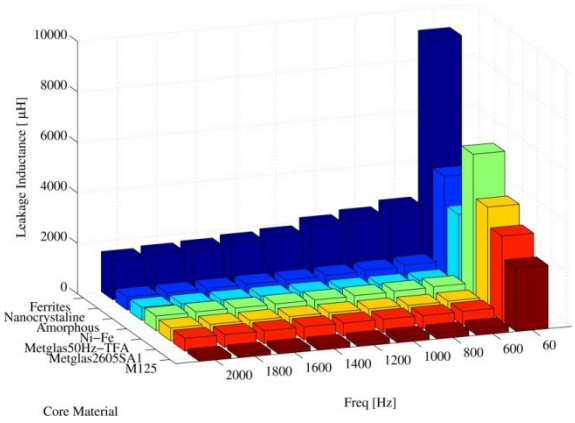

Figure 3–12. Max efficiency transformer leakage inductance

When compared to their min size counterparts in Figure 3–11 and Figure 3–10 respectively. The leakage inductance is of important factor for this design, the lower its value the better the transformer performance, its value determines the notch in the transformer current during the switching moments. The expected leakage inductance value for max efficiency is in Figure 3–12 and for min size is in Figure 3–15.

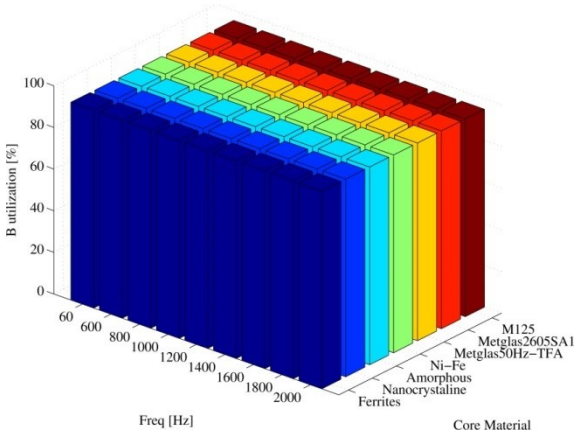

Figure 3–13. Min size transformer flux utilization ratio

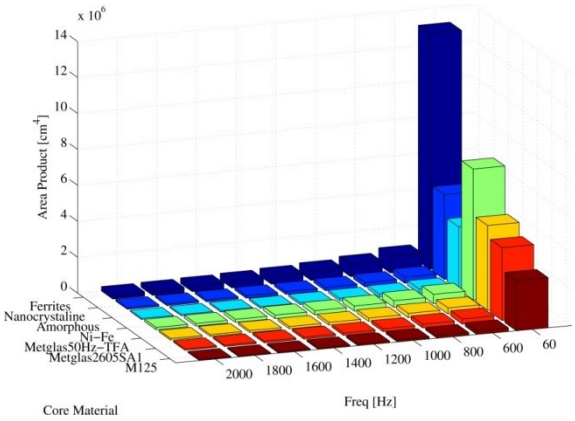

Figure 3–14. Min size transformer area product

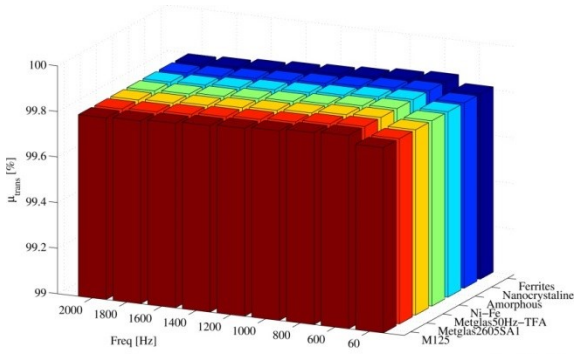

Figure 3–15. Min size transformer expected efficiency

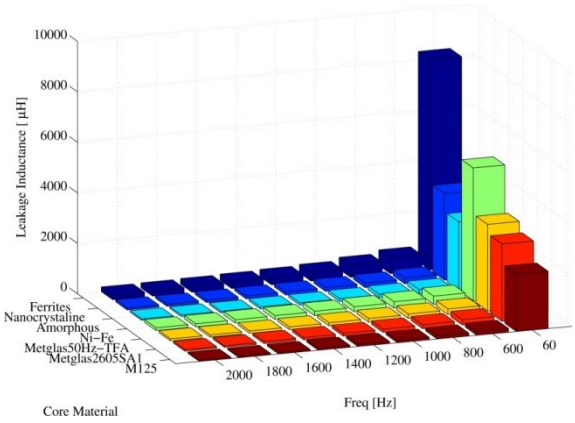

Figure 3–16. Min size transformer leakage inductance

3.2.1.2.1. Three Limbs Vs Five Limbs Transformer

The minimum size transformer design is selected and verified using ANSYS-Maxwell; it is selected because it is the maximum priority in this application. The mechanical parameters are used to build two transformers, the first with three limbs, Figure 3–17, and the second with five limbs, Figure 3–18. The five limbs transformer is considered to accommodate the effect of the zero sequence current that may result from switching of the ac to ac converters. For the three limbs design, the magnetic circuits for the two outer limbs are not equal to the middle limb that will result in different inductance between the three limbs and since the fundamental frequency power is shifted at medium frequency range, the equivalent impedance will be bigger and will result in different current between the three limbs because they experience the same input voltage. On the other hand, the five limbs design result in the same magnetic circuit for the three phases hence the inductance will be equal and resultant phase current will be equal to each other.

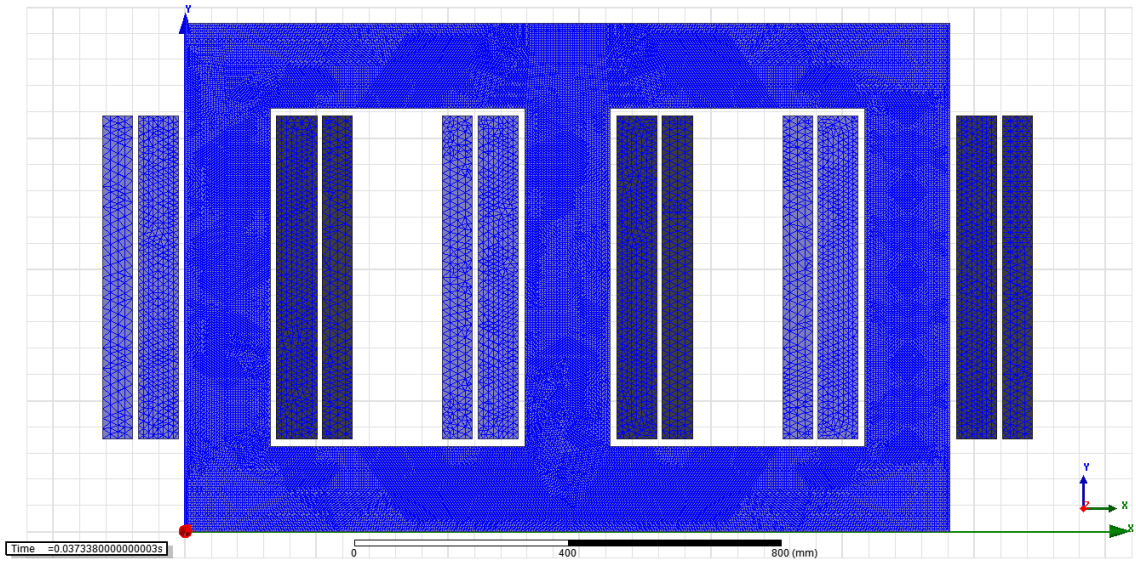

Figure 3–17. Three limbs – three phase transformer

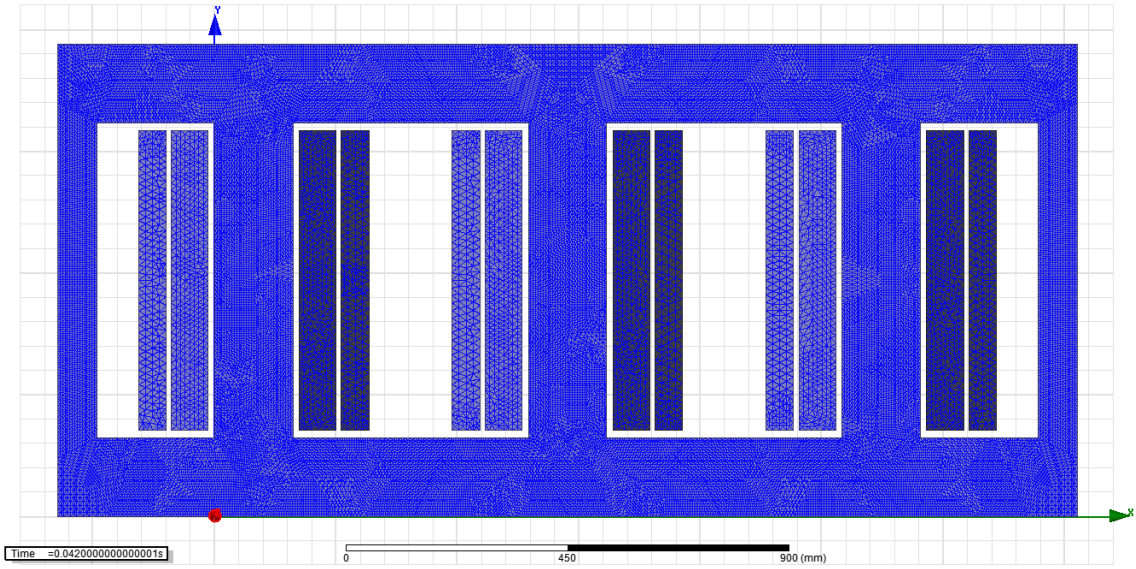

Figure 3–18. Five limbs – three phase transformer

The time domain voltage and current waveforms for the two transformers are shown in Figure 3–19 and Figure 3–20. The current and voltage waveforms are confirming the design values. To further investigate the differences between the two designs, two more simulations where run where different dead band values were imposed on the H-bridge converters switching moments to encounter for real world switching. The dead band values were 4uSec and 8uSec for phase B and Phase C converters respectively. The summery of the two transformers currents and voltage waveforms are shown in Figure 3–21. The first impression that they all have a symmetric performance except for some tiny current notches in the three limbs transformer primary currents in case of different dead band.

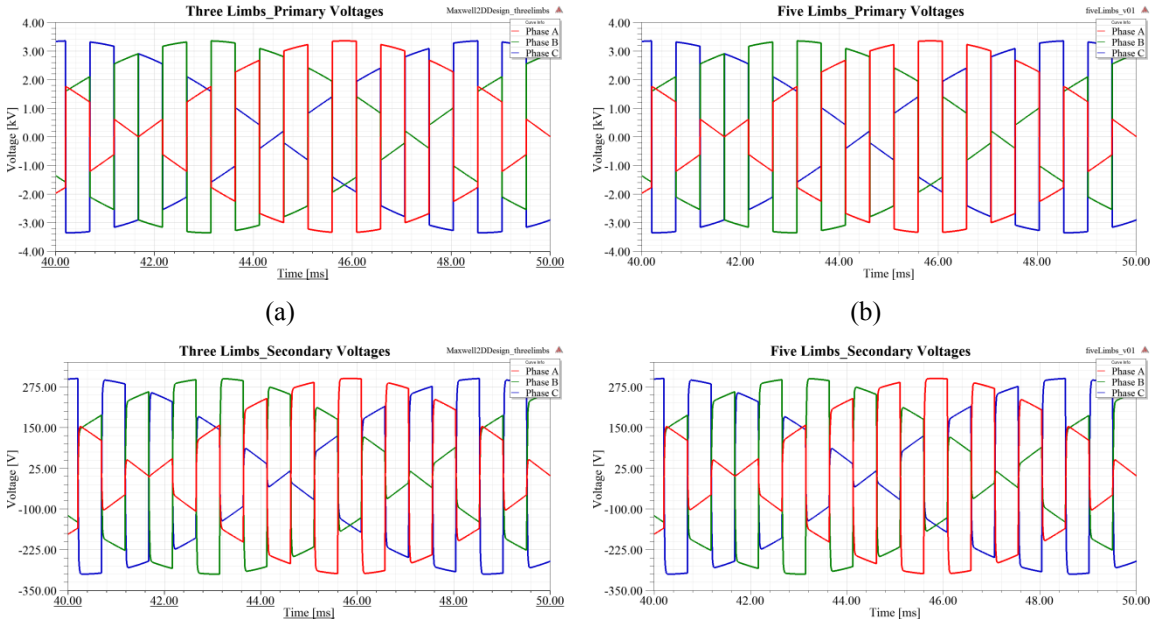

Figure 3–19. Time domain wave forms for three limbs transformer (a)primary voltages (c) secondary voltages , five limbs transformer(b) primary voltages (d) secondary voltages

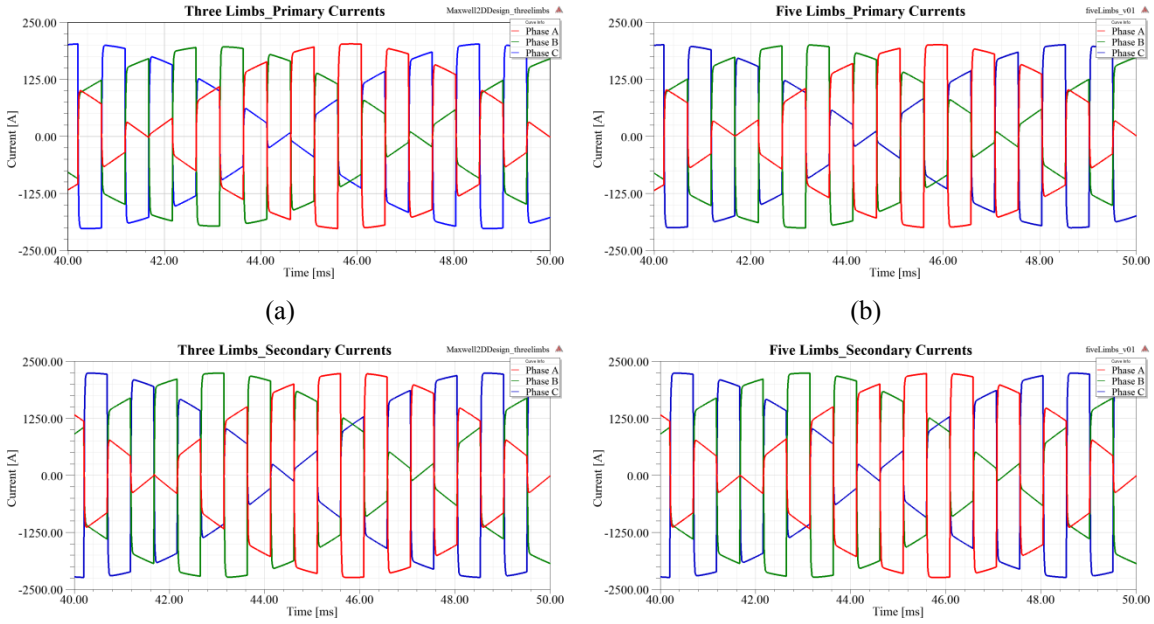

Figure 3–20. Time domain wave forms for three limbs transformer (a)primary currents (c) secondary currents , five limbs transformer(b) primary currents (d) secondary currents

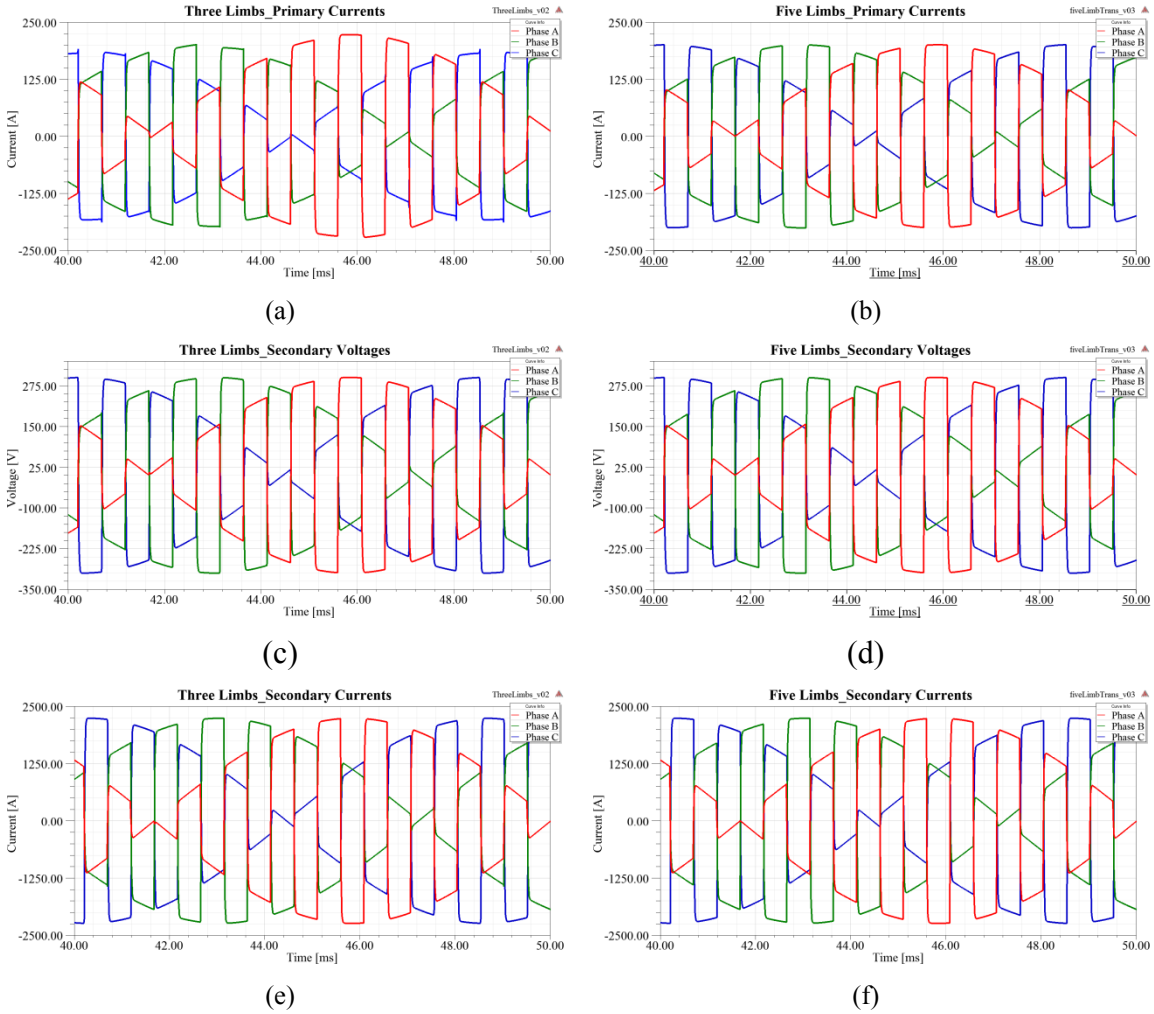

Figure 3–21. Time domain waveforms for the proposed structure with different dead bands (a) three Limbs primary currents (b) five limbs primary currents(c) three limbs secondary voltage (d) five limbs secondary voltages (e) three limbs secondary currents (f) five limbs secondary currents

Figure 3–23 gives closer look at the primary current FFT in Figure 3–22 and it reveals the reason for the difference for the average neutral current values for the cases with and without dead bands in Figure 3–24. As expected the five limbs transformer provides a more symmetric magnetic circuit for the three phases therefore the three phase applied voltage will experience almost identical impedances that will results in similar three phase current amplitudes at the different frequency fundamentals and the

odd harmonics. On the other hand, the three limbs transformer design will have different current amplitudes at the same frequency values that will result in an average neutral current values and its value will increase during the different dead band cases. If this neutral current is not allowed to pass, the common mode voltage of the transformer will increase and may cause a protection trigger due to the fact that the transformer body should be grounded to provide protection for human.

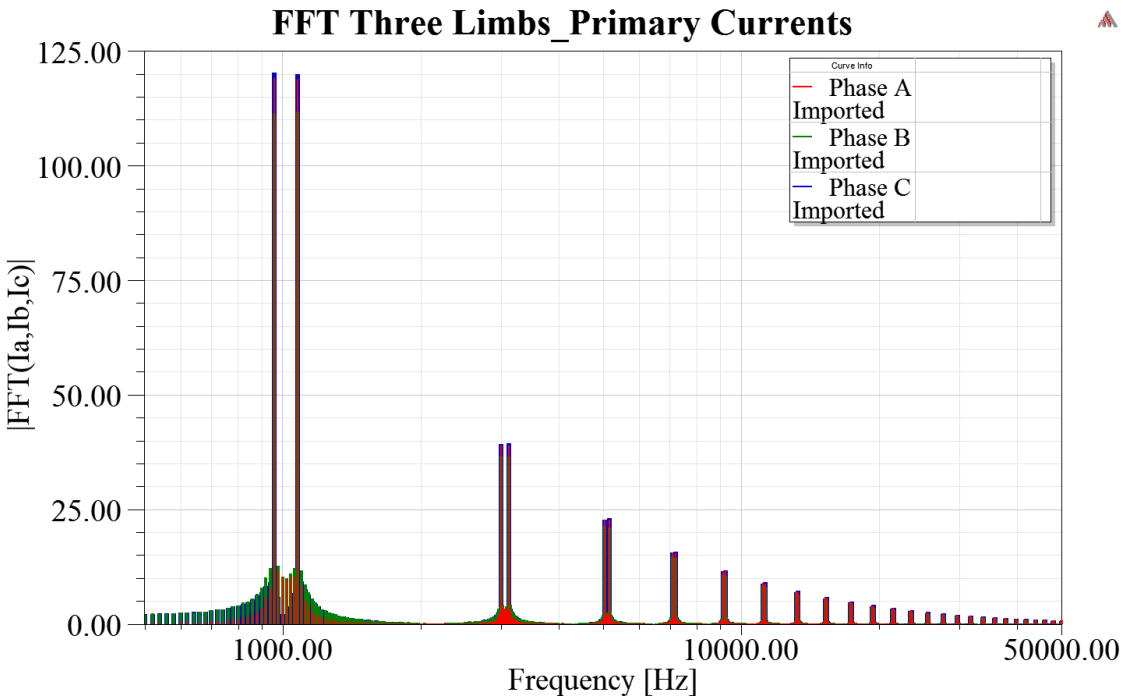

Figure 3–22. Frequency domain response for the three limb- three phase transformer line current in case of no dead band

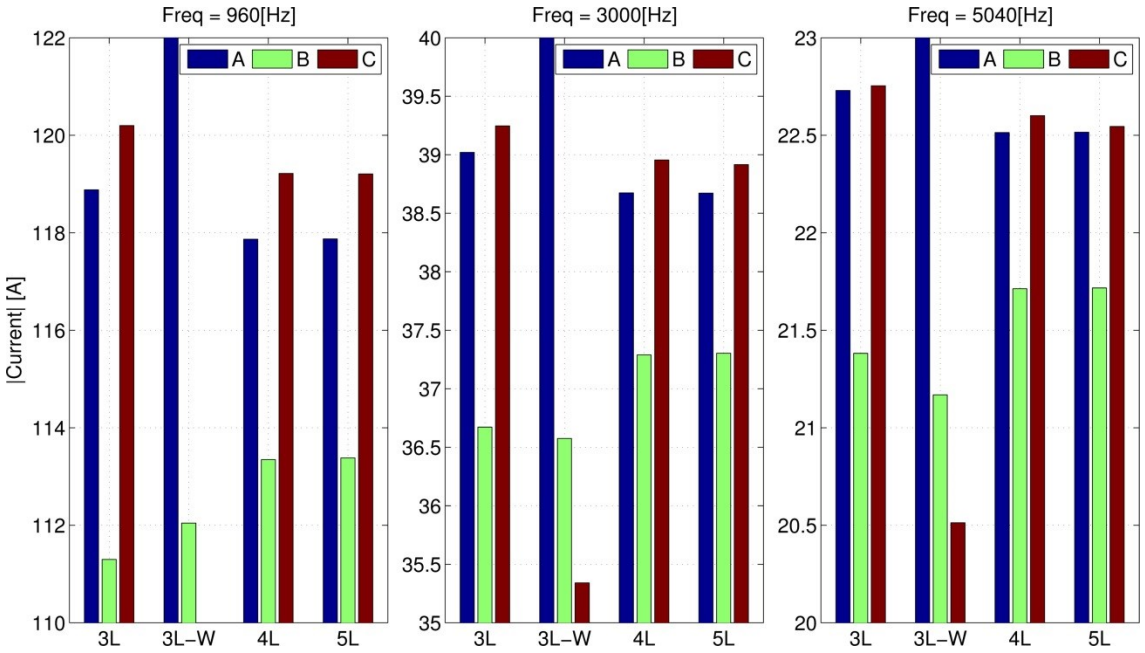

Figure 3–23. Zoomed in view for the frequency domain graphs for the three limbs and five limbs transformer designs during no deadband and with different deadband simualtions at 940Hz,300Hz and 5000Hz

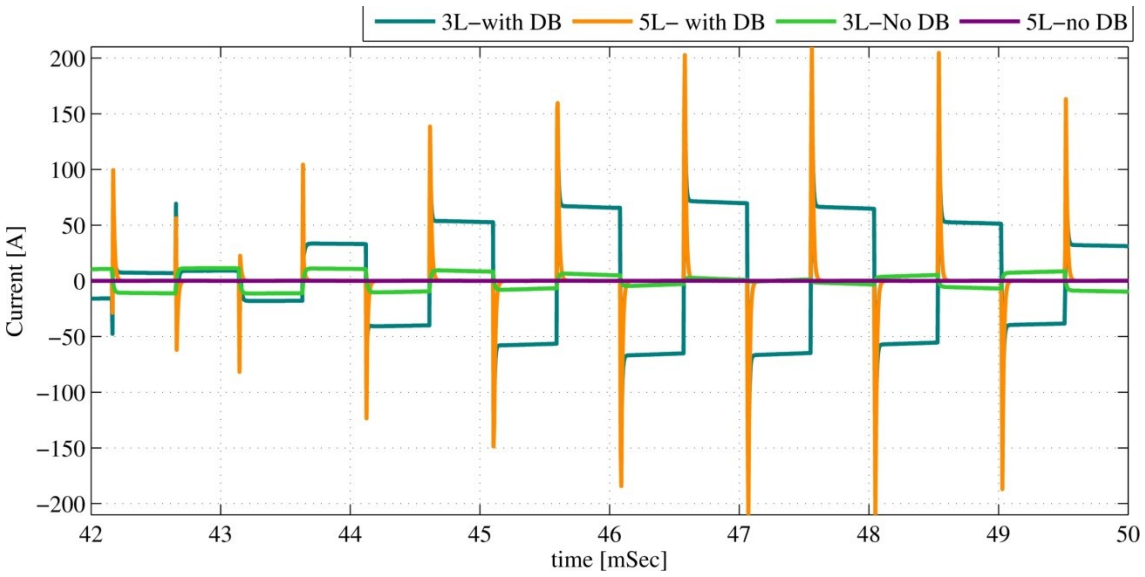

Figure 3–24. Neutral current time domain waveforms for three limbs and five limbs transforms with and without different deadband simualtions

The core losses are in Figure 3–27 the efficiency for the two transformers are 99.91%, three limbs, and 99.85%, five limbs. The two has low losses, as expected, and the five limbs transformer has more core loss than the three limbs one due to the two extra limbs. The flux distribution for the three limbs transformer is in Figure 3–25 and the five limbs transformer is in Figure 3–26. It can be noted that the flux density is lower in the five limbs transformer when compared to the three limbs, this due to the fact that the transformer core is bigger and this is expected to overcome the zero sequence current problem that is resulted during the non-ideal real world switching .

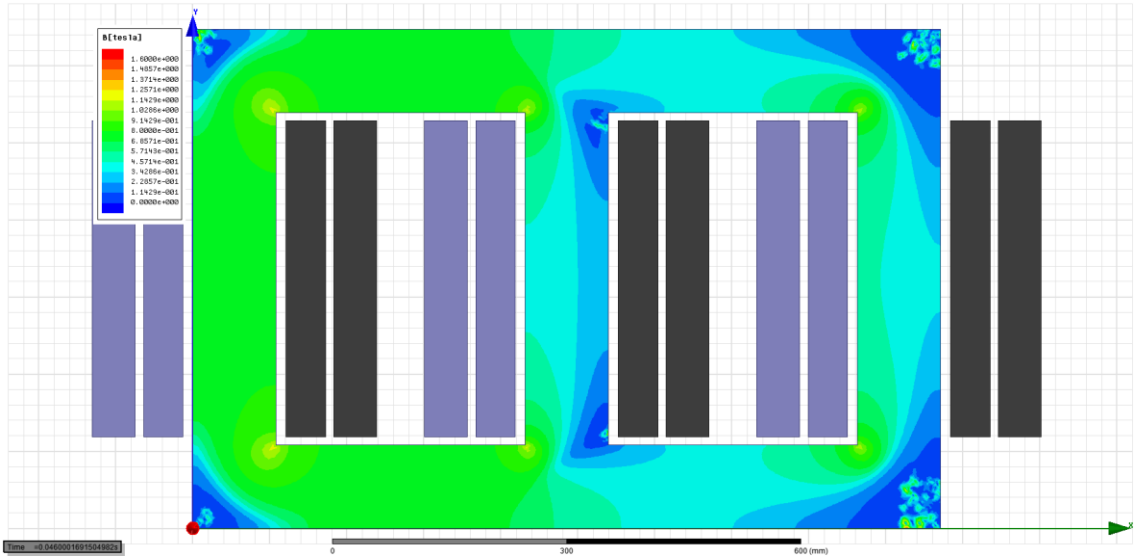

Figure 3–25. Flux distribution for the three limbs transformer at 46 msec

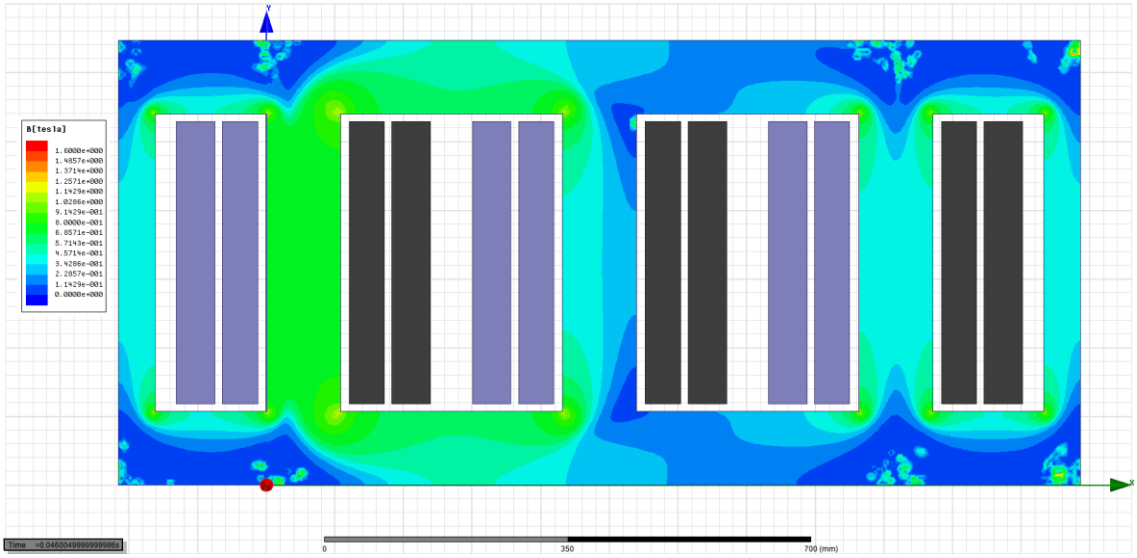

Figure 3–26. Flux distribution for the five limbs transformer at 46 msec

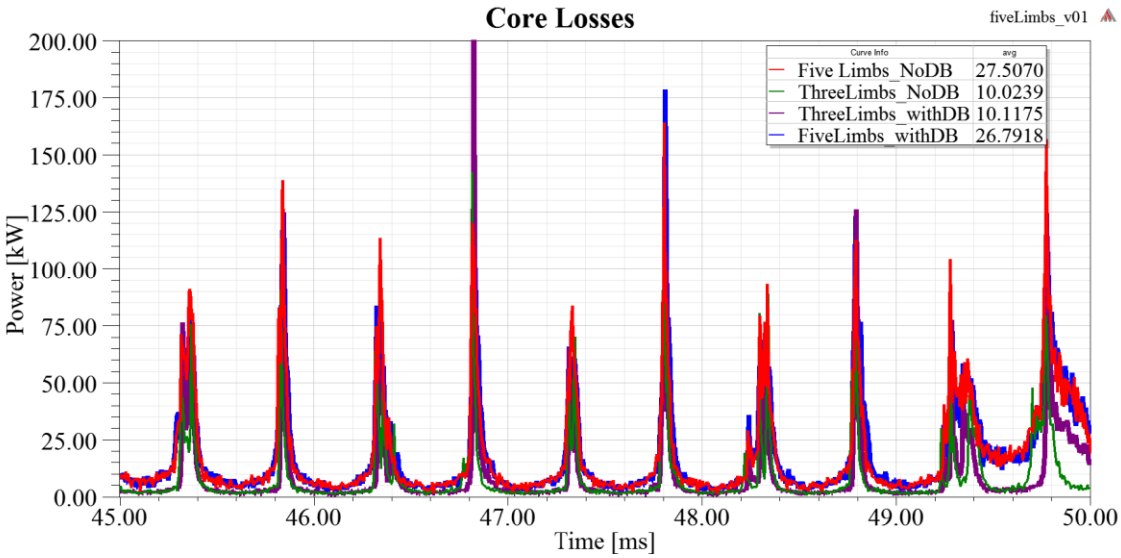

Figure 3–27. Three limbs and five limbs transformers core losses

3.2.1.3. Three Phase PWM Inverter

For bi-directional active power transfer across the transformer, the inverter should generate all the major frequency components present in MF transformer primary windings. Thus, the switching function of the PWM inverters must be a product of a line frequency sine PWM and a medium frequency square wave, appropriately phase-shifted depending on the amount of power to be transferred. It is used to interface the BESS to the loads. Its controller consists of PI regulators implemented in the rotating frame [64]. There is another AC-AC converter that supplies to the essential loads, cooling fans, etc that require the line frequency AC. It can also be constructed using a uni-directional AC-AC converter with diode front-end. The output voltage waveform is shown in Figure 3–28.

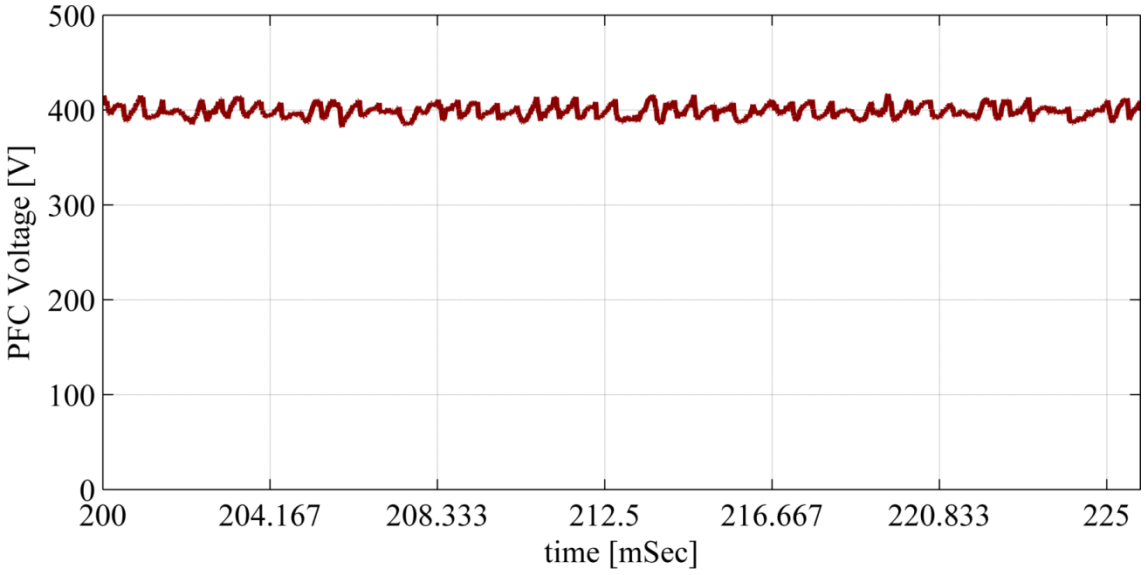

Figure 3–28. Output voltage waveform for the three phase PWM inverter

3.2.1.4. Single Phase Boost PFC

The 1-phase boost PFC stages provide another DC output port for the DC loads. Its structure is shown in Figure 3–5 as in [56]. Its controller provides a constant DC output and unity input power factor for the modulated sine-wave.

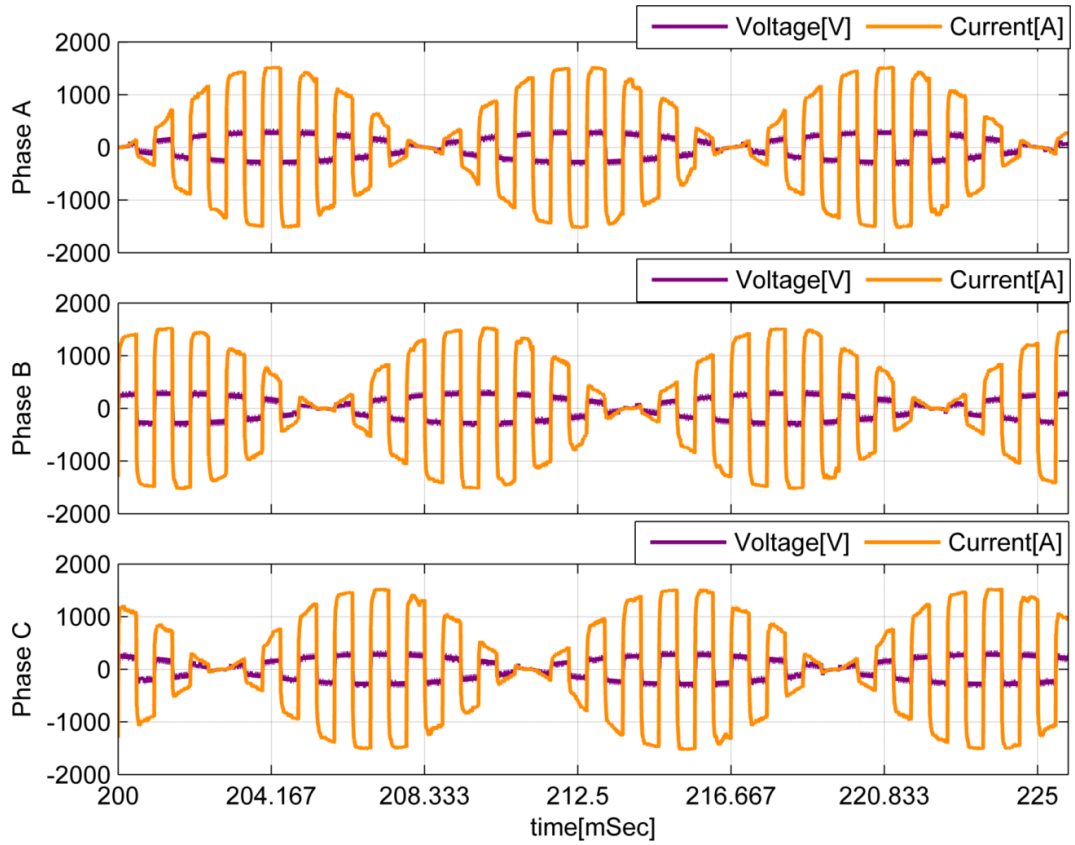

Figure 3–29. Input voltage and current for the three single phase PFC

The boost PFC stages can be operated in the 3-phase mode, where the DC outputs from the three phases are connected in parallel to form a single DC-bus for large loads, thus the reactive power can be compensated. The control algorithm has two loops, inner current loop and outer voltage loop. The inner loop controller could be either a

hysteresis controller or a PI controller. This loop has a high bandwidth; around 20 kHz. The outer voltage loop consists from a PI controller with a low bandwidth of about 20 Hz[71]. The three single phase PFC correctors input voltage and current are shown in Figure 3–29 and their output voltages are shown in Figure 3–30.

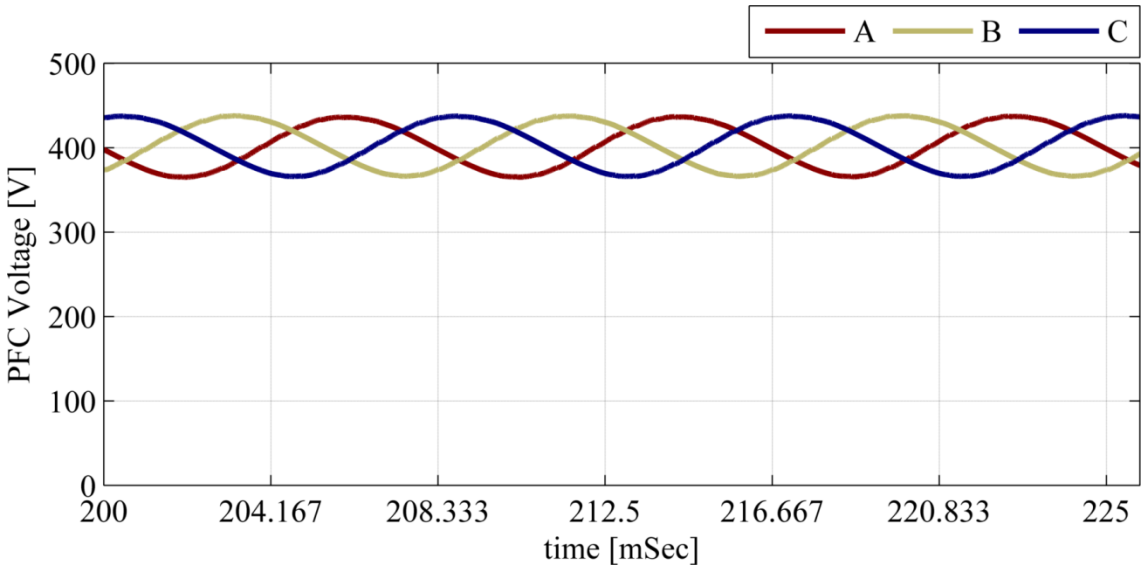

Figure 3–30. Output voltage waveforms for the three single PFC

3.2.1.5. Loads and UPS

The data center loads are primarily servers, cooling system, etc. The loads can be AC or DC and thus can be supplied by the different converter sections of the architecture as explained. The BESS and the DPG systems provide back-up power for the servers in case of a fault in the utility power grid. The DC-DC or DC-AC converters used from the distribution side to the server side for utilization are not the focus of this paper.

The grid voltages and currents are shown in Figure 3–31 and Figure 3–32. The former is for the unfiltered waveforms and the latter is for the filtered waveforms.

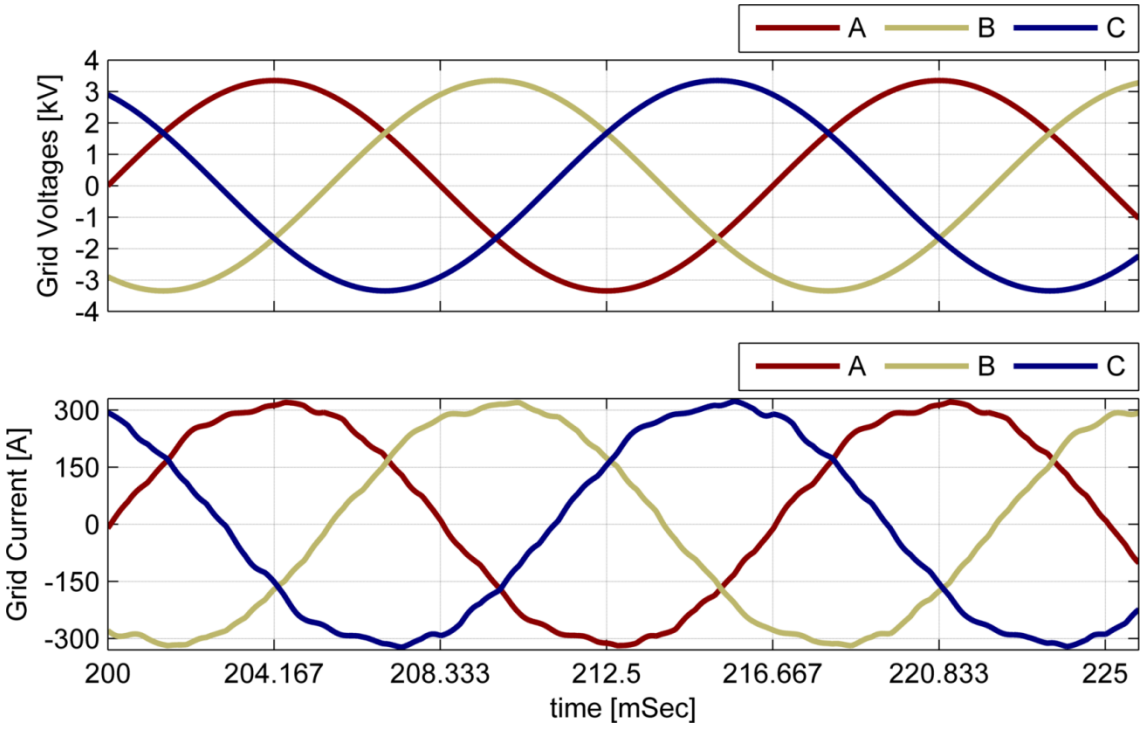

Figure 3–31. grid filtered input voltages/currents

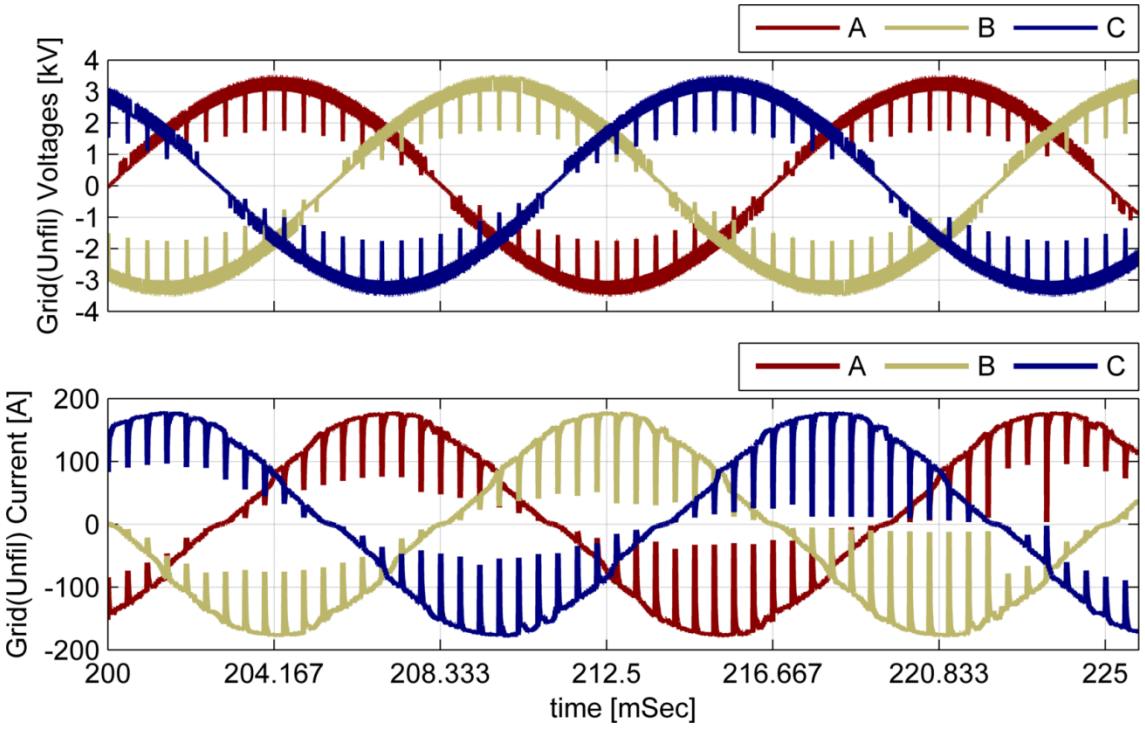

Figure 3–32. grid unfiltered voltage/current

3.3. Summary

MV data center power distribution architecture was proposed in this section that uses medium-frequency (MF) link transformer isolation. The proposed architecture is constituted using MV switch gear, MF transformer, battery storage systems, etc. The MV to LV conversion is implemented via a MF transformer based converter system. Simulation results proved the validity of the concept. MV switch gear and MF transformer together contribute to higher system efficiency and power density. Three limbs and five limbs transformer designs were investigated and the five limbs transformer proofed to be the best candidate within the structure because it provides a symmetric impedance transformer for the three phases that makes it more immune to zero sequence and higher order harmonics. The following section shows a scaled down lab prototype as a proof of the concept.

4. HARDWARE RESULTS

This section presents the hardware results for the proposed two structures. It first starts with the utility scale PV structure and explore different operating scenarios that include steady state vs. transient, normal vs. faulty. These different scenarios are used to fully test the proposed controller and verify its robustness. The second section presents the results for the data center structure and provides detailed waveforms for the circuit variables.

A TI TMS320F28335 DSP is used as the system controller[72]. It is programmed using Matlab/Simulink embedded coder toolbox[73]. A modular three phase inverter setup is used as a building block to construct the two proposed structures; it comprises SK13GD063 Semikron power module and SKHI61R Semikron gate driver circuit[74, 75]. ValueCAN3 is used for real time communication with the DSP that provides a way to debug/tune the controller and change the command to implement the different operating scenarios [76] .

4.1. Utility Scale PV Farm

The lab setup for utility scale PV is shown in Figure 4–1, it comprises five PWM based inverter modules. Inv#1, Inv#2 and Inv3 represent the PV connected inverters and they have the same voltage closed loop controller. This controller has only one control loop that is closed on the voltage and it is not responsible for the current. The output of each of these inverters is connected to the input of the medium frequency transformer. The transformers' outputs are series connected to construct the MF collection grid. Inv#4

and Inv#5 form the AC to AC converter that is responsible to interface the MF voltage to the utility grid. Inv#4 acts as an Active Front End Rectifier [77]. It forces the MF grid current to be in phase with the MF grid voltage. It has two control loops, the inner is current control loop and the outer is voltage control loop. The outer voltage control loop is controlling the voltage over the C_{AFER} to a fixed value and in the same time the inner current loop controls the input current from the MF grid to achieve this target. Inv#5 is the final stage that is controlling the injected grid current. It forces the injected current to be in phase with the grid voltage using a PR controller.

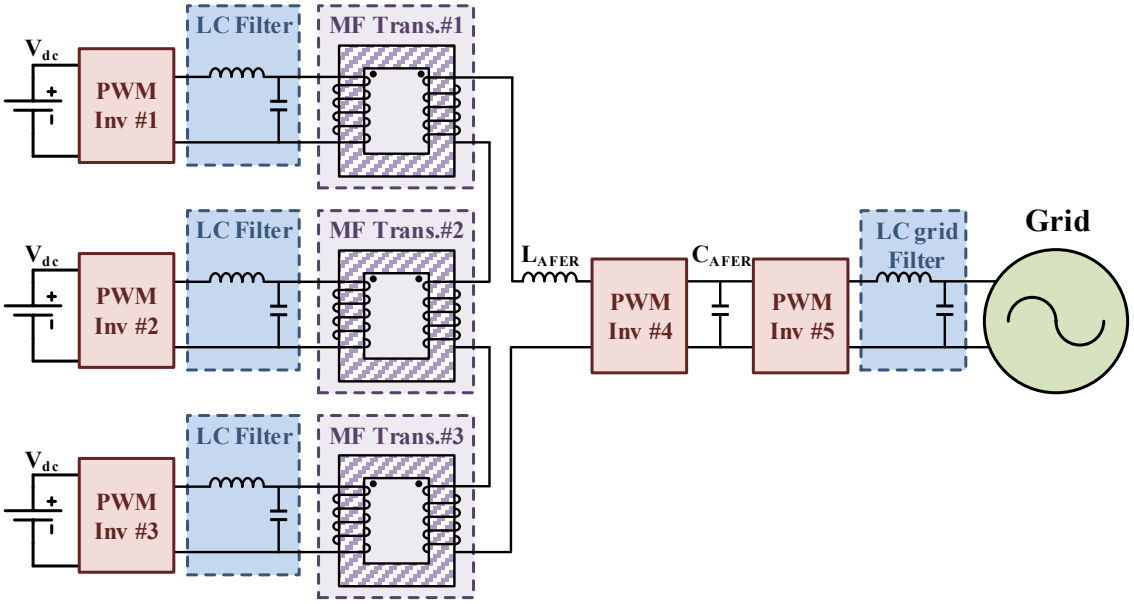

Figure 4–1. PV farm lab setup arrangement

TABLE 4-1. PV SETUP CIRCUIT PARAMETERS

Parameter	Value
DSP switching frequency	8 kHz
PV Inverters DC link voltage	50V
Medium frequency	200Hz
AFER DC link voltage	100V
Grid voltage (rms)	40V
Grid frequency	60Hz
Grid current (peak)	2.5A
L (LC filter)	220uH
C (LC filter)	5uF
L_{AFER}	6mH
C_{AFER}	580uF
L(LC grid filter)	1mH
C(LC grid filter)	60uF

The circuit parameters are summarized in Table 4-1. One DSP is used control the whole structure for the sake of reducing complexity but this increases the computation burden on the DSP therefore the switching frequency is limited to 8 kHz. This is the maximum achievable switching frequency for the DSP to control the five inverters and this is the sole reason to limit the MF grid frequency to 200Hz. The system can operate at higher frequency values without any problem if several DSPs were used, which is the case for real world implementation.

TABLE 4-2. PV DIFFERENT CASES VOLTAGES

Case	Inv #1	Inv #2	Inv #3	MF Voltage
Min Inverter	25	25	25	75
Normal Inverter Voltage	30	30	30	90
Max Inverter voltage	35	35	35	105
One Zero Inverter Voltage	40	0	40	80

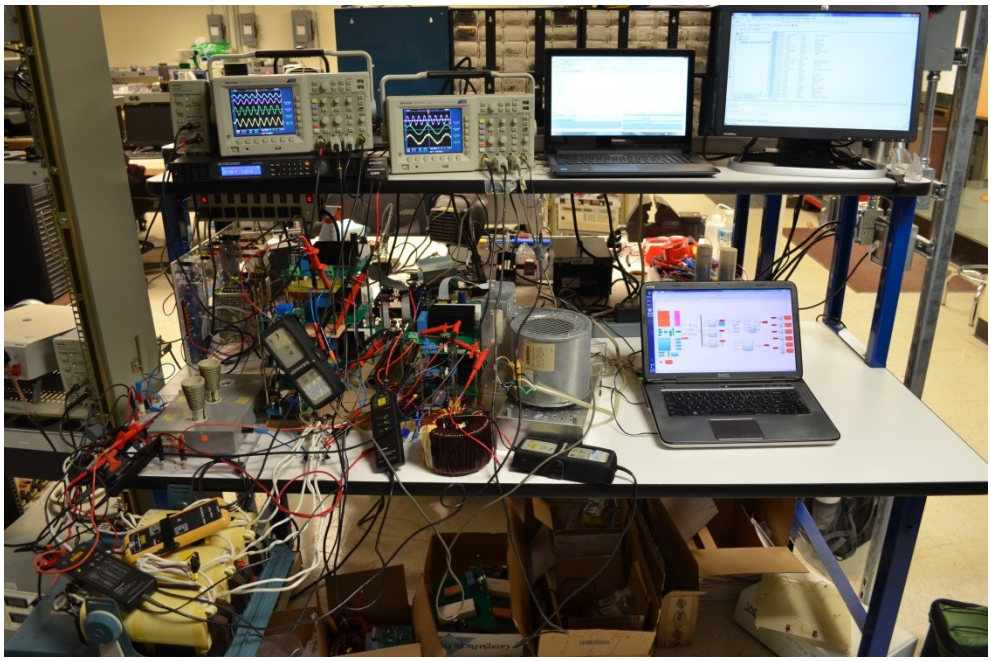

Figure 4–2. Actual PV farm lab complete setup

Table 4-2 summarized the different scenarios that the collection grid is operated at. It shows each inverter commanded voltage during each case when it will be applied in the cases to come below. For example; during normal inverter voltage case Inv#1, Inv#2 and Inv#3 will be commanded 30V and this will result in MF grid voltage of 90V.

In all cases the DC link voltage across C_{AFER} has a constant command of 100V and the grid voltage is kept constant at 50V and the injected current is kept constant at 2.5A.

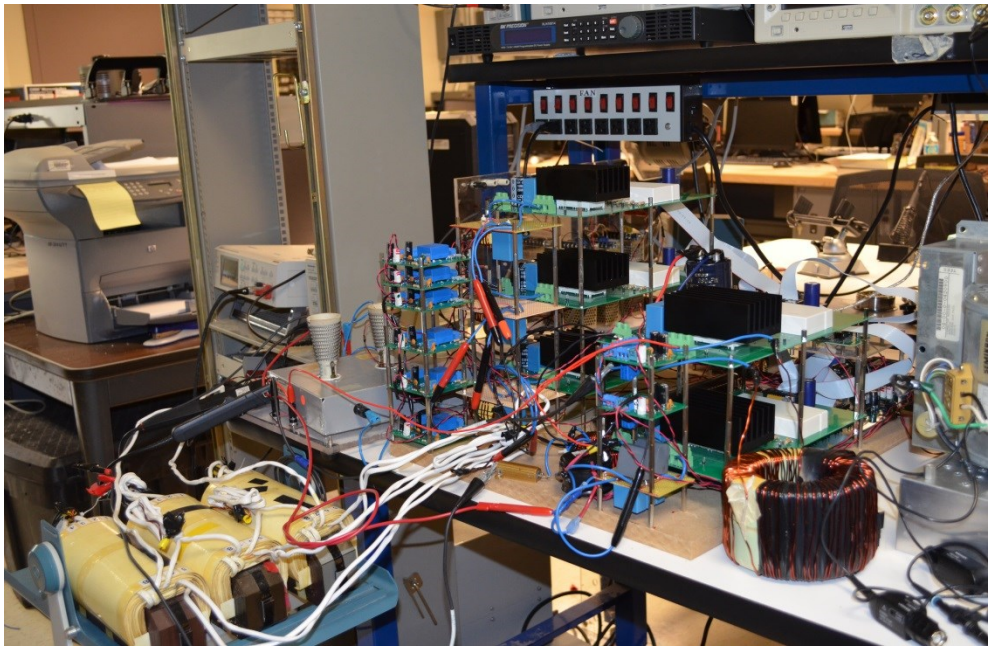

Figure 4–3. Actual PV farm setup inverters

Figure 4–2 shows the setup in the lab, two PCs are used; the first to program the DSP and the second is used for real time communication with the DSP using the CAN module. Figure 4–3 gives a closer look for the setup and shows the five inverters with their filters and all the required sensors for closed loop operation and the three transformers. .

The captured waveforms are combined in to two main categories

1. Steady state waveforms
2. Transient waveforms

4.1.1. Steady State Waveforms

This section shows the steady state waveforms for each element in the proposed architecture. The case when the minimum inverter voltage is applies is showed in Figure 4–4 and Figure 4–5. It can be noted that the MF grid voltage is not a total sinusoidal shape. The reason for that is the distortion in the inverter voltage due to the dead band effect. Due to the system complexity, an external dead band of 1uS is implemented on the inverters operation using the gate drive circuit itself and at low modulation index the effect of distortion can be noted. However, all the three inverter voltage are in phase and successfully managed to build the MF grid voltage. The AFER works perfectly and controls the MF grid current to be in phase with its voltage while maintaining a constant DC link of 100V. The grid connected inverter injects the final current in the phase with the grid voltage as shown in Figure 4–5.

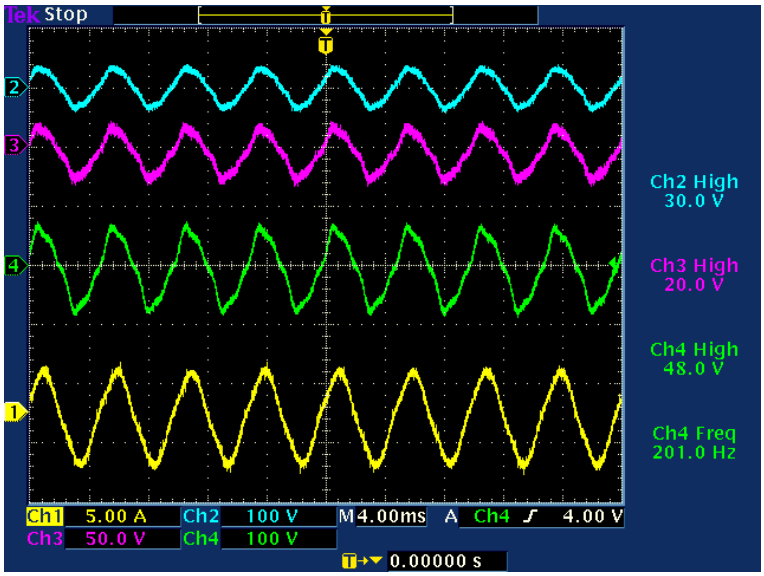

– Inv1 V [V]

– Inv 2 V [V]

– MF grid V [V]

– MF grid I[A]

Figure 4–4. Steady state time domain waveforms for min inverter voltage cases scope 1

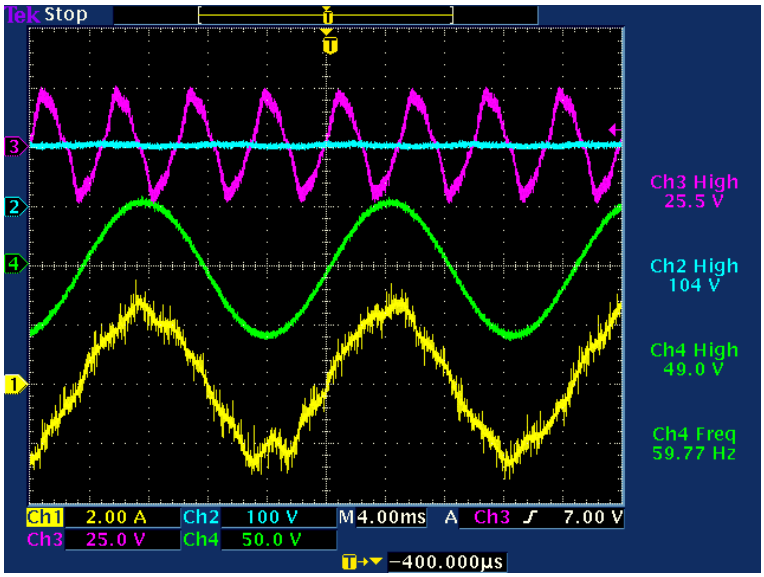

Figure 4–5. Steady state time domain waveforms for min inverter voltage cases scope 2

Figure 4–6 and Figure 4–7 shows the case when the normal voltage cases are imposed on the structure. It can be noted that the whole grid architecture performs as expected. All the PV inverter grid voltages produce synchronized voltages that are summed together to build the MF grid and the collected power is injected to the utility grid. The maximum inverter voltage case is presented in Figure 4–8 and in Figure 4–9.

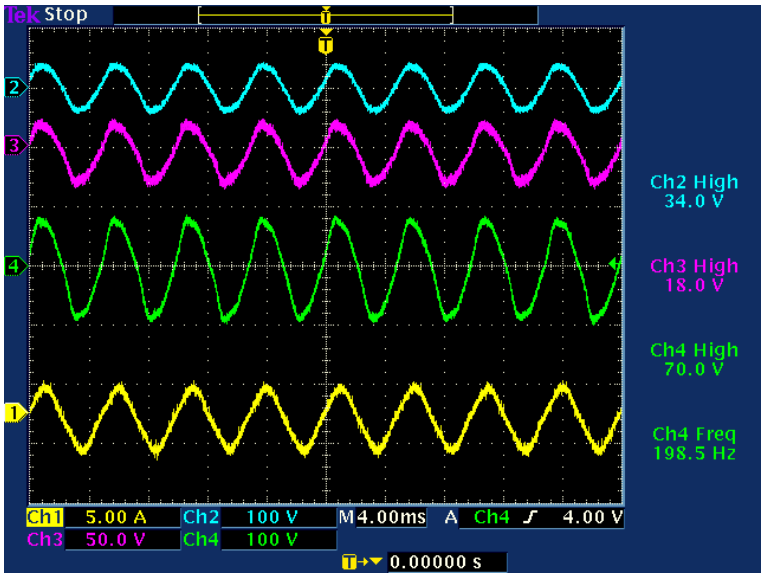

– Inv1 V [V]

– Inv 2 V [V]

– MF grid V [V]

– MF grid I[A]

Figure 4–6. Steady state time domain waveforms for normal inverter voltage cases scope 1

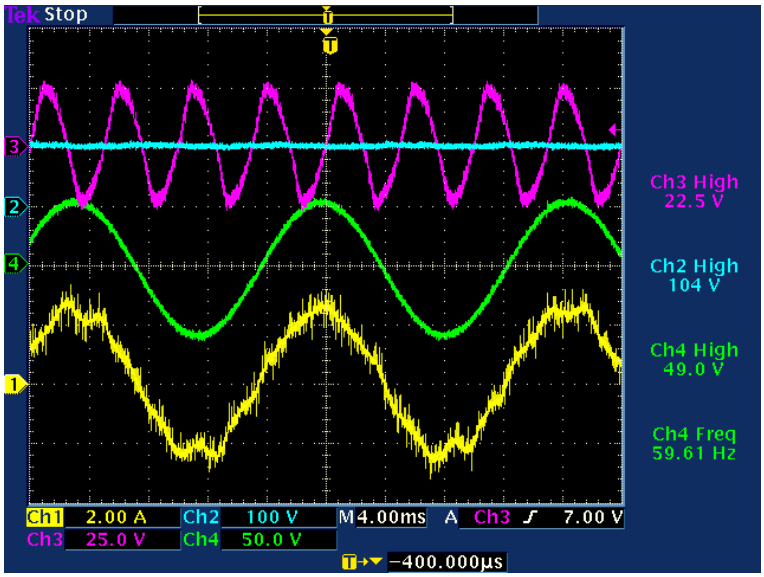

– AFER V_{dc} [V]

– I_{inv} 3 V[V]

– Grid V [V]

– Grid I [A]

Figure 4–7. Steady state time domain waveforms for normal inverter voltage cases scope 2

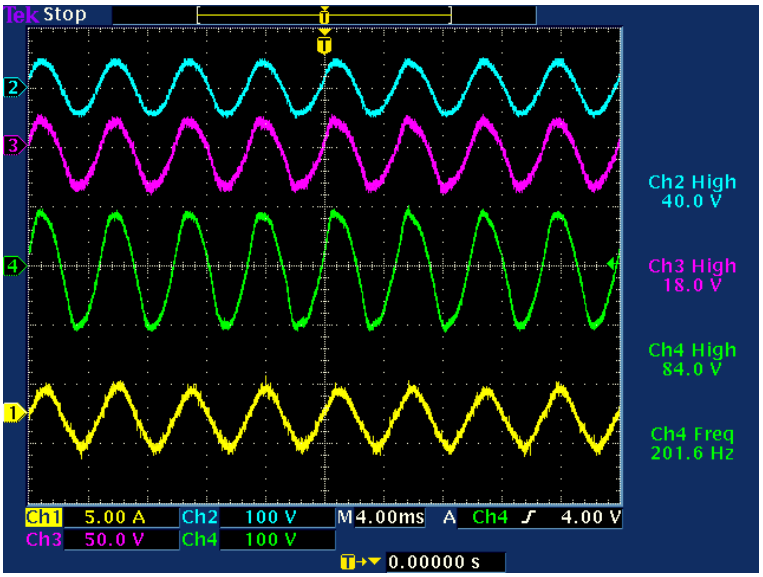

Figure 4–8. Steady state time domain waveforms for maximum inverter voltage cases scope 1

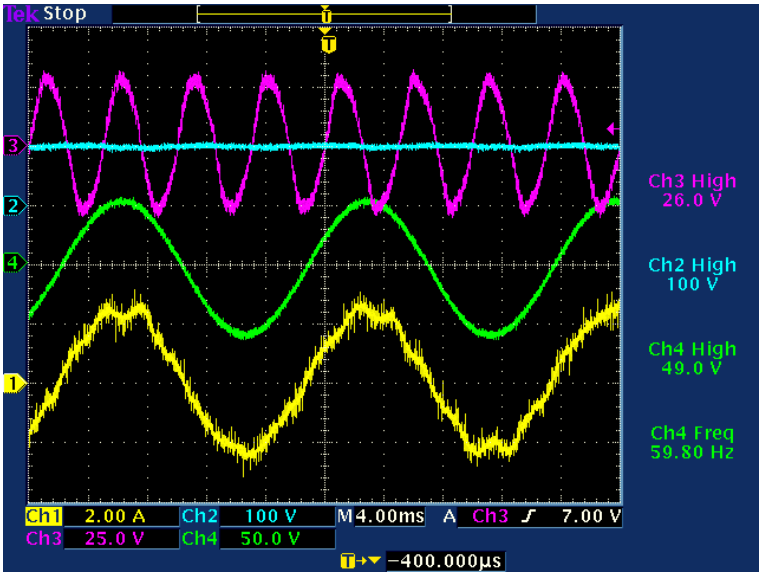

Figure 4–9. Steady state time domain waveforms for maximum inverter voltage cases scope 2

Figure 4–10 and Figure 4–11 show the structure waveforms in case of one faulty inverter and the other two contribute together to supply its share. It can be noted that structure maintains its full functionality with zero effect on the rest of the system elements.

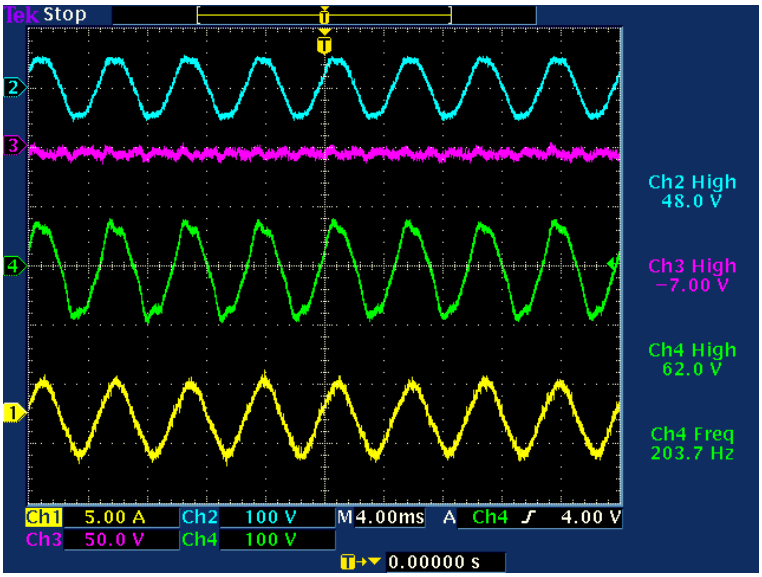

Figure 4–10. Steady state time domain waveforms for zero inverter voltage cases scope 1

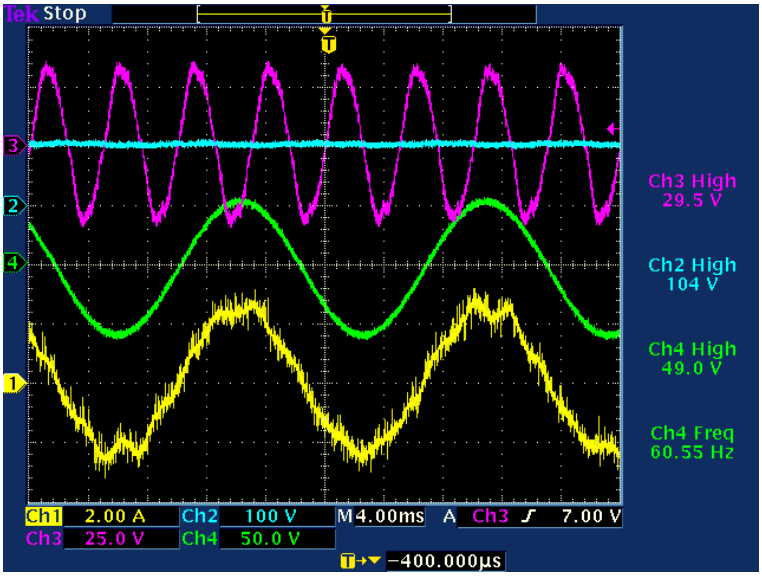

Figure 4–11. Steady state time domain waveforms for zero inverter voltage cases scope 2

4.1.2. Transient Waveforms

The transient periods between the previously mentioned inverter cases are captured and presented in this section. The transient from minimum inverter voltages to maximum inverter voltages are shown in Figure 4–12 and Figure 4–13. When the

inverter voltage commands change to their new states, it can be seen that the inverters perform as expected to the new higher values and increase the MF grid voltage to a higher voltage value hence decrease the MF grid current to a lower value because the injected current to the grid remained unchanged (i.e. constant power). The intermediate AFER voltage remains constant during the operation that indicates the controller robustness.

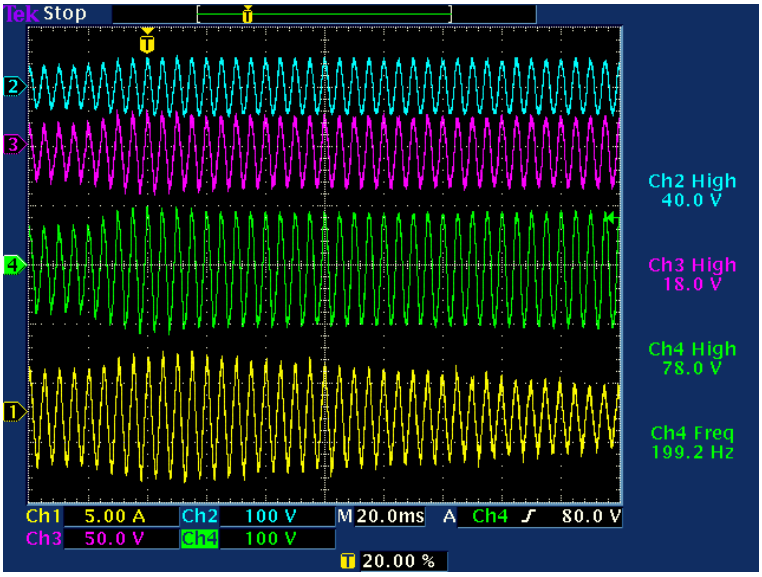

Figure 4–12. Minimum to maximum inverter voltage cased transient time domain waveforms scope 1

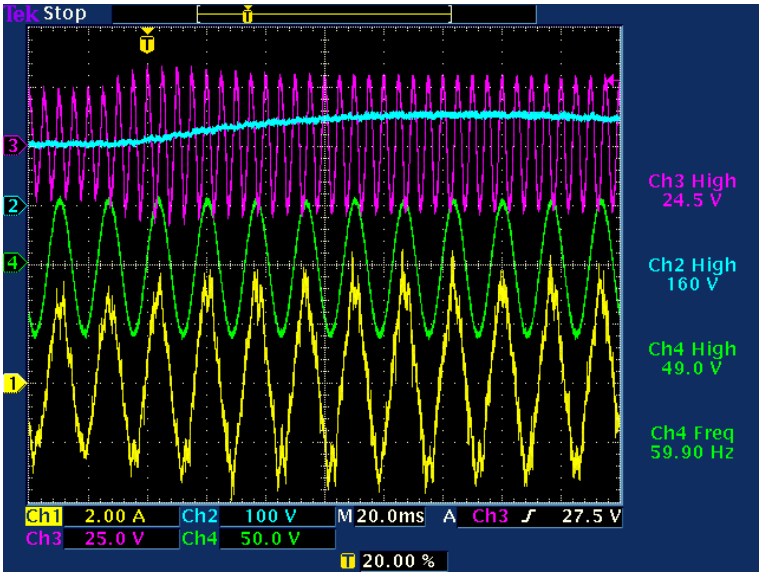

Figure 4–13. Minimum to maximum inverter voltage cased transient time domain waveforms scope 2

The change form minimum inverter voltages to zero inverter voltages case and vice versa are summarized in Figure 4–14, Figure 4–15 and in Figure 4–16, Figure 4–17 respectively. As can be seen, the proposed system controller shows extreme robustness within all the changes and maintains the whole structure operation without any loss of power. The generated PV voltages are synchronized; MF grid voltage and current are in phase. The injected grid current is at unity power factor.

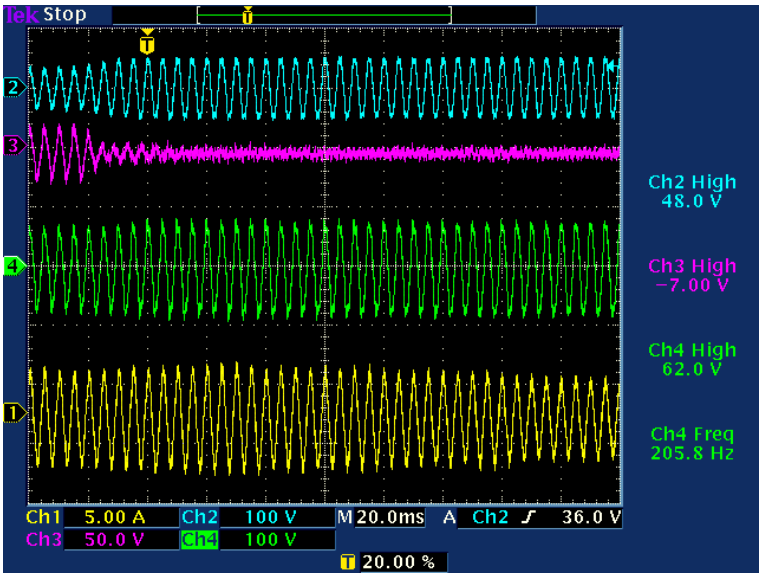

Figure 4–14. Minimum to zero inverter voltage cased transient time domain waveforms scope 1

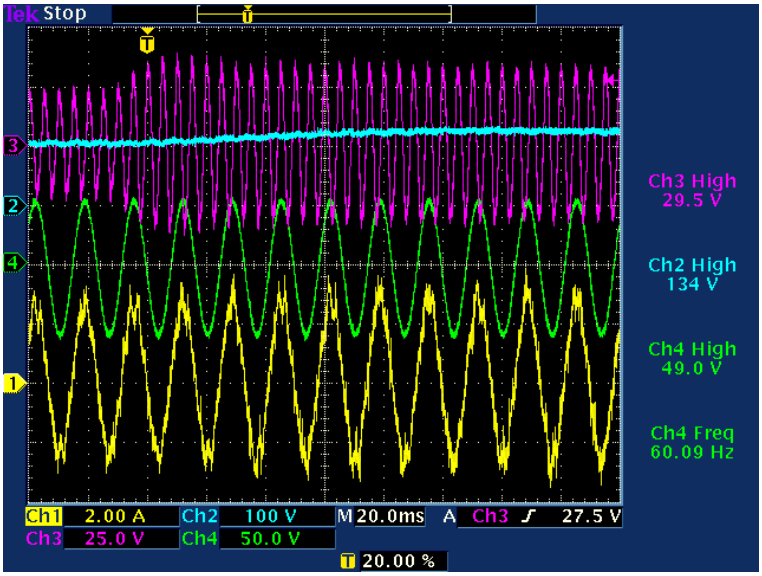

Figure 4–15. Minimum to zero inverter voltage cased transient time domain waveforms scope 2

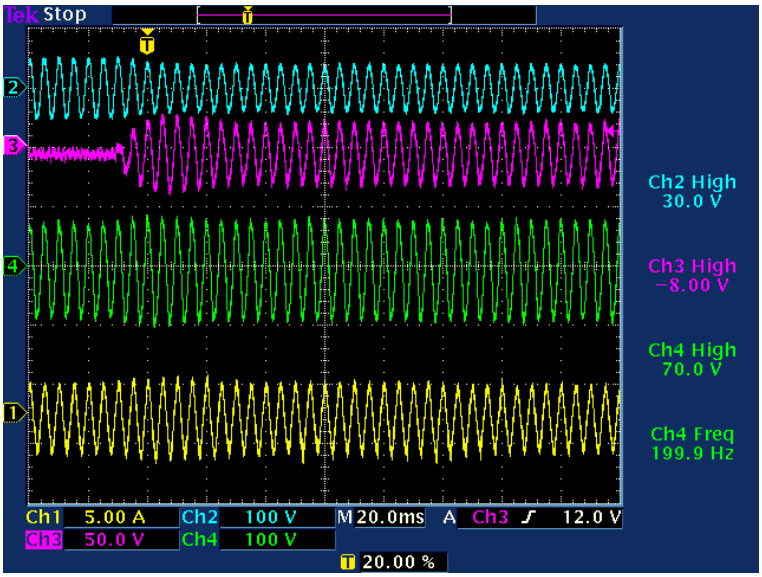

– Inv1 V [V]

– Inv 2 V [V]

– MF grid V [V]

– MF grid I[A]

Figure 4–16. Zero to normal inverter voltage cased transient time domain waveforms scope 1

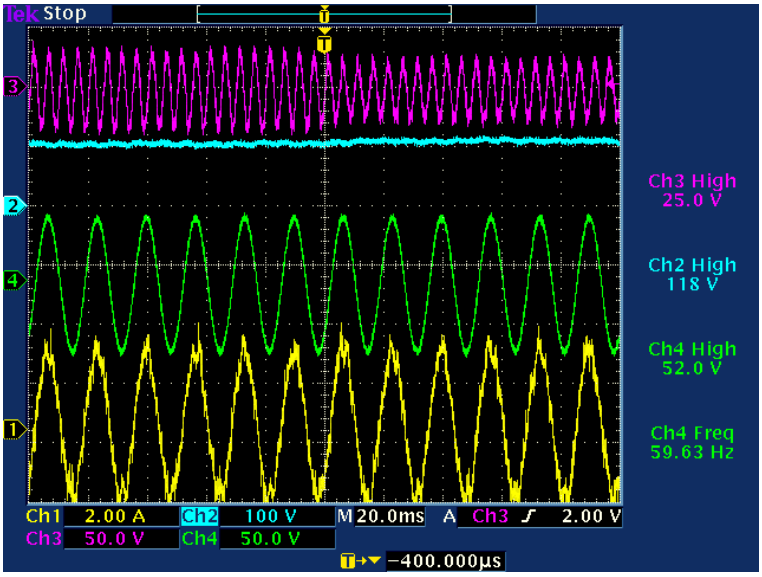

– AFER V_{dc} [V]

– I_{inv} 3 V[V]

– Grid V [V]

– Grid I [A]

Figure 4–17. Zero to normal inverter voltage cased transient time domain waveforms scope 2

4.2. Data Center

The lab setup arrangement for the proposed data center structure is shown in Figure 4–18. The system comprises three single phase transformers and their outputs are connected to a standard 250 Watts Murata PFC (MVAC400-48AFD). Each transformer primary side is connected to an AC to AC converter to modulate input grid voltage by the square wave medium frequency voltage as discussed before. Figure 4–19 shows the setup arrangement that is built in the lab. The waveforms were captured once with resistive load connected to the transformer terminals and the second with the mentioned boost PFC module. The frequency of the modulated square wave is set to be 1 kHz.

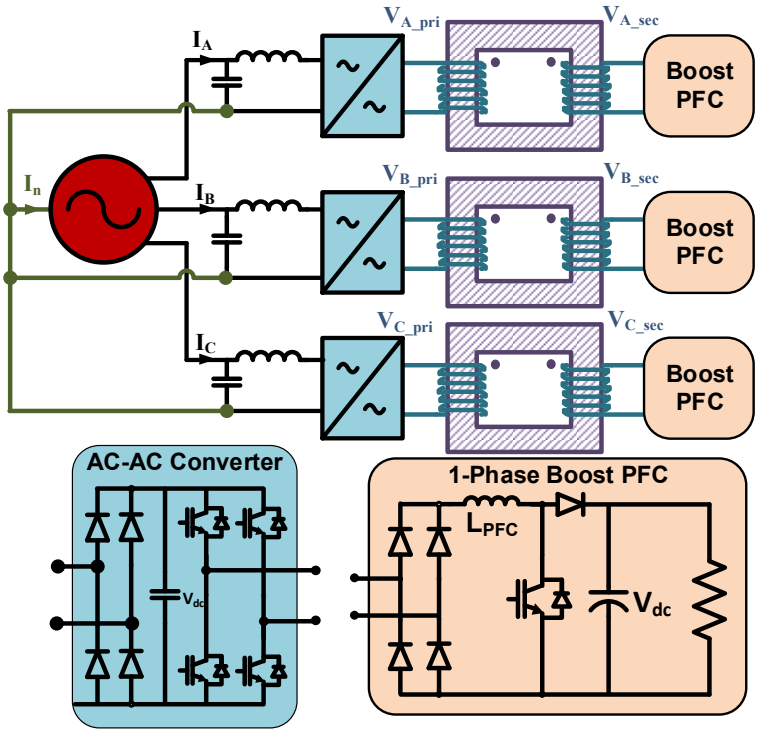

Figure 4–18. Data center lab setup arrangement

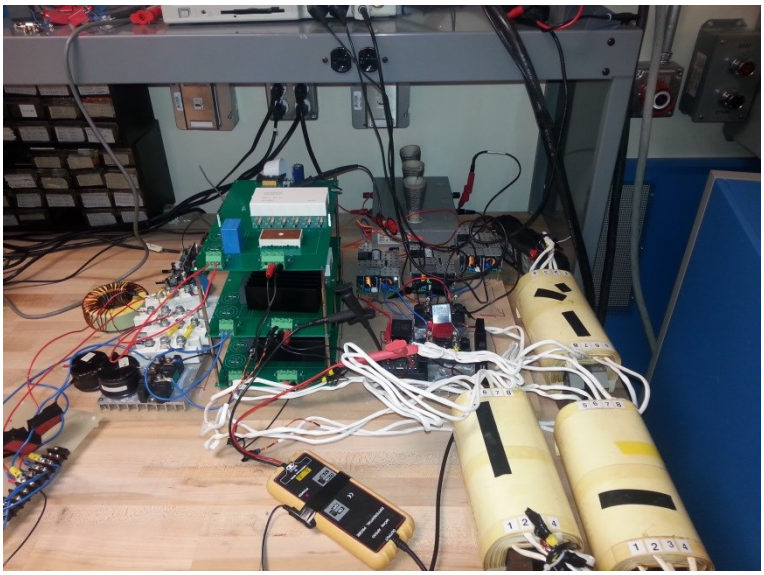

Figure 4–19. Data center actual lab setup

4.2.1. Data Center with Resistive Load

The input voltage is set to be 50V peak. The load resistance set to be 12Ω and the supply current will be almost 4A. Figure 4–20 and Figure 4–21 show the input voltage and current, neutral current, three transformer secondary voltages and phase A transformer secondary current. It can be noted that the transformers secondary voltages take the expected forms. The neutral current is shown to have almost zero average and some notches. Tracing back these notches and comparing it to the phases of the grid voltage, i.e. the envelope of the modulated MF voltages, it can be noted that every notch takes place whenever a zero crossing occurs. The voltage on one phase is small that barely able to turn the diode on, in the input diode rectifier, and this input voltage is wasted as a drop on the switches. As the result the three phases will not be balanced on during these moments that cause this notch in the neutral current. These notches did not appear in the FEA simulation because ideal switches were used there.

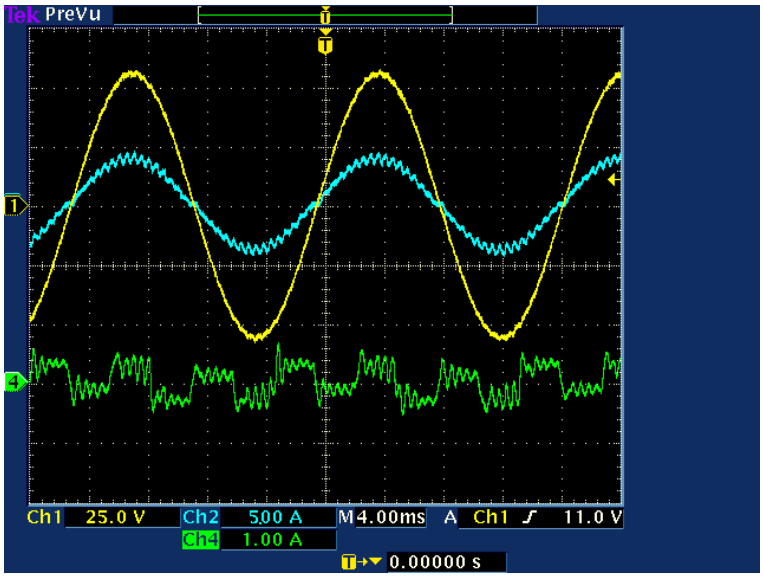

Figure 4–20. Steady state time domain waveforms for data center with identical dead band resistive load scope 1

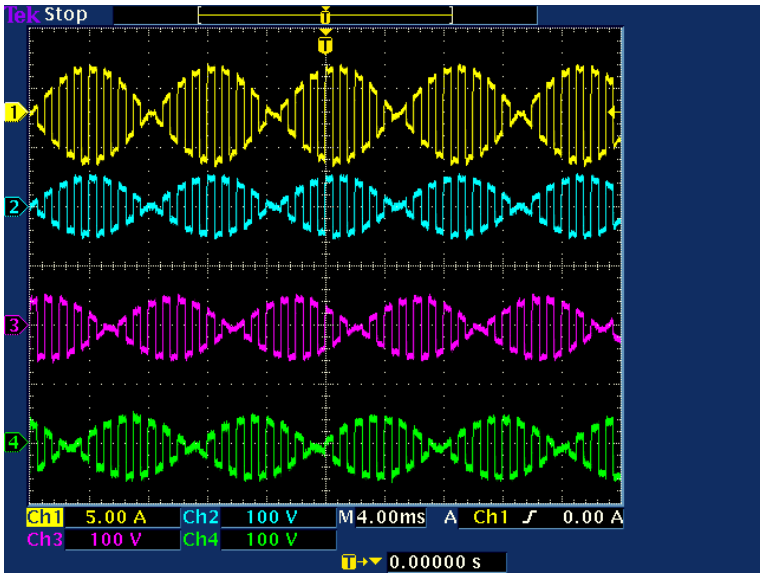

Figure 4–21. Steady state time domain waveforms for data center with identical dead band resistive load scope 2

Different dead bands were imposed on the H-bridge part of the input AC-AC converters where it was 1uS for phase A inverter, 2uS for phase B inverter, 4 uS for phase C inverter. The waveforms for the system are shown in Figure 4–22and Figure 4–23. It can be seen that the neutral current has a minimal change from the previous case.

This shows the immunity for the transformer structure for unbalanced operation due to real time switching.

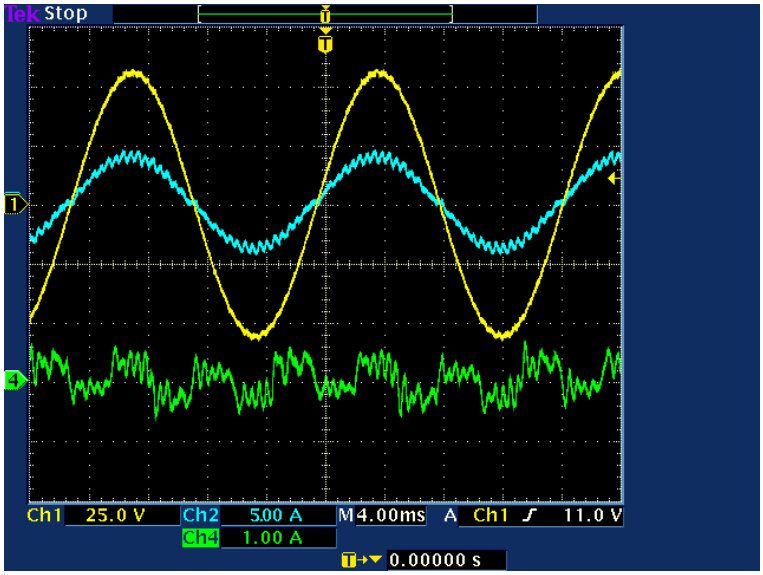

Figure 4–22. Steady state time domain waveforms for data center with different dead band resistive load scope 1

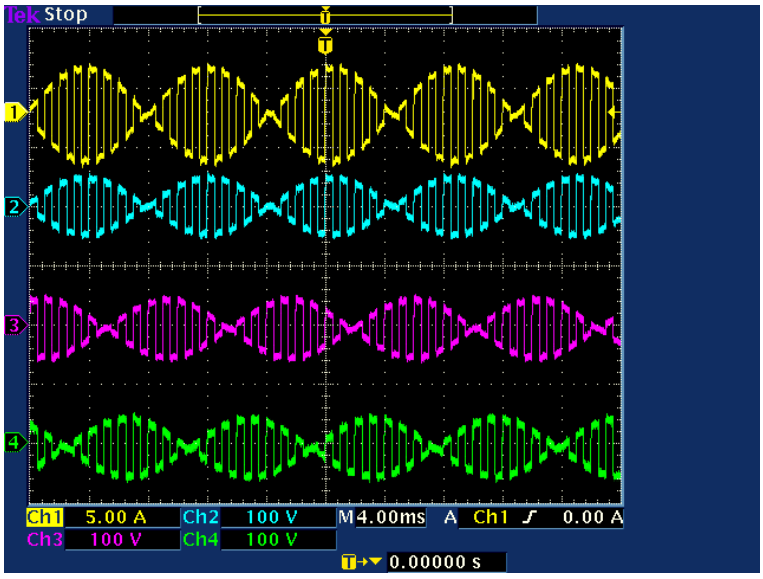

Figure 4–23. Steady state time domain waveforms for data center with different dead band resistive load scope 2

4.2.2. Data Center with Boost PFC Load

A three boost PFCs are connected to the output of three single phases' transformers. The inverters are set to have identical dead bands of 1uS of the three of them. Complete waveforms from the system are shown in Figure 4–24 and in Figure 4–25. It can be noted that the transformer secondary voltage waveforms are of the expected shape. The PFC output voltage is kept constant at 50V. It can be noted that the phase A input current suffers from a distortion during the zero crossing which is the responsibility of the boost PFC controller and this distortion will cause unbalanced load seen by the three phases that will result in the third and zero sequence neutral current as shown which can't be attenuated by the transformer structure.

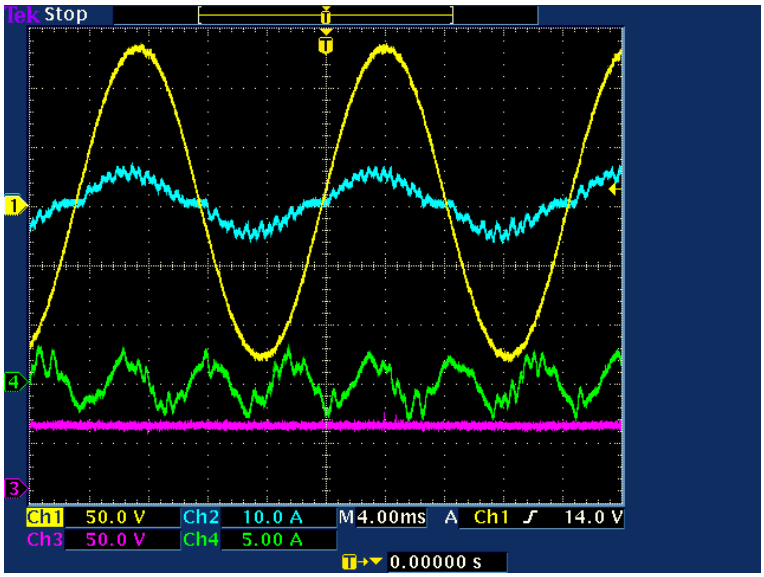

Figure 4–24. Steady state time domain waveforms for data center with identical dead band boost PFC load scope 1

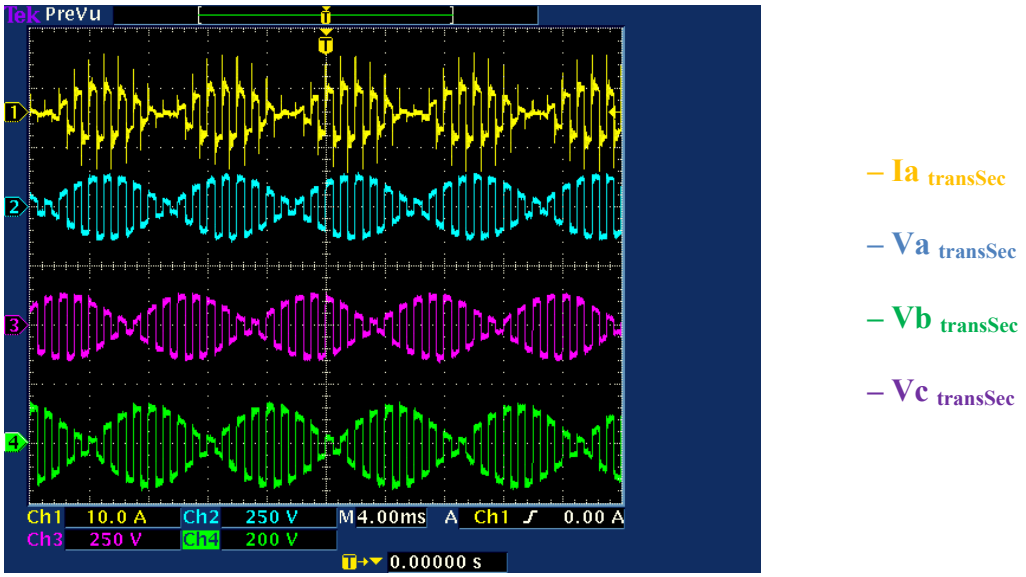

Figure 4–25. Steady state time domain waveforms for data center with identical dead band boost PFC load scope 2

Figure 4–26 and Figure 4–27 shows the system performance when different dead band is set on each inverter phase. 1uS for phase A, 2uS for phase B and 4uS for phase C. it can be noted that the system will maintain its performance as in the previous case and the neutral current will remain unchanged which means that changing the dead band had zero effect on it. However, it still suffers from the third and zero sequence components due to unbalanced loading those results from the weak performance of the PFC controller at zero crossing.

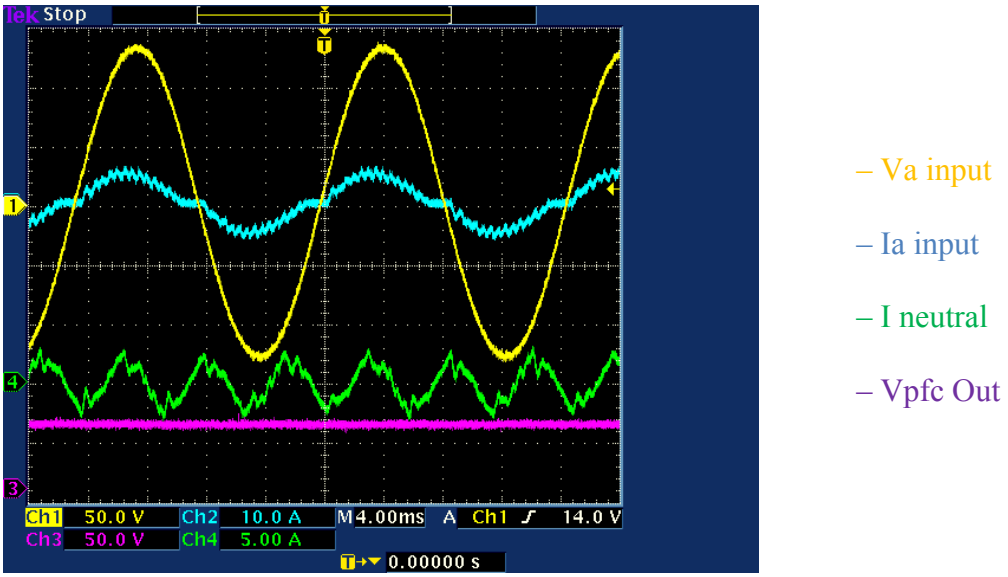

Figure 4–26. Steady state time domain waveforms for data center with different dead band boost PFC load scope 1

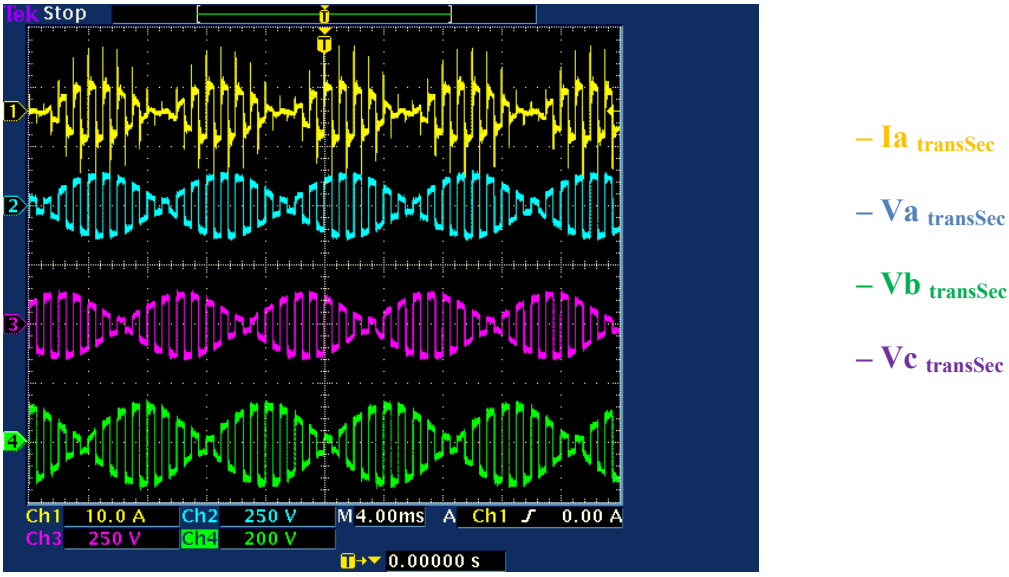

Figure 4–27. Steady state time domain waveforms for data center with different dead band boost PFC load scope 2

4.3. Summary

This section presents the experimental results for the proposed PV farm and data center architectures. It starts with the PV farm results; the shown system waveform verifies the proposal applicability. A detailed steady state results for different inverter voltages are shown combined with the transient voltage during the switch between these voltage cases. These different operating scenarios test the proposed controller performance and it shows superior robustness with no loss of power during any transient period.

The second section shows the results for the data center and it proves the proposed concept. The system shows immunity for harmonics that results from real world switching however, it can't resist the harmonics that is resulted from unbalanced loads.

5. SUMMARY

5.1. Conclusion

This dissertation introduced two new architectures for utility scale PV farms and data centers power supplies. The proposed architectures utilize wide band gaps power electronics devices in combination with MF transformer concepts to build high density power architectures.

The proposed utility scale PV farm structure provides a modular architecture for PV farms along with a customized control strategy for the proposal. The proposed structure increase the overall efficiency by 2% while reducing the system cost due to use of lower size passive elements and reduction in transformer size by one quarter. The system installation time is expected to be shorter because of the reduction in the elements and the requirement for fewer infrastructures to withstand the element sizes.

The data center structure decrease the size of the transformer by one quarter due to medium frequency operation hence increase the system power density. That section of the thesis provides an extensive comparison between three limbs and five limbs transformer designs and proved that the five limbs designs is a must for these type of structures.

This dissertation provided complete experimental results for the two proposed system to validate both of them along with their controllers. These experimental results reveal some practical challenges that were investigated and addressed.

5.2. Future Work

The work presented in this dissertation has several benefits regarding increasing the system efficiency, decreasing the system cost and elements size and several research opportunities can be further investigated

1. For Utility scale PV farm
    a. An economical and efficiency optimization study that includes all the system parameters such cable size, cable length, transformer size, transformer turns ratio, MF frequency operating voltage, MF operating frequency to select the most optimum parameters for the PV structure.
    b. The efficiency of the PV farm during different operating condition should be investigated to verify the controller tracking maximum efficiency ability. If needed, the controller can consider the operating efficiency when deciding the PV inverter voltage commands.
2. For Data Center
    a. The medium transformer could be optimized to have lower leakage inductance value. This will improve the system current quality.
    b. The input diode rectifier bridge could be replaced by an H-bridge and an implementation of four step switching algorithm could be implemented this may improve the system current quality.

REFERENCES

[1] J. D. Glover, M. Sarma, and T. Overbye, *Power System Analysis & Design, SI Version*: Cengage Learning, 2011.

[2] G. G. R. Kathleen O'Brien, ,. (March 8, 2011), Solar Grid Integration Industrial Research Perspectives , Online Available: http://www.bnl.gov/energy/files/nserc/GE_Global_Research_Solar_Grid_Integration.pdf

[3] M. H. Rashid, *Power electronics handbook: devices, circuits and applications*: Academic Press, 2010.

[4] P. Roussel, "SiC market and industry update," in *Int. SiC Power Electron. Appl. Workshop, Kista, Sweden*, 2011.

[5] B. Zhao, Q. Song, and W. Liu, "Experimental Comparison of Isolated Bidirectional DC–DC Converters Based on All-Si and All-SiC Power Devices for Next-Generation Power Conversion Application," *Industrial Electronics, IEEE Transactions on,* vol. 61, pp. 1389-1393, 2014.

[6] C. Sintamarean, E. Eni, F. Blaabjerg, R. Teodorescu, and H. Wang, "Wide-band gap devices in PV systems-opportunities and challenges," in *Power Electronics Conference (IPEC-Hiroshima 2014-ECCE-ASIA), 2014 International*, 2014, pp. 1912-1919.

[7] J. Millan, P. Godignon, X. Perpina, A. Pérez-Tomás, and J. Rebollo, "A survey of wide bandgap power semiconductor devices," *Power Electronics, IEEE Transactions on,* vol. 29, pp. 2155-2163, 2014.

[8] R. Burkart and J. W. Kolar, "Component cost models for multi-objective optimizations of switched-mode power converters," in *Energy Conversion Congress and Exposition (ECCE), 2013 IEEE*, 2013, pp. 2139-2146.

[9] R. M. Burkart and J. W. Kolar, "Comparative evaluation of SiC and Si PV inverter systems based on power density and efficiency as indicators of initial cost and operating revenue," in *Control and Modeling for Power Electronics (COMPEL), 2013 IEEE 14th Workshop on*, 2013, pp. 1-6.

[10] D. Rana, B. Hafez, P. Garg, S. Essakiappan, and P. Enjeti, "Analysis and design of active inductor as DC-link reactor for lightweight adjustable speed drive systems," in *Energy Conversion Congress and Exposition (ECCE), 2014 IEEE*, 2014, pp. 3243-3250.

[11] W. G. Hurley, W. H. Wolfle, and J. G. Breslin, "Optimized transformer design: inclusive of high-frequency effects," *Power Electronics, IEEE Transactions on,* vol. 13, pp. 651-659, 1998.

[12] C.-k. Leung, S. Dutta, S. Baek, and S. Bhattacharya, "Design considerations of high voltage and high frequency three phase transformer for solid state transformer application," *Proc. IEEE ECCE,* pp. 1551-1558, 2010.

[13] G. Ortiz, M. Leibl, J. W. Kolar, and O. Apeldoorn, "Medium frequency transformers for solid-state-transformer applications — Design and experimental verification," in *Power Electronics and Drive Systems (PEDS), 2013 IEEE 10th International Conference on*, 2013, pp. 1285-1290.

[14] H. Qin and J. W. Kimball, "Solid-state transformer architecture using AC–AC dual-active-bridge converter," *Industrial Electronics, IEEE Transactions on,* vol. 60, pp. 3720-3730, 2013.

[15] X. She, A. Q. Huang, and R. Burgos, "Review of solid-state transformer technologies and their application in power distribution systems," *Emerging and Selected Topics in Power Electronics, IEEE Journal of,* vol. 1, pp. 186-198, 2013.

[16] C. Zhao, D. Dujic, A. Mester, J. K. Steinke, M. Weiss, S. Lewdeni-Schmid*, et al.*, "Power Electronic Traction Transformer—Medium Voltage Prototype," *Industrial Electronics, IEEE Transactions on,* vol. 61, pp. 3257-3268, 2014.

[17] W. G. Hurley and W. H. Wölfle, *Transformers and Inductors for Power Electronics: Theory, Design and Applications*: John Wiley & Sons, 2013.

[18] W. Kramer, S. Chakraborty, B. Kroposki, and H. Thomas, "Advanced power electronic interfaces for distributed energy systems," *National Renewable Energy Laboratory, Cambridge, MA Rep. NREL/Tp–581–42672,* vol. 1, 2008.

[19] S. Esterly and R. Gelman, *2013 Renewable Energy Data Book*: US Department of Energy, Energy Efficiency & Renewable Energy Laboratory, 2013.

[20] Solar Energy Industries Assocation, "Solar Market Insight Report 2013 Year in Review," 2013.

[21] S. J. Castillo, R. S. Balog, and P. Enjeti, "Predicting capacitor reliability in a module-integrated photovoltaic inverter using stress factors from an environmental usage model," in *North American Power Symposium (NAPS), 2010*, 2010, pp. 1-6.

[22] A. Darwish, A. S. Abdel-Khalik, A. Elserougi, S. Ahmed, and A. Massoud, "Fault current contribution scenarios for grid-connected voltage source inverter-based distributed generation with an LCL filter," *Electric Power Systems Research,* vol. 104, pp. 93-103, 11// 2013.

[23] Danfoss Solar. (June 2012), Optimized system layout , Online Available: http://www.danfoss.com/NR/rdonlyres/6507E2ED-D210-422C-976B-6E8DC943B65D/0/DKSIPM204A102_Eggebek_TechCaseStudy_WEB.pdf

[24] J. M. Carrasco, L. G. Franquelo, J. T. Bialasiewicz, E. Galvan, R. C. P. Guisado, M. A. M. Prats*, et al.*, "Power-Electronic Systems for the Grid Integration of Renewable Energy Sources: A Survey," *Industrial Electronics, IEEE Transactions on,* vol. 53, pp. 1002-1016, 2006.

[25] H. S. Krishnamoorthy, S. Essakiappan, P. N. Enjeti, R. S. Balog, and S. Ahmed, "A new multilevel converter for Megawatt scale solar photovoltaic utility integration," in *Applied Power Electronics Conference and Exposition (APEC), 2012 Twenty-Seventh Annual IEEE*, 2012, pp. 1431-1438.

[26] G. G. R. Ahmed Elasser, ,. (October 7th, 2010), Photovoltaics Systems: Overview, Status, and Future Prospects , Online Available: http://www.ecse.rpi.edu/homepages/ieee/presentations/Fall_2010/IEEE_RPI_Oct7th_PV_Systems_Seminar_2010.pdf

[27] A. K. Abdelsalam, A. M. Massoud, S. Ahmed, and P. Enjeti, "High-Performance Adaptive Perturb and Observe MPPT Technique for Photovoltaic-Based Microgrids," *Power Electronics, IEEE Transactions on,* vol. 26, pp. 1010-1021, 2011.

[28] J. A. Villarejo, A. Molina-Garcia, and E. De Jodar, "Comparison of central vs distributed inverters: application to photovoltaic systems," in *Industrial Electronics (ISIE), 2011 IEEE International Symposium on*, 2011, pp. 1741-1746.

[29] J. Koomey, "Growth in data center electricity use 2005 to 2010," *Oakland, CA: Analytics Press. August,* vol. 1, p. 2010, 2011.

[30] Emerson. (2011), State of the Data Center 2011 , Online Available: http://www.emersonnetworkpower.com/en-US/Solutions/infographics/Pages/2011DataCenterState.aspx

[31] IBM Corporation. (April 21, 2010), Energy Efficient IT.

[32] B. Carmichael. (May 2008), Data centers set to outpace airlines in GHG emissions *Onearth magazine [Online]*. Available: http://www.onearth.org/blog/whats-happening-on-earth/data-centers-set-to-outpace-airlines-in-ghg-emissions

[33] Gartner Executive Programs (EXP). (2009), Gartner EXP 2009 CIO Survey , Online Available: http://www.gartner.com/newsroom/id/855612

[34] Z. Moradi-Shahrbabak, A. Tabesh, and G. R. Yousefi, "Economical design of utility-scale photovoltaic power plants with optimum availability," *Industrial Electronics, IEEE Transactions on,* vol. 61, pp. 3399-3406, 2014.

[35] M. Meinhardt, G. Cramer, B. Burger, and P. Zacharias, "Multi-string-converter with reduced specific costs and enhanced functionality," *Solar Energy,* vol. 69, pp. 217-227, 2001.

[36] T. Kerekes, *Analysis and modeling of transformerless photovoltaic inverter systems*: Videnbasen for Aalborg UniversitetVBN, Aalborg UniversitetAalborg University, Det Teknisk-Naturvidenskabelige FakultetThe Faculty of Engineering and Science, Institut for EnergiteknikDepartment of Energy Technology, 2009.

[37] R. Pena-Alzola, G. Gohil, L. Mathe, M. Liserre, and F. Blaabjerg, "Review of modular power converters solutions for smart transformer in distribution system," in *Energy Conversion Congress and Exposition (ECCE), 2013 IEEE*, 2013, pp. 380-387.

[38] X. Li, X. Ai, and Y. Wang, "Study of single-phase HFAC microgrid based on Matlab/Simulink," in *Electric Utility Deregulation and Restructuring and Power Technologies (DRPT), 2011 4th International Conference on*, 2011, pp. 1104-1108.

[39] S. Gierschner, H.-G. Eckel, and M.-M. Bakran, "A competitive medium frequency AC distribution grid for offshore wind farms using HVDC," in *Power Electronics and Applications (EPE), 2013 15th European Conference on*, 2013, pp. 1-10.

[40] S. Chakraborty and M. G. Simoes, "Experimental Evaluation of Active Filtering in a Single-Phase High-Frequency AC Microgrid," *Energy Conversion, IEEE Transactions on,* vol. 24, pp. 673-682, 2009.

[41] Wikipedia, "Eggebek Solar Park," ed. Online, 2015.

[42] K. H. Ahmed, S. J. Finney, and B. W. Williams, "Passive Filter Design for Three-Phase Inverter Interfacing in Distributed Generation," in *Compatibility in Power Electronics, 2007. CPE '07*, 2007, pp. 1-9.

[43] C. Hsin-Ju, G. L. Kusic, and G. F. Reed, "Comparative PSCAD and Matlab/Simulink simulation models of power losses for SiC MOSFET and Si IGBT devices," in *Power and Energy Conference at Illinois (PECI), 2012 IEEE*, 2012, pp. 1-5.

[44] Cree. "C2M0080120D Silicon Carbide Power MOSFET Z-FET TM MOSFET" [Online]. Available: http://www.cree.com/Power/Products/MOSFETs/TO247/C2M0080120D

[45] I. Metglas®, ,. (April 29, 2011), Amorphous Alloys for Transformer Cores , Online Available: http://www.metglas.com/assets/pdf/2605sa1.pdf

[46] G. F. Moore, *Electric cables handbook*: Blackwell publishing, 1997.

[47] Elsewedy Electric. (2012), Power Cables, Online Available: http://www.elsewedyelectric.com/Catalogs/Power%20Cables.pdf

[48] Infineon Technologies Bipolar GmbH& Co. KG, "Technical Information Bipolar semiconductors," 2012.

[49] L. Gyugyi and B. R. Pelly, *Static power frequency changers: theory, performance, and application*: Wiley New York, 1976.

[50] A. Ishiguro, T. Furuhashi, and S. Okuma, "A novel control method for forced commutated cycloconverters using instantaneous values of input line-to-line

voltages," *Industrial Electronics, IEEE Transactions on,* vol. 38, pp. 166-172, 1991.

[51] J. Irwin, M. P. Kazmierkowski, R. Krishnan, and F. Blaabjerg, *Control in power electronics: selected problems*: Academic press, 2002.

[52] H. Akagi, E. H. Watanabe, and M. Aredes, *Instantaneous power theory and applications to power conditioning* vol. 31: John Wiley & Sons, 2007.

[53] P. T. Krein, "A discussion of data center power challenges across the system," in *Energy Aware Computing (ICEAC), 2010 International Conference on*, 2010, pp. 1-3.

[54] J. Mitchell-Jackson, J. G. Koomey, B. Nordman, and M. Blazek, "Data center power requirements: measurements from Silicon Valley," *Energy,* vol. 28, pp. 837-850, 6// 2003.

[55] T. Soeiro, T. Friedli, and J. W. Kolar, "Three-phase high power factor mains interface concepts for Electric Vehicle battery charging systems," in *Twenty-Seventh Annual IEEE Applied Power Electronics Conference and Exposition (APEC)*, 2012, pp. 2603-2610.

[56] G. Spiazzi and F. C. Lee, "Implementation of single-phase boost power-factor-correction circuits in three-phase applications," *Industrial Electronics, IEEE Transactions on,* vol. 44, pp. 365-371, 1997.

[57] P. Drabek, Z. Peroutka, M. Pittermann, Ce, x, and M. dl, "New Configuration of Traction Converter With Medium-Frequency Transformer Using Matrix Converters," *Industrial Electronics, IEEE Transactions on,* vol. 58, pp. 5041-5048, 2011.

[58] P. Barbosa, F. Canales, and F. C. Lee, "A front-end distributed power system for high-power applications," in *Industry Applications Conference, 2000. Conference Record of the 2000 IEEE*, 2000, pp. 2546-2551 vol.4.

[59] C. Yong-Won, K. Jung-Min, and K. Bong-Hwan, "Single Power-Conversion AC--DC Converter With High Power Factor and High Efficiency," *Power Electronics, IEEE Transactions on,* vol. 29, pp. 4797-4806, 2014.

[60] M. Mosman. (September 2012), Medium Voltage Electrical Systems for Data Centers [Online]. Available:

http://www.ccgfacilities.com/pdf/MEDIUM%20VOLTAGE%20ELECTRICAL%20SYSTEMS%20FOR%20DATA%20CENTERS.pdf

[61] A. T. Russell and E. M. A. Oliveira, "Sine Amplitude Converters for efficient datacenter power distribution," in *Renewable Energy Research and Applications (ICRERA), 2012 International Conference on*, 2012, pp. 1-6.

[62] M. Wiboonrat, "Next Generation Data Center design under Smart Grid," in *Ubiquitous and Future Networks (ICUFN), 2012 Fourth International Conference on*, 2012, pp. 103-108.

[63] SchneiderElectric. (April 2011), Data Center Product Application Guide [Online]. Available: http://download.schneider-electric.com/files?p_File_Id=159293837&p_File_Name=0100SM0501.pdf

[64] H. S. Krishnamoorthy, D. Rana, and P. N. Enjeti, "A new wind turbine generator / battery energy storage utility interface converter topology with medium-frequency transformer," in *Applied Power Electronics Conference and Exposition (APEC), 2013 Twenty-Eighth Annual IEEE*, 2013, pp. 2218-2224.

[65] infineon. (2013), FF450R12IE4 [Online]. Available: http://www.infineon.com/dgdl/ds_ff450r12ie4_2_4_de-en.pdf?folderId=db3a304412b407950112b4095b0601e3&fileId=db3a30431f848401011feb871c423ea4

[66] infineon. (2013), FF100R12YT3 [Online]. Available: http://www.infineon.com/dgdl/ds_ff100r12yt3_2_1_de-en.pdf?folderId=db3a304412b407950112b408e8c90004&fileId=db3a304412b407950112b43470386031

[67] V. Semiconductors. (2013), 240U(R).. Series [Online]. Available: http://www.vishay.com/docs/93504/240urseries.pdf

[68] V. Semiconductors. (2008), SD403C..C Series [Online]. Available: http://www.vishay.com/docs/93175/sd403cc.pdf

[69] infineon. (2009), IGW75N60T [Online]. Available: http://www.infineon.com/dgdl/IGW75N60T_Rev2_5G.pdf?folderId=db3a304412b407950112b408e8c90004&fileId=db3a304412b407950112b42817e13d60

[70] I. Villar, L. Mir, I. Etxeberria-Otadui, J. Colmenero, X. Agirre, and T. Nieva, "Optimal design and experimental validation of a Medium-Frequency 400kVA power transformer for railway traction applications," in *Energy Conversion Congress and Exposition (ECCE), 2012 IEEE*, 2012, pp. 684-690.

[71] N. Mohan, *First Course on Power Electronics*: MNPERE, Minnesota Power Electronics Research & Education, 2009.

[72] T. Instruments. (2012), TMS320F28335, TMS320F28334, TMS320F28332, TMS320F28235, TMS320F28234, TMS320F28232 Digital Signal Controllers (DSCs) Data Manual [Online]. Available: http://www.ti.com/lit/ds/symlink/tms320f28335.pdf

[73] MathWorks(accessed on May 31,2015). Embedded Coder Generate C and C++ code optimized for embedded systems [Online]. Available: http://www.mathworks.com/products/embedded-coder/

[74] Semikron. (2006), SK13GD063 [Online]. Available: http://shop.semikron.com/out/media/ds/SEMIKRON_DataSheet_SK_13_GD_063_24508201.pdf

[75] Semikron. (2007), SKHI 61 (R) [Online]. Available: http://shop.semikron.com/out/media/ds/SEMIKRON_DataSheet_SKHI_61_R_L6100061.pdf

[76] Intrepidcs(accessed on May 31,2015). ValueCAN3 [Online]. Available: http://store.intrepidcs.com/ValueCAN3-DW-2-Channel-p/vcan-dw3.htm

[77] R. Labaki, B. Kedjar, and K. Al-Haddad, "Single-Phase Active Front End Converter with series compensation," in *Industrial Electronics, 2006 IEEE International Symposium on*, 2006, pp. 769-774.

APPENDIX

Transformer design matlab code

```
clc;clear all;close all;
%% Transformer Specs/Design

folderName = 'Transformer_1MW';
VtIn = 4e3;
VtOut = 350;
Ptout = 1e6;
TransformerTurnsRatio = VtIn/VtOut;
TransformerEffectiveTurnsRatio = TransformerTurnsRatio;
ItInput = Ptout/(sqrt(3)*VtIn);
ItOut = Ptout/(sqrt(3)*VtOut);
Rout = VtOut/ItOut;
%%
% The used referances for the transformer design are
%   1- "Transformers and inductors for power electronics-theory, design and applications" by W.G. Hurley and W.H. Wolfle
%   2- "Transformer and Inductor Design Handbook" third edition. Colonel Wm. T. Mclyman
% The transformer design process is based on the flowchart in chapter five from the first refernec - page 129
effTrans = 0.98;        % Initial transformer effeciency
PFtrans = 0.98;         % Initial transformer power factor
Tamp = 30;              % ampiant temp
dT = 60;                % in degree C
Tmax = Tamp+dT;         % in degree C
hc = 10;                % coeffient of heat transfer by convention in Watts/(Kelvin/m^2)
% ka,kw,kc are three dimension less constants in page 61 - kt is in page xxiv
ka = 40;
kw = 10;
kc = 5.6;
kt = 48.2e3;
% ku = 0.0175; % Window utilization factor
ku = 0.4; % Window utilization factor - for low power 0.02
```

```
kf = 0.99; % core stacking factor (effective area/ total area)
alfa20 = 0.00393;% temp coefficient at 20 deg C for copper
Kv = 4.00;    % voltage waveform constant
transVA = (Ptout/PFtrans)*(3/effTrans);
ft = [ 0.06; 0.6; 0.8; 1; 1.2; 1.4; 1.6; 1.8; 2]*1e3; %define the design frequency
% http://www.engineersedge.com/copper_wire.htm
[num,txt,AWGInfoCell] = xlsread('AWGInfo'); % load wire sizes
AWGName = (AWGInfoCell( 2:end ,1));
AWGArea = cell2mat(AWGInfoCell( 2:end ,2))./100; % to convert to mm2 to cm2
AWGRho = cell2mat(AWGInfoCell( 2:end ,3))*1e-3; % to convert to mOhms to Ohms
mkdir(folderName);
% The materials parameters is in page 20
% select material index
% 2 > Ferrites
% 3 > Nanocrystaline
% 4 > Amorphous
% 5 > Si-Iron
% 6 > Ni-Fe - permalloy
% 7 > poweder iron
% 8 > MetglasNanoFinemet-50 Hz-TFA (COMSOL database)
% 9 > Metglas2605SA1
% 10> M125

% CoreMaterailSelected = [2,3,4,6,8,9,10];
CoreMaterailSelected = [2:8];
CoreMatLen = length(CoreMaterailSelected);
BratioMinSize = ones(length(ft),CoreMatLen);
BratioMaxEff = ones(length(ft),CoreMatLen);
TransEffMinSize = ones(length(ft),CoreMatLen);
TransEffMaxEff = ones(length(ft),CoreMatLen);
TransAPMinSize = ones(length(ft),CoreMatLen);
TransAPMaxEff = ones(length(ft),CoreMatLen);
TransLleakMinSize = ones(length(ft),CoreMatLen);
TransLleakMaxEff = ones(length(ft),CoreMatLen);
CoreNameVec = cell(1,CoreMatLen);
```

```
for cms = 1:CoreMatLen
    CoreIndex = CoreMaterailSelected(cms);
    [num1,txt1,CoreParameter] = xlsread('MagneticCoreParameter');
    CoreMaterial = cell2mat(CoreParameter(1,CoreIndex));
    CoreNameVec(CoreIndex-1) = {CoreMaterial};
    rho = cell2mat(CoreParameter(2,CoreIndex))*1e-6;    % Ohm.meter
    Kc = cell2mat(CoreParameter(3,CoreIndex));          % Materail parameter
    alfa = cell2mat(CoreParameter(4,CoreIndex));        % Materail parameter
    beta = cell2mat(CoreParameter(5,CoreIndex));        % Materail parameter
    Bpeak = cell2mat(CoreParameter(6,CoreIndex));       % Materail parameter
    muh = cell2mat(CoreParameter(7,CoreIndex));         % magentic permeability for the core

    %
    Bo = ones(length(ft),2);
    Ap = ones(length(ft),2);
    Jo = ones(length(ft),2);

    % dimension of the core/ winding
    a = ones(length(ft),2);
    b = ones(length(ft),2);
    d = ones(length(ft),2);

    % the asumption is a = b  and d = 4a
    MLT = ones(length(ft),2); % mean length of winding turns in the left and rigth limbs
    MLTmid = ones(length(ft),2); % mean length of winding turns in the middle limb
    MPL = ones(length(ft),2); % average magnetic length


    Ac  = ones(length(ft),2); % cross section are of the magnetic core
    Am = ones(length(ft),2); % effective cross section are of the magnetic core
    Vc = ones(length(ft),2);% the total volume of the core
    Vw = ones(length(ft),2);% the total volume of the winding
    Wa = ones(length(ft),2); % window winding area of the core
    Np = ones(length(ft),2); % transformer primary number of turns
    Ns = ones(length(ft),2); % transformer secondary number of turns
```

```
transWidth = ones(length(ft),2);
transHeight = ones(length(ft),2);
skinDepth = ones(length(ft),2); % skin depth [cm]
wireD =  ones(length(ft),2);    % wire Diamter  [cm]
wireA = ones(length(ft),2);    % wire Area  [cm^2]
AWGAreaSelected = ones(length(ft),2); % AWG wire size selected in [cm^2]
AWGNameSelected = cell(length(ft),2);
wireStrandsPri = ones(length(ft),2);
wireStrandsSec = ones(length(ft),2);
BpeakVec = Bpeak*ones(length(ft),2);

rhoAWGMaxT = ones(length(ft),2); % resistivity of the conductor at the Maximum  operating temp
Rpri = ones(length(ft),2);% total primary winding resistance [Ohms]
Rsec = ones(length(ft),2);% total secondary winding resistnace [Ohms]
Rcore = ones(length(ft),2); % Core resistance [Ohms]
PwindPri = ones(length(ft),2);% total primary winding losses [Watts]
PwindSec = ones(length(ft),2);% total secondary winding losses [Watts]
PwindTotal = ones(length(ft),2);% total winding losses  [Watts]

Lm = ones(length(ft),2);% Magnatizing inductance [Henry]
Im = ones(length(ft),2);% Magnatizing current [Amp]
Im_Iin= ones(length(ft),2);% Magnatizing to input current ratio [%]
Bcheck =ones(length(ft),2); % calcualted B for the transformer

Pcore     = ones(length(ft),2); % total winding losses [Watts]
PLossTotal = ones(length(ft),2); % total transformer losses [Watts]
efficiencyTrans =ones(length(ft),2); % Transformer Effiecincy  [Watts]
wireAPri              = ones(length(ft),2);
wireASec              = ones(length(ft),2);
AWGAreaSelectedPri    = ones(length(ft),2);
AWGAreaSelectedSec    = ones(length(ft),2);
AWGNameSelectedPri    = cell(length(ft),2);
AWGNameSelectedSec    = cell(length(ft),2);
rhoAWGMaxTPri         = ones(length(ft),2);
rhoAWGMaxTSec         = ones(length(ft),2);
```

```
% OptSelect = 2; % 1 for optimium losses , 2 for lower size

for z =1:2 % 1 is for min Losses, 2 is for min Size
   for i=1:length(ft)
      skinDepth(i,z) = 6.62/sqrt(ft(i)); % [cm]
      wireD(i,z) = 2*skinDepth(i,z);    % [cm]

      wireA(i,z) = pi*(wireD(i,z)^2)/4;   % [cm^2]

      IndexTemp = find(AWGArea>wireA(i,z));
      if isempty(IndexTemp) % skin effect is too big - use the biggest wire possible
         IndexTemp = 1;
      end
      IndexTemp = IndexTemp(end);



      AWGAreaSelected(i,z)  = AWGArea(IndexTemp); % AWG wire size selected in [cm^2]
      AWGNameSelected(i,z) = AWGName(IndexTemp);
      rhoAWGMaxT(i,z) = AWGRho(IndexTemp)*(1+alfa20*(Tmax-20));

      if z==1              % Minimum Losses & Bcal < Bsat
         Bo(i,z) = ((hc*ka*dT)^(2/3))*...
            ((Kv*ft(i)*kf*ku/transVA)^(1/6))/...
            (2^(2/3))/...
            ((rhoAWGMaxT(i,z)*kw*ku)^(1/12))/...
            ((kc*Kc*ft(i)^alfa)^(7/12)); % [Tesla]
         if (Bo(i) > BpeakVec(i)) || (Bo(i) == BpeakVec(i)) % Minimum Losses & Bcal > Bsat
            Bo(i) = 0.85*BpeakVec(i);
         end
         BratioMaxEff(i,CoreIndex-1) = 100*Bo(i,z)/BpeakVec(i);
      elseif z==2          % Min Size
         Bo(i,z) = 0.95*BpeakVec(i);
         BratioMinSize(i,CoreIndex-1) = 100*Bo(i,z)/BpeakVec(i);
```

```
end

Ap(i,z) = ((sqrt(2)*transVA/Kv/ft(i)/Bo(i,z)/kf/kt/sqrt(ku*dT))^(8/7));% [m^4]
if z==2
   TransAPMinSize(i,CoreIndex-1) =  Ap(i,z);
else
   TransAPMaxEff(i,CoreIndex-1) = Ap(i,z);
end

Jo(i,z) = kt*sqrt(dT/(2*ku))/(Ap(i,z)^(1/8)); % [A/(m^2)]

[atemp,al,am,ar,aw,at,btemp,bw,bt,aair,bair,wa,ac,vc,mlt,lc]=transDim(Ap(i,z));

a(i,z) = atemp; % [m]
b(i,z) = btemp;  % [m]
d(i,z) = bw; % [m]
transWidth(i,z) = at;  % [m]
transHeight(i,z) = bt; % [m]

MLT(i,z) = mlt;        % [m]
MLTmid(i,z) = MLT(i,z); % [m]
MPL(i,z) = lc;



Ac(i,z) = ac;          % [m^2]
Am(i,z) = kf*Ac(i,z);    % [m^2]
Wa(i,z) = wa;          % [m^2]
Vc(i,z) = vc;

Np(i,z) = ceil(VtIn/Kv/ft(i)/Bo(i,z)/Am(i,z));
Ns(i,z) = ceil(VtOut/Kv/ft(i)/Bo(i,z)/Am(i,z));

Lm(i,z) = 4*pi*1e-7*muh*Np(i,z)^2*Ac(i,z)/MPL(i,z);
Im(i,z) = VtIn/(2*pi*ft(i))/Lm(i,z);
```

```
Bcheck(i,z) = 4*pi*1e-7*muh*Im(i,z)*Np(i,z)/MPL(i,z);
Im_Iin(i,z)= Im(i,z)/ItInput*100;

totalWireAreaRriTemp = ItInput/Jo(i,z)*1e4; % [cm^2]
totalWireAreaSecTemp = ItOut/Jo(i)*1e4;% [cm^2]

wireStrandsPri(i,z) = (totalWireAreaRriTemp/AWGAreaSelected(i,z));
wireStrandsSec(i,z) = (totalWireAreaSecTemp/AWGAreaSelected(i,z));

if ( wireStrandsPri(i,z) < 1)
   wireStrandsPri(i,z) = 1;
   wireAPri(i,z) = totalWireAreaRriTemp;   % [cm^2]
   IndexTempPri = find(AWGArea>wireAPri(i,z));
   IndexTempPri = IndexTempPri(end);
   AWGAreaSelectedPri(i,z)  = AWGArea(IndexTempPri); % AWG wire size selected in [cm^2]
   AWGNameSelectedPri(i,z) = AWGName(IndexTempPri);
   rhoAWGMaxTPri(i,z) = AWGRho(IndexTempPri)*(1+alfa20*(Tmax-20));
   if ( AWGAreaSelectedPri(i,z) > AWGAreaSelected(i,z) )
      error('Case 1- No strands | The skin depth is smaller than the selected Primary wire Radius -
Low utilization of Copper ')
   end
else
   wireStrandsPri(i,z) = ceil(wireStrandsPri(i,z));
   IndexTempPri    = IndexTemp;
   AWGAreaSelectedPri(i,z)  = AWGArea(IndexTempPri); % AWG wire size selected in [cm^2]
   AWGNameSelectedPri(i,z) = AWGName(IndexTempPri);
   rhoAWGMaxTPri(i,z) = AWGRho(IndexTempPri)*(1+alfa20*(Tmax-20));
end

if ( wireStrandsSec(i,z) < 1)
   wireStrandsSec(i,z)  = 1;
   wireASec(i,z)     = totalWireAreaSecTemp;   % [cm^2]
   IndexTempSec   = find(AWGArea>wireASec(i,z));
   IndexTempSec   = IndexTempSec(end);
   AWGAreaSelectedSec(i,z)  = AWGArea(IndexTempSec);
```

```
            AWGNameSelectedSec(i,z) = AWGName(IndexTempSec);
            rhoAWGMaxTSec(i,z) = AWGRho(IndexTempSec)*(1+alfa20*(Tmax-20));
            if ( AWGAreaSelectedSec(i,z) > AWGAreaSelected(i,z) )
               error('Case 1- No strands | The skin depth is smaller than the selected Secondary wire Radius -
Low utilization of Copper ')
            end
         else
            wireStrandsSec(i,z) = ceil(wireStrandsSec(i,z));
            IndexTempSec    = IndexTemp;
            AWGAreaSelectedSec(i,z)  = AWGArea(IndexTempSec); % AWG wire size selected in [cm^2]
            AWGNameSelectedSec(i,z) = AWGName(IndexTempSec);
            rhoAWGMaxTSec(i,z) = AWGRho(IndexTempSec)*(1+alfa20*(Tmax-20));
         end

         Rpri(i,z) = (2*MLT(i,z)*Np(i,z)*rhoAWGMaxTPri(i,z)/wireStrandsPri(i,z))+...
            (MLTmid(i,z)*Np(i,z)*rhoAWGMaxTPri(i,z)/wireStrandsPri(i,z));
         PwindPri(i,z) = Rpri(i,z)*(ItInput)^2;
         Rsec(i,z) = (2*MLT(i,z)*Ns(i,z)*rhoAWGMaxTSec(i,z)/wireStrandsSec(i,z))+...
            (MLTmid(i,z)*Ns(i,z)*rhoAWGMaxTSec(i,z)/wireStrandsSec(i,z));

         PwindSec(i,z) = Rsec(i,z)*(ItOut)^2;
         PwindTotal(i,z) =  Rpri(i,z)+PwindSec(i,z);
         Pcore(i,z)  = Vc(i,z)*Kc*ft(i)^alfa*Bo(i,z)^beta;

         Rcore(i,z) = Pcore(i,z)/VtIn;

         PLossTotal(i,z) = PwindSec(i,z)+Pcore(i,z);
         efficiencyTrans(i,z) = Ptout/(Ptout+PLossTotal(i,z))*100;
         if z==2
            TransEffMinSize(i,CoreIndex-1) = efficiencyTrans(i,z);
         else
            TransEffMaxEff(i,CoreIndex-1) = efficiencyTrans(i,z);
         end
      end
   end
```

```
    FileName = [CoreMaterial,'-',num2str(Ptout),'Watts'];

    %% save transformer parameters in excel
    TransformerParemeters = cell(65,1+length(ft));
    TransformerParemetersMaxMu = cell(65,1+length(ft));
    TransformerParemetersMinSize = cell(65,1+length(ft));
for z=1:2
    TransformerParemeters(1,1) = {['Power Total is ', num2str(Ptout),' [Watts]',...
        ' | Input Voltage/Current is ',num2str(VtIn), '[Volt]/',num2str(ItInput),'[Amp]',...
        ' | Output Voltage/Current is ',num2str(VtOut),'[Volt]/',num2str(ItOut),'[Amp]',...
        ' | Material is ', CoreMaterial]};
    TransformerParemeters(2,1) = {'Tr #'};
    TransformerParemeters(3,1) = {'F[Hz]'};
    TransformerParemeters(4,1) = {'AWG(Pri/Sec)'};
    TransformerParemeters(5,1) = {'W[m]'};
    TransformerParemeters(6,1) = {'H[m]'};
    TransformerParemeters(7,1) = {'D[m]'};
    TransformerParemeters(8,1) = {'S/T-Pri'};
    TransformerParemeters(9,1) = {'T-Pri'};
    TransformerParemeters(10,1) = {'S/T-Sec'};
    TransformerParemeters(11,1) = {'T-Sec'};

    TransformerParemeters(12,1) = {'Rpri[Ohms]'};
    TransformerParemeters(13,1) = {'Rsec[Ohms]'};
    TransformerParemeters(14,1) = {'Rcore[Ohms]'};

    TransformerParemeters(15,1) = {'Ploss[Watts]'};
    TransformerParemeters(16,1) = {'Eff %'};

    TransformerParemeters(17,1) = {'Lm[H]'};
    TransformerParemeters(18,1) = {'Im/Iin[%]'};
    % -------- mechanical Parameters -------- %
    TransformerParemeters(19,1) = {'Transformer Parameters for Comsol Simulation'};
```

```
TransformerParemeters(20,1) = {'KuFinal'};
TransformerParemeters(21,1) = {'a'};
TransformerParemeters(22,1) = {'al'};
TransformerParemeters(23,1) = {'am'};
TransformerParemeters(24,1) = {'ar'};
TransformerParemeters(25,1) = {'aw'};
TransformerParemeters(26,1) = {'at'};
TransformerParemeters(27,1) = {'b'};
TransformerParemeters(28,1) = {'bw'};
TransformerParemeters(29,1) = {'bt'};
TransformerParemeters(30,1) = {'lw'};
TransformerParemeters(31,1) = {'awp'};
TransformerParemeters(32,1) = {'aws'};
TransformerParemeters(33,1) = {'awpm'};
TransformerParemeters(34,1) = {'awsm'};
TransformerParemeters(35,1) = {'xwl'};
TransformerParemeters(36,1) = {'ywl'};
TransformerParemeters(37,1) = {'xwr'};
TransformerParemeters(38,1) = {'ywr'};
TransformerParemeters(39,1) = {'aair'};
TransformerParemeters(40,1) = {'bair'};
TransformerParemeters(41,1) = {'xair'};
TransformerParemeters(42,1) = {'yair'};
TransformerParemeters(43,1) = {'yw'};
TransformerParemeters(44,1) = {'xwplr'};
TransformerParemeters(45,1) = {'xwpll'};
TransformerParemeters(46,1) = {'xwpmr'};
TransformerParemeters(47,1) = {'xwpml'};
TransformerParemeters(48,1) = {'xwprr'};
TransformerParemeters(49,1) = {'xwprl'};
TransformerParemeters(50,1) = {'xwslr'};
TransformerParemeters(51,1) = {'xwsll'};
TransformerParemeters(52,1) = {'xwsmr'};
TransformerParemeters(53,1) = {'xwsml'};
TransformerParemeters(54,1) = {'xwsrr'};
```

```
TransformerParemeters(55,1) = {'xwsrl'};
TransformerParemeters(56,1) = {'Np'};
TransformerParemeters(57,1) = {'Ns'};
TransformerParemeters(58,1) = {'Vac'};
TransformerParemeters(59,1) = {'Freq'};
TransformerParemeters(60,1) = {'Rc'};
TransformerParemeters(61,1) = {'Rl'};
TransformerParemeters(62,1) = {'clear'};
TransformerParemeters(63,1) = {'wireApri'};
TransformerParemeters(64,1) = {'wireAsec'};
TransformerParemeters(65,1) = {'Im'};

for i = 2:length(ft)+1
    TransformerParemeters(2,i) = {i-1};
    TransformerParemeters(3,i) = {ft(i-1)};
    TransformerParemeters(4,i) = {[char(AWGNameSelectedPri(i-
1,z)),'\',char(AWGNameSelectedSec(i-1,z))]};
    TransformerParemeters(5,i) = {transWidth(i-1,z)};
    TransformerParemeters(6,i) = {transHeight(i-1,z)};
    TransformerParemeters(7,i) = {a(i-1,z)};
    TransformerParemeters(8,i) = {wireStrandsPri(i-1,z)};
    TransformerParemeters(9,i) = {Np(i-1,z)};
    TransformerParemeters(10,i) = {wireStrandsSec(i-1,z)};
    TransformerParemeters(11,i) = {Ns(i-1,z)};

    TransformerParemeters(12,i) = {Rpri(i-1,z)};
    TransformerParemeters(13,i) = {Rsec(i-1,z)};
    TransformerParemeters(14,i) = {Rcore(i-1,z)};

    TransformerParemeters(15,i) = {PLossTotal(i-1,z)};
    TransformerParemeters(16,i) = {efficiencyTrans(i-1,z)};

    TransformerParemeters(17,i) = {Lm(i-1,z)};
    TransformerParemeters(18,i) = {Im_Iin(i-1,z)};
    %---------- transformer mechnical structure parameters for templates -----
```

```
[atemp,al,am,ar,aw,at,btemp,bw,bt,aair,bair,wa,ac,vc,mlt,lc]=transDim(Ap(i-1,z));
[lw,awp,aws,awpm,awsm,kuFinal]=windingDim(aw,bw,AWGAreaSelectedPri(i-1,z)*1e-4,AWGAreaSelectedSec(i-1,z)*1e-4,Np(i-1,z),Ns(i-1,z),wireStrandsPri(i-1,z),wireStrandsSec(i-1,z));

[xwl,ywl,xwr,ywr,xair,yair,yw,xwplr,xwpll,xwpmr,xwpml,xwprr,xwprl,xwslr,xwsll,xwsmr,xwsml,xwsrr,xwsrl]=WindingOrientation(ar,al,aw,am,awpm,awsm,awp,aws,at,btemp,bt,bw);

insThickness= 0.5;% 5 mm
if z==2
   TransLleakMinSize(i-1,CoreIndex-1) = 4*pi*100*MLT(i-1,z)*(Np(i-1,z)^2)/(bw*100)*(insThickness+(100*(awp+aws)/3))*1e-9;
else
   TransLleakMaxEff(i-1,CoreIndex-1) = 4*pi*MLT(i-1,z)*100*(Np(i-1,z)^2)/(bw*100)*(insThickness+(100*(awp+aws)/3))*1e-9;
end

TransformerParemeters(20,i) = {num2str(kuFinal)};% {'a'};
TransformerParemeters(21,i) = {[num2str(a(i-1,z)),'[m]']};% {'a'};
TransformerParemeters(22,i) = {[num2str(al),'[m]']};% {'al'};
TransformerParemeters(23,i) = {[num2str(am),'[m]']};% {'am'};
TransformerParemeters(24,i) = {[num2str(ar),'[m]']};% {'ar'};
TransformerParemeters(25,i) = {[num2str(aw),'[m]']};% {'aw'};
TransformerParemeters(26,i) = {[num2str(at),'[m]']};% {'at'};
TransformerParemeters(27,i) = {[num2str(btemp),'[m]']};% {'b'};
TransformerParemeters(28,i) = {[num2str(bw),'[m]']};% {'bw'};
TransformerParemeters(29,i) = {[num2str(bt),'[m]']};% {'bt'};
TransformerParemeters(30,i) = {[num2str(lw),'[m]']};% {'lw'};
TransformerParemeters(31,i) = {[num2str(awp),'[m]']};% {'awp'};
TransformerParemeters(32,i) = {[num2str(aws),'[m]']}; % {'aws'};
TransformerParemeters(33,i) = {[num2str(awpm),'[m]']};% {'awpm'};
TransformerParemeters(34,i) = {[num2str(awsm),'[m]']}; % {'awsm'};

TransformerParemeters(35,i) = {[num2str(xwl),'[m]']};% {'xwl'};
TransformerParemeters(36,i) = {[num2str(ywl),'[m]']};% {'ywl'};
```

```
TransformerParemeters(37,i) = {[num2str(xwr),'[m]']};% {'xwr'};
TransformerParemeters(38,i) = {[num2str(ywr),'[m]']};% {'ywr'};
TransformerParemeters(39,i) = {[num2str(aair),'[m]']};% {'aair'};
TransformerParemeters(40,i) = {[num2str(bair),'[m]']};% {'bair'};
TransformerParemeters(41,i) = {[num2str(xair),'[m]']};% {'xair'};
TransformerParemeters(42,i) = {[num2str(yair),'[m]']};% {'yair'};
TransformerParemeters(43,i) = {[num2str(yw),'[m]']};% {'yw'};
TransformerParemeters(44,i) = {[num2str(xwplr),'[m]']};% {'xwplr'};
TransformerParemeters(45,i) = {[num2str(xwpll),'[m]']};% {'xwpll'};
TransformerParemeters(46,i) = {[num2str(xwpmr),'[m]']};% {'xwpmr'};
TransformerParemeters(47,i) = {[num2str(xwpml),'[m]']};% {'xwpml'};
TransformerParemeters(48,i) = {[num2str(xwprr),'[m]']};% {'xwprr'};
TransformerParemeters(49,i) = {[num2str(xwprl),'[m]']};% {'xwprl'};

TransformerParemeters(50,i) = {[num2str(xwslr),'[m]']};% {'xwslr'};
TransformerParemeters(51,i) = {[num2str(xwsll),'[m]']};% {'xwsll'};
TransformerParemeters(52,i) = {[num2str(xwsmr),'[m]']};% {'xwsmr'};
TransformerParemeters(53,i) = {[num2str(xwsml),'[m]']};% {'xwsml'};

TransformerParemeters(54,i) = {[num2str(xwsrr),'[m]']};% {'xwsrr'};
TransformerParemeters(55,i) = {[num2str(xwsrl),'[m]']};% {'xwsrl'};

TransformerParemeters(56,i) = {num2str(Np(i-1,z))};% {'Np'};
TransformerParemeters(57,i) = {num2str(Ns(i-1,z))};% {'Ns'};
TransformerParemeters(58,i) = {[num2str(sqrt(2)*VtIn),'[V]']};% {'Vac'};
TransformerParemeters(59,i) = {[num2str(ft(i-1)),'[Hz]']};% {'Freq'};
TransformerParemeters(60,i) = {[num2str(0.01*Rpri(i-1,z)),'[ohm]']};% {'Rc'};
TransformerParemeters(61,i) = {[num2str(100),'[Mohm]']};% {'Rl'};
TransformerParemeters(62,i) = {[num2str(0),'[m]']};% {'clear'};
TransformerParemeters(63,i) = {[num2str(AWGAreaSelectedPri(i-1,z)*1e-4),'[m^2]']};%
{'wireDpri'};
TransformerParemeters(64,i) = {[num2str(AWGAreaSelectedSec(i-1,z)*1e-4),'[m^2]']};%
{'wireDsec'};
TransformerParemeters(65,i) = {[num2str(sqrt(2)*Im(i-1,z)),'[A]']};% {'wireDsec'};
```

```
    end

    if z==1
        TransformerParemetersMaxMu = TransformerParemeters;
    elseif z==2
        TransformerParemetersMinSize = TransformerParemeters;
    end

end

%% write the results in excel sheet
TransformerParemetersTemp = cell(65,2);
TransformerParemetersTemp(:,1) = TransformerParemetersMaxMu(:,1);
for z=1:2
    if z==1
        for i = 2:length(ft)+1
            TransformerParemetersTemp(:,2) = TransformerParemetersMaxMu(:,i);
            xlswrite([folderName,'\',FileName],TransformerParemetersTemp,['MaxEff-',num2str(ft(i-1)),'Hz'])
        end
    else
        for i = 2:length(ft)+1
            TransformerParemetersTemp(:,2) = TransformerParemetersMinSize(:,i);
            xlswrite([folderName,'\',FileName],TransformerParemetersTemp,['MinSize-',num2str(ft(i-1)),'Hz'])
        end
    end
end
close all

end

save([folderName,'\','transformer3DPlotData.mat'],'ft','CoreNameVec','BratioMinSize','BratioMaxEff',...
    'TransEffMinSize','TransEffMaxEff','TransAPMinSize','TransAPMaxEff',...
    'TransLleakMinSize','TransLleakMaxEff')  % save mat file for plotting afterwards - design summery
```

```
function [a,al,am,ar,aw,at,b,bw,bt,aair,bair,wa,ac,vc,mlt,lc]=transDim(Ap)

a = 0.537*(Ap^(1/4));
al  = a;   % Left limb a
am = a;   % Middle limb a
ar  = a;   % Right limb a
aw = 3*a; % window a

at  = al+ar+am+2*aw; % transformer lenght

b = a;
bw = 4*a; % window b

bt = 2*b+bw; % transformer b

aair = 2*at; % air a
bair = 2*bt; % air b

wa = aw*bw;          % window area
ac = a*a ;             % core area
vc = a^2*(2*at+3*bw);   % core volume
mlt = a+0.5*aw;        % mean magnetic length
lc = a+aw+b+bw;        % magentic lenght in the core
```

```
function
[lw,awp,aws,awpm,awsm,ku]=windingDim(aw,bw,coilAPri,coilASec,Np,Ns,StrandsPri,StrandsSec)

lw = bw*0.95;

coilDPri = sqrt(StrandsPri*coilAPri*4/pi);
NCoilsStripPri  = ceil(lw/coilDPri);
NstripsPri = ceil(Np/NCoilsStripPri);
awp = NstripsPri*coilDPri;
awpm = awp;
```

```
coilDSec = sqrt(StrandsSec*coilASec*4/pi);
NCoilsStripSec  = ceil(lw/coilDSec);
NstripsSec= ceil(Ns/NCoilsStripSec);
aws = NstripsSec*coilDSec;
awsm = aws;

ku = (awp+aws+awpm+awsm)/aw;
```

```
function
[xwl,ywl,xwr,ywr,xair,yair,yw,xwplr,xwpll,xwpmr,xwpml,xwprr,xwprl,xwslr,xwsll,xwsmr,xwsml,xwsrr,x
wsrl]=WindingOrientation(ar,al,aw,am,awpm,awsm,awp,aws,at,b,bt,bw)

% Core window orientation
xwl = al; % Left window corner X
ywl = b; % Left window corner Y
xwr = al+aw+am; % Right window X
ywr = b; % Right window corner Y

% Air Orientation
xair = 0.5*at; % X corner for the air
yair = 0.5*bt; % Y corner for the air

% Winding orientation
yw = b+0.5*0.05*bw; % Y corner for all the coils winding

% primary winding Orientation
xwplr = al;              % X corner for the Primary/Left winding - Right portion
xwpll = -awp;            % X corner for the Primary/Left winding - Left portion
xwpmr = al+aw+am;        % X corner for the Primary/Middle winding - Right portion
xwpml = al+aw-awpm; % X corner for the Primary/Middle winding - Left portion
xwprr = at;              % X corner for the Primary/Right winding - Right portion
xwprl = at-ar-awp;       % X corner for the Primary/Right winding - Left portion
```

```
% secondary Winding Orientation
xwslr = al+awp;            % X corner for the Secondary/Left winding - Right portion
xwsll = -awp-aws;          % X corner for the Secondary/Left winding - Left portion
xwsmr = xwpmr+awpm;      % X corner for the Secondary/Middle winding - Right portion
xwsml = xwpml-awsm;       % X corner for the Secondary/Middle winding - Left portion
xwsrr = xwprr+awp;         % X corner for the Secondary/Right winding - Right portion
xwsrl = xwprl -aws;         % X corner for the Secondary/Left winding - Left portion
```